A Study Of Gelatin Bird Strike Pressure Profiles And The Importance Of Deviatoric Stresses For Bird Strike Simulations

by

Shaun Kennedy

BCS, Acadia University, 2003

BSc E (Mechanical Engineering), University of New Bunswick, 2007

A Dissertation Submitted in Partial Fulfillment

of the Requirements for the Degree of

Doctor of Philosophy

in the Graduate Academic Unit of Mechanical Engineering

Supervisor: Andy Simoneau, Ph.D., Dept. of Mechanical Engineering

Examining Board: Clodualdo Aranas, Ph.D., Dept. of Mechanical Engineering

Mohsen Mohammadi, Ph.D., Dept. of Mechanical Engineering

Othman Nasir, Ph.D., Dept. of Civil Engineering

External Examiner: Marwan Hassan, Ph.D., Dept. of Mechanical Engineering,

University of Guelph

This dissertation is accepted by the Dean of Graduate Studies

THE UNIVERSITY OF NEW BRUNSWICK

June 2025

ABSTRACT

Computer simulations are typically used in the design of aircraft to ensure safety in the event of a bird strike. However, there is very little published experimental data available for validating potential bird impact models. To address this void, 17 impact tests were performed. The peak pressures achieved in this work were significantly higher than previously published results.

Parametric studies were carried out to determine the effects of bird model parameters on the resulting impact pressure profile. While previous works have claimed to successfully match experimental pressure profiles, the experimental and modeling results from this research highlight the very limited success of previous experimental and modeling results, and their interpretation. The parametric studies carried out enabled the development of a material model that more closely matches the more reliable experimental results carried out in this research.

One of the most important results from this research is the conclusive evidence towards the importance of peak impulse. In the past, it was assumed by some that the peak portion of the pressure profile is negligible as compared to the steady-state portion and may be ignored. However, the results from this research clearly demonstrated the significance of the peak impulse as it was shown that the peak deflection of an aluminum plate was increased with increasing peak impulse even when the steady-state and total impulses were decreased.

The importance of shear thickening behavior and deviatoric stresses was discovered in the research. While it has been shown that the dynamic viscosity of gelatin increases exponentially with strain rate, this research demonstrates how the shear thickening behavior of the gelatin bird could cause the dynamic viscosity to increase significantly during the high strain rate impact event. This increase in dynamic viscosity was shown to have a significant effect on the pressure profiles created during the event and demonstrated the importance of considering the deviatoric terms of a material model as opposed to just considering the hydrodynamic terms as was done in the past by many researchers. A suggested shear thickening bird material model was also proposed for future work.

DEDICATION

I would like to dedicate this thesis to the late Dr. Ann Sherman and my late father, Barry Kennedy.

Ann was the former Dean of Education at UNB but was also a great family friend. She was instrumental in convincing me to complete this PhD and I made a promise to her in her finals days that I would finish it for her. It was not easy for me to finish this thesis while running a start-up business and raising two kids, but Ann provided me with the motivation I needed.

My father was always immensely proud of me and how I would be the first person in our family to receive a PhD. Unfortunately, he passed away just before I was able to do my defence. The pride and encouragement he always showed me is something I strive to replicate with my own children, as the impact it had on me is unquantifiable.

ACKNOWLEDGEMENTS

I would like to once again thank Dr. Ann Sherman for her motivation in helping me complete this thesis. I would also like to thank my supervisor Dr. Andy Simoneau for his patience and guidance. Of course, I would like to acknowledge my wife Jenna and my children, Carter and Leah, for their continued support and understanding, as one the hardest things I had to do was sacrifice family time to complete this work. Finally, I would like to thank my parents, Barry and Debbie Kennedy, who have always been my biggest fans and have supported me my whole life to put me in a position where I am able to have an opportunity to complete a PhD.

Table of Contents

List of Tables

List of Figures

List of Acronyms

ALE – Arbitrary Lagrange Euler

DAQ – Data Acquisition

DIC – Digital Image Correlation

EOS – Equation of State

FAA – Federal Aviation Administration

FE – Finite Element

FEA – Finite Element Analysis

FOD – Foreign Object Damage

GCI – Grid Convergence Index

HOT – Higher Order Terms

SPH – Smooth Particle Hydrodynamics

UNB – University of New Brunswick

Vc – Cruising Speed

1 Introduction

1.1 Background

It has been estimated that over 30,000 bird strike incidents involving civilian aircrafts occur annually, and that these incidents cost the aviation industry $3 billion dollars a year [1]. One of the Federal Aviation Administration (FAA) requirements is that an airplane must be capable of successfully completing a flight after structural damage has occurred to a wing due to an impact with a 1.814 kg bird at a speed equal to the greater of the cruising speed (Vc) of the airplane at sea level or 0.85 Vc at 2440 m [2]. It should be noted that other components, such as the empennage and windshield, must meet other requirements; however, these components are not within the scope of this project.

Failing a certification test can be extremely costly to an aerospace company, as it would lead to the redesign and remanufacturing of components. Prototype testing may be performed before the certification tests; however, these physical tests can also be very costly and time consuming. Prototype testing also introduces added biological hazards by increasing the number of real birds that are used [3]. For this reason, it is highly desirable to use computer simulations early in the design phase to minimize the amount of physical testing required. The use of computer simulations may also help to reduce the weight of the leading edges as it would provide a more cost-effective tool to minimize the weight, while maintaining confidence in the ability to pass the certification tests.

During an impact event, there is a critical link between a target's behavior and the projectile's material. Therefore, it is very important that the projectile material model is able to accurately represent the loading conditions from the projectile (i.e., the bird). To ensure the accuracy of a bird strike simulation, data from actual testing must be obtained for purposes of validation. There exists some published data for the pressures/forces generated during a bird strike, however, a lot of the published data contains large variations in results and there is not a lot of published data that contains a statistically significant repetition of specific impact conditions. This makes it difficult to validate the quality of bird strike simulations. For these reasons, there is an interest in a hybrid method of simulations and testing [4].

In the past, it has been assumed by some that the bird material model may ignore the deviatoric terms and only requires an initial density and equation of state [5] to accurately replicate the loading conditions. Another assumption that has been made by the industry is that the peak pressures may be ignored and that the steady-state regime dominates. The validity of both of these assumptions was investigated as part of this work.

1.2 Objectives

Given the costs associated (both financial and human life costs) with bird strikes and its importance to researchers, material scientists and aviation designers, it is imperative that a suitable bird (the projectile in a bird strike) material model be developed. More accurate simulations and testing will help to reduce the time and costs associated with the required physical testing.

The thesis is divided into four main objectives:

1. Develop an experimental method for the generation of statistically significant data that can be used to help characterize a gelatin bird material model for use in simulations of specific FAA certification tests (in this case, for a 1.814 kg gelatin bird simulant impact at 170 m/s).
2. Improve the understanding of how various parameters affect the pressure profile resulting from a gelatin bird strike.
3. Investigate the importance of the peak pressures and whether they can be ignored as is often done in industry.
4. Investigate the importance of the deviatoric stresses and shear thickening behavior when modeling a gelatin bird simulant impact.

The results of this work should have significant value to the scientific community as it will not only provide a higher quality data set to work with but will also help to understand certain trends associated with various parameters that will aid researchers to fine tune bird models in the future. There are also conflicting views regarding the importance of peak pressures and deviatoric stresses when modeling bird strikes. The importance of shear thickening behavior was investigated as part of the work related to the importance of the deviatoric stresses. The results of this work should help to clarify the validity of current assumptions for future researchers.

1.3 Scope of Work

To achieve the research objectives, the research methodology and constraints need to be clearly detailed. FAA requirements for testing may vary dramatically based on the type of aircraft, cruising speeds, and section of the aircraft being tested [2]. This research was very focused for a specific aircraft's leading-edge impact. As a result, the following scope was set.

- The scope of work was limited to a 1.814 kg (4 lb) bird as per the FAA requirements for a wing leading edge [2].
- A speed of 330 knots (170 m/s) was used, as this was the speed required for a particular aircraft that was of interest for a commercial aerospace company that was involved in the early work.
- This thesis only concerns the development of the bird model. Leading edge models will be left for future work.
- Real birds were not used for the purpose of this thesis. A gelatin bird simulant was used instead as a proof of concept. Real birds may be used in future work to develop a more realistic bird model.

2 Literature Review

A thorough literature review was done regarding the simulation of bird strikes. This review includes examining different modeling methods such as Lagrangian, Eulerian, ALE and SPH methodologies. A review of some of the published material models for bird strike simulations is included as well as a review of some of the previously published experimental results.

2.1 Hydrocode Modeling of High-Speed Impacts

A hydrocode is a computational tool for modeling the behavior of continuous media, typically for time-dependent, non-linear problems [6]. When solid materials impact at speeds greater than the material's local sound speed, the material acts as a fluid and hydrodynamic effects dominate. Early versions of hydrocodes considered only these hydrodynamic effects, while newer codes consider material strength and failure as well, which makes them very robust for solving most impact problems [7].

A hydrocode problem can be divided into the following components which, when combined, can result in a complete solution to the problem [8]:

1. Newtonian Laws of Motion – a set of differential equations derived from the principles of conservation of momentum, mass, and energy:
    a. Conservation of mass:

$$\rho = \frac{m}{V} = \frac{\rho_0 V_0}{V} \qquad \text{Equation 1}$$

where ρ is the current density, ρ_0 is the original density, m is mass, V is volume, and V_0 is the original volume.

b. Conservation of momentum:

$$\rho \ddot{x} = \frac{\partial \sigma_{xx}}{\partial x} + \frac{\partial \sigma_{xy}}{\partial y} + \frac{\partial \sigma_{xz}}{\partial z}$$

$$\rho \ddot{y} = \frac{\partial \sigma_{yx}}{\partial x} + \frac{\partial \sigma_{yy}}{\partial y} + \frac{\partial \sigma_{yz}}{\partial z} \qquad \text{Equation 2}$$

$$\rho \ddot{z} = \frac{\partial \sigma_{zx}}{\partial x} + \frac{\partial \sigma_{zy}}{\partial y} + \frac{\partial \sigma_{zz}}{\partial z}$$

where $\ddot{x}$, $\ddot{y}$, and $\ddot{z}$ are acceleration in the x, y, and z directions respectively, and σ_{ij} represents components of the stress tensor.

c. Conservation of energy:

$$\dot{e} = \frac{1}{\rho}\left(\sigma_{xx}\dot{\varepsilon}_{xx} + \sigma_{yy}\dot{\varepsilon}_{yy} + \sigma_{zz}\dot{\varepsilon}_{zz} + 2\sigma_{xy}\dot{\varepsilon}_{xy} + 2\sigma_{yz}\dot{\varepsilon}_{yz} + 2\sigma_{zx}\dot{\varepsilon}_{zx}\right) \qquad \text{Equation 3}$$

where $\dot{e}$ is the rate of change of energy with respect to time, and $\dot{\varepsilon}_{ij}$ represents components of the strain rate tensor.

2. Material Model – can be divided into two major components:
    a. Equation of State – relates pressure, density, and internal energy.
    b. Constitutive Model – can generally be divided into 2 sub-categories:
        i. Strength Model – describes the stress-strain relationship.
        ii. Failure Model – defines the loss of strength.
3. Initial and Boundary Conditions

The method in which the mathematical problem is solved is dependent on how the model is discretized.

2.1.1 Discretization Methods

Before discussing the various options for discretizing a bird model, the two different types of reference frames should first be understood. Field variables (displacement, density, etc.) can be described with respect to the original coordinates (before deformation) or with respect to the current coordinates (after deformation). The former description is called a Lagrangian or material frame of reference, while the latter is called an Eulerian or spatial frame of reference [9].

2.1.1.1 Lagrange

A Lagrangian discretization can be viewed as dividing the geometry into a grid. This can be a 2D grid or a 3D grid, depending on the problem. The points where the grid lines intersect are called nodes. In the Lagrange approach, as a body undergoes deformation, the nodes are forced to move and the element is distorted [10]. A typical problem with the Lagrange approach in high-speed impact problems is that the elements may become so distorted that they become inverted. This leads to negative volumes and errors in the simulation results [11]. To prevent these negative volumes from occurring, a technique called erosion is implemented. Erosion is used to remove elements once they reach a specified level of distortion. The onset of erosion can be based on various criteria, such as a strain or stress limit. Erosion allows the calculation to continue, but it lacks a physical basis and should therefore be used with caution [10].

Figure 1 shows a cylinder prior to and after impacting a wall that has been discretized using the Lagrange method. The distorted elements in the cylinder should be noted, especially close to the center of impact as the elements are severely distorted, which may lead to numerical errors.

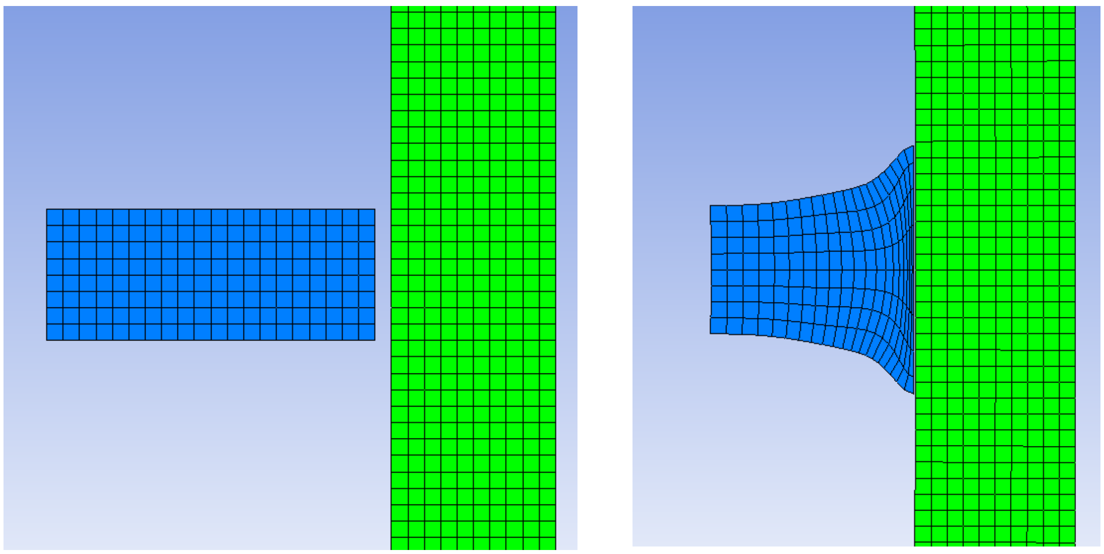

(a) (b)

Figure 1 – Lagrange simulation of cylinder before (a) and after (b) impact.

2.1.1.2 Euler

In an Eulerian discretization, the geometry is once again divided into a grid (usually rectangular or hexahedral in shape). The points where the grid lines intersect are once again called nodes. The difference in the Euler method is that as a body undergoes deformation, the nodes do not move, and hence the elements do not distort. Instead, the material flows through the elements and into the adjoining neighbors. This eliminates the major downfall of the Lagrange method as erosion techniques are no longer required. A disadvantage of the Euler method is that it is generally more computationally expensive than the Lagrange method. This is because the Euler method has to transport material from one element to another and track the material fractions in each cell [11]. Also, the Euler method typically requires more elements as it not only has to discretize the starting geometry, but it must also cover any areas where material may flow during the simulation [10].

It is also important to note that the location and interface of each material is tracked only approximately. The Euler solution only uses the volume fractions of material in each element. During post processing, an approximation (derived from the volume fractions) of the material boundaries may be displayed. However, this approximation is only accurate to within one element dimension [11].

The same model shown in Figure 1 is shown in Figure 2, however this model has been discretized using the Euler method. Notice that the elements have not been distorted. Instead, the material location is approximated within the fixed elements. Also, note the additional number of elements that are used outside of the area of interest during the Euler approach, which is one of its primary drawbacks.

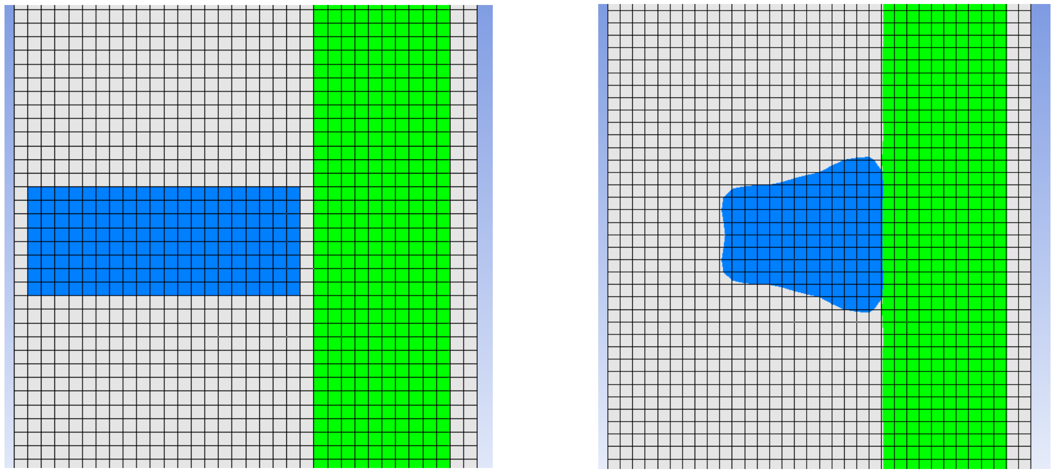

(a) (b)

Figure 2 – Euler simulation of cylinder before (a) and after (b) impact.

2.1.1.3 Arbitrary Lagrange Euler (ALE)

The ALE method is a combination of the Lagrange and Euler methods. It allows the grid to be redefined as the simulation proceeds. Normally, the rezoning is based on distortion limits such that once an element distorts to a certain point, the grid is restructured by moving the nodes and recalculating the solution for the new grid [12]. Typically, the elements on the boundaries and interfaces are Lagrangian and allowed to move with the materials to provide an accurate description of boundaries and interfaces during a solution. The inner elements, on the other hand, are usually allowed to move arbitrarily to optimize element shapes [13]. For example, the user may request that the inner elements attempt to remain equally spaced in a certain direction. Two major advantages of the ALE method are that it can reduce or eliminate the problems of severe mesh distortion that may occur with a purely Lagrangian method, and it allows a calculation to continue efficiently compared to a purely Eulerian method [14]. A major limitation to the ALE method is that it relies heavily on user input to determine if it acts more like a Lagrange grid or an Euler grid [12]. The ALE method may also struggle to handle material separation.

Figure 3 shows a cylinder prior to and after impacting a wall that has been discretized using the ALE method. In this instance an equipotential ALE rezoning scheme has been applied to control the spacing of inner elements. Note the spacing of the elements close to the impact plane as compared to those of the purely Lagrangian method in Figure 1. The equipotential and other ALE smoothing methods are described further in Souli et al. [15].

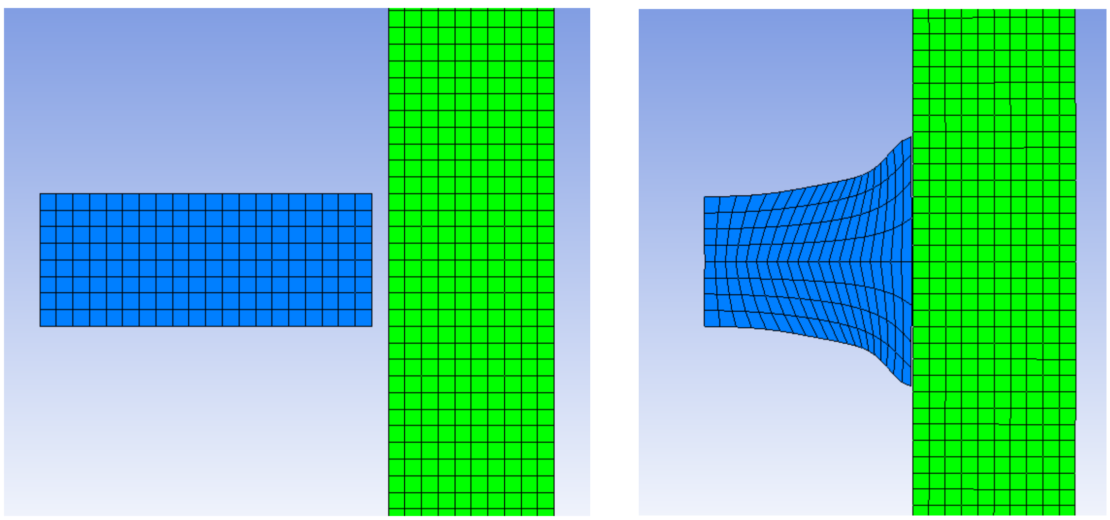

(a) (b)

Figure 3 – ALE simulation of cylinder before (a) and after (b) impact.

2.1.1.4 Smooth Particle Hydrodynamics (SPH)

SPH is a mesh free method of discretization that uses a Lagrangian frame of reference. In this technique, the geometry is filled with particles that are not attached by a grid. The particles act as interacting mass points as well as interpolation points used to calculate the value of field variables based on data from neighboring particles [14]. A kernel estimate allows the description of the conservation of mass, momentum and energy in terms of interpolation sums [10]. The SPH method has several advantages over the other methods. It eliminates the Lagrange problem of mesh entanglement and inverted elements, since there are no connecting grids between the particles. Material boundaries and interfaces are clearly defined, as opposed to the Euler method. It handles material separation (spalling, cracking), in a natural way since the particles are not physically bound together. One of the issues with the SPH technique is that it is computationally more expensive than a mesh-based Lagrange technique. This is partially due to the extra step of having to sort the particles in order to locate current neighbors [14]. Another potential issue is that there can sometimes be very large velocity oscillations in single particles [10].

Figure 4 shows a cylinder prior to and after impacting a wall that has been discretized using the SPH method. Note that there are no mesh entanglements, element deletions, and no extra elements outside of the area of interest. The SPH method has an advantage over ALE for this type of problem due to the way that it naturally handles the flow of material as opposed to ALE, which as the name suggests, requires an arbitrarily defined criterion to enable it to represent the physical response of the material.

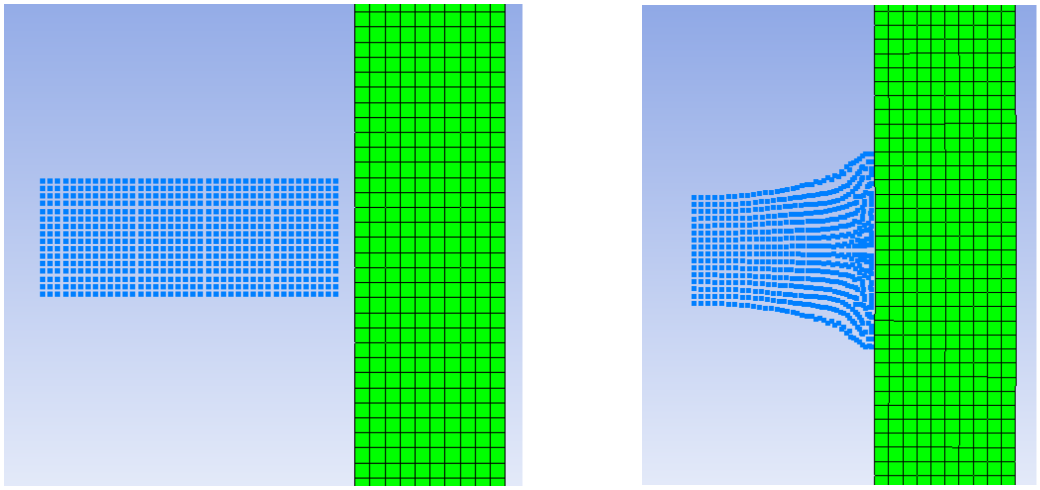

(a) (b)

Figure 4 – SPH simulation of cylinder before (a) and after (b) impact.

2.1.2 Material Modeling

The stress tensor for an element is made up of normal stresses (σ) and shear stresses (τ) as shown in Figure 5.

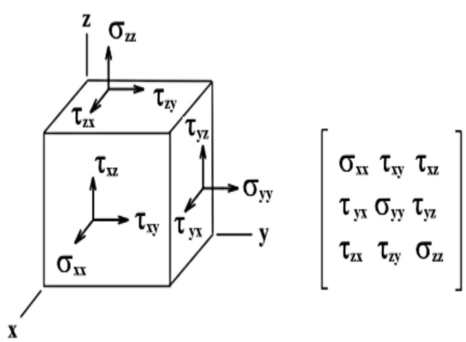

Figure 5 – Stress tensor for an element [16].

The stress tensor can be divided into two components: hydrostatic (volumetric) and deviatoric stresses. The hydrostatic stress portion is that which acts to change the volume of a material element subject to pressure. The deviatoric portion is a measure of the shear stress that distorts a material element without changing its volume [17]. The hydrostatic stress is defined as:

$$\sigma_v = \begin{bmatrix} \sigma_m & 0 & 0 \\ 0 & \sigma_m & 0 \\ 0 & 0 & \sigma_m \end{bmatrix} \qquad \text{Equation 4}$$

where the mean stress, σ_m is defined as:

$$\sigma_m = \frac{\sigma_{xx} + \sigma_{yy} + \sigma_{zz}}{3} \qquad \text{Equation 5}$$

Since the total stress tensor is defined as the sum of the hydrostatic and deviatoric stress tensors, the deviatoric stress can be defined as the total stress minus the hydrostatic stress:

$$\sigma_D = \begin{bmatrix} \sigma_{xx} - \sigma_m & \tau_{xy} & \tau_{xz} \\ \tau_{yx} & \sigma_{yy} - \sigma_m & \tau_{yz} \\ \tau_{zx} & \tau_{zy} & \sigma_{zz} - \sigma_m \end{bmatrix} \qquad \text{Equation 6}$$

The hydrostatic component is described using an equation of state (EOS), while the deviatoric component is described through a constitutive model [18]. The constitutive model can be subdivided into a strength model and a failure model. The accuracy of a hydrocode is greatly dependent on the sophistication of the equation of state and constitutive models defined [6].

2.1.3 Initial Conditions and Boundary Conditions

The initial and boundary conditions are important in any simulation model. Initial conditions set the start point for the simulation and the boundary conditions may dramatically impact the behavior of the model. In an impact simulation, the initial condition typically consists of the initial velocity of the projectile. The velocity must be given a magnitude and a direction. Initial conditions may also include the initialization of other state variables such as angular velocity, temperature, or internal energy.

Loads/boundary conditions may be applied to bodies, surfaces, lines, or points. The loading may be applied as a constant value over the entire simulation, or it may be specified as a time history with varying values. Velocity, acceleration, force, pressure, and temperature are all typical loadings used in impact modeling. Displacement is also available in some software packages; however, it is recommended to use velocity instead because specifying displacement may result in discontinuous velocities and infinite accelerations when they are differentiated in the solution phase [19]. For example, to fix the edges of a rectangular plate, one could apply constant zero velocity conditions in all directions to the nodes along the edges.

2.1.4 Contact/Interaction

Contact is a self-evident feature and challenge when modeling impact. As a result, a critical factor in any impact simulation is the ability to handle interaction between parts. This may include contact between multiple parts or self-contact due to gross deformation. In the set-up phase of a model, it is usually possible to define which surfaces/parts will interact with one another (including self-interaction). During the solution phase, only these specified surfaces will be checked for contact, which can save on computation time.

The interaction algorithm must determine which nodes/surfaces are in contact for each time step. One method of determining this is to assign an interaction gap size. This gap size is the distance allowed between two nodes/surfaces before contact is initiated. It essentially creates an artificial boundary around the elements, which will be checked to determine if anything has crossed over this boundary to initiate contact. This method requires that all interacting parts be separated by the specified gap size upon initiation. The gap size may influence the size of the time step. The time step should have a restriction placed on it to ensure that a node may not travel too far into a contacting surface so as to create instabilities (for example, AUTODYN restricts the time step such that there cannot be more than 20% penetration in a single step) [11].

There are various algorithms available for handling contact. The algorithm should conserve linear and angular momentum. One common method uses repelling forces to prevent two bodies from passing through one another. This method may be visualized as placing springs between the interacting nodes/elements. The spring force is typically determined by the relative stiffness of the contacting bodies and the penetration depth. Typically, there is also a penalty factor included in the calculation of the repelling force. There is usually a default value of the penalty factor provided with most software packages that has been calibrated to give realistic results [19]. This method conserves momentum by applying equal and opposite forces, however, it does not necessarily conserve kinetic energy, and therefore the energy error history should be checked in the post-processing phase to ensure realistic results [11].

The interaction may also include frictional contact between bodies. Friction is implemented in the model by applying a friction force upon contact initiation. For static friction, the force is defined as:

$$F = \mu_s N \qquad \text{Equation 7}$$

where F is the friction force, μ_s is the coefficient of static friction, and N is the normal force applied to the node/segment [11].

For dynamic friction, the force is defined as:

$$F = \mu_e N \qquad \text{Equation 8}$$

Where μ_e is the effective friction force which is defined as:

$$\mu_e = \mu_d + (\mu_s - \mu_d)e^{-\beta V} \qquad \text{Equation 9}$$

where μ_d is the coefficient of dynamic friction, β is the exponential decay coefficient, and V is the relative sliding velocity at the point of contact [11].

Another type of contact that may be defined is bonded (tied) contact in which contacting nodes are bonded to a surface. When the bond is in place, the slave nodes are forced to follow the target surface displacements. There is usually an option for failure criterion at which point the bonds will be broken. This failure criterion typically involves specifying normal and/or shear strengths [19].

As mentioned earlier, these are just some examples of interaction algorithms. The algorithms above are for Lagrange (including SPH) interactions; however, there are algorithms for Euler parts and Euler/Lagrange interactions as per [11]. There are numerous contact algorithms that have been employed for simulations. It is not practical to summarize all of them in this document. A good reference for how to treat interactions can be found in [20].

2.1.5 Shock Waves and Artificial Viscosity

High speed impacts may result in the formation of shock waves within the materials [11]. A shock wave is commonly described as a discontinuity where properties such as density, pressure, velocity, and temperature rapidly change. In reality, this rapid change in properties occurs over a very narrow transition zone [10]. Typically, a finite element model has difficulty solving this rapid change because the transition zone is normally smaller than the smallest cell size in the model [6]. Solving the conservation of mass, momentum, and energy equations for the discontinuity region using an explicit integration method may cause oscillations in velocity behind the shock front, which could cause singularities and therefore errors in the solution. Von Neumann and Richtmyer [21] noted that a natural dissipation mechanism was missing from the solution methodology. The equations failed to include the fact that some of the energy in a shock is lost when it is irreversibly converted into heat. To account for this heat dissipation of energy, they developed an artificial viscosity term [10]. The artificial viscosity is added to the pressure in the conservation of momentum and energy equations [22]. The result is that the shock transition is spread out over a few cells so that it has a finite thickness and transitions are better described numerically [18].

A typical formulation for artificial viscosity is shown in Equation 10.

$$q = \rho\left[\left(C_Q d \frac{\dot{V}}{V}\right)^2 - C_L c\, d \frac{\dot{V}}{V}\right] \quad for\ \frac{\dot{V}}{V} < 0 \qquad \text{Equation 10}$$

where q is the artificial viscosity pressure term, ρ is density, C_Q is the quadratic artificial viscosity coefficient, C_L is the linear artificial viscosity coefficient, d is a typical element length scale, c is the local sound speed, and $\dot{V}/V$ is the rate of change of volume. The quadratic term is used to smooth out the shock discontinuities, while the linear term dampens any oscillations behind the shock front [11]. The coefficients can be determined based on experimental comparisons.

2.1.6 Implicit vs. Explicit Solutions

Solution methods may be classified as either implicit or explicit. An implicit solution method is typically used for solving static/structural problems, wherein the following equation relating force and displacement is used:

$$F = m\frac{d^2x}{dt^2} + c\,\frac{dx}{dt} + kx \qquad \text{Equation 11}$$

where F is force, m is mass, x is displacement, c is damping, and k is stiffness. In a static problem, the displacement is not a function of time and therefore the derivatives (i.e. velocity and acceleration) are zero [23]. This leaves the force equal to the stiffness multiplied by the displacement. Each of these components is represented by matrices to include all the degrees of freedom in the model. The stiffness matrix is defined based on the material model and degrees of freedom. The force vector and stiffness matrix are known and therefore the displacements can be solved for using:

$$x = k^{-1}F \qquad \text{Equation 12}$$

where k^{-1} is the inverse of the stiffness matrix. In other words, the implicit method solves a set of simultaneous algebraic equations at each time step [24].

For non-linear problems, such as in high-speed impact problems that result in large deformations, the stiffness matrix is a function of displacement such that the velocity and acceleration components may not be zero [25]. These types of problems result in more complicated stiffness matrices as per [26], which are very computationally expensive to invert [25].

Another key characteristic of the implicit method is how it performs numerical time integration. In an implicit integration method, the solution at time $t + \Delta t$ is a function of the equilibrium condition at time $t + \Delta t$. Examples of implicit integration methods are Backwards Euler, Newmark, Wilson-θ, and Houbolt. More information on these methods can be found in [26].

The implicit method is an attractive method for static problems because it is unconditionally stable. It can also be executed using relatively large time steps and is typically solved iteratively using smaller time steps until a convergence criterion is met. However, the implicit method has a large computational cost associated with non-linear problems as described above, and it also is computationally expensive for transient problems due to the requirement of iterative solutions of simultaneous equations [24]. For these reasons, hydrocodes typically use explicit methods [6].

In the explicit method, functions at the new time step are determined using known functions from the previous time steps [6]. A typical Lagrangian solution cycle can be seen in Figure 6.

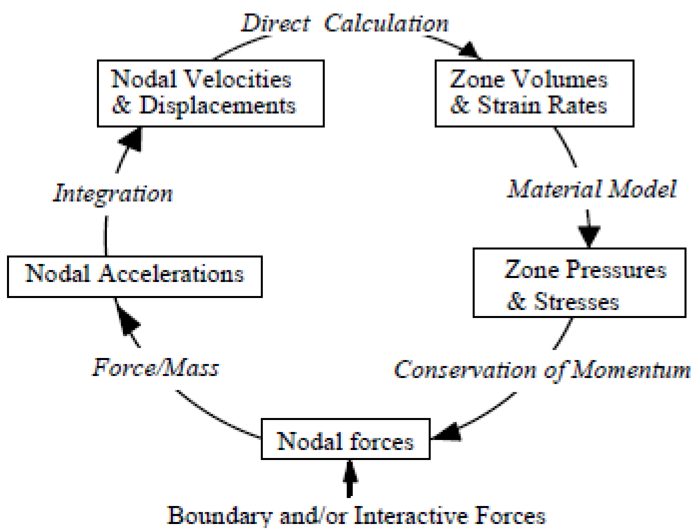

Figure 6 – AUTODYN's explicit Lagrangian solution cycle [12].

From the figure above, it can be seen that a calculation starts with the nodal forces (due to external and/or internal loads). The nodal accelerations, a, are calculated by dividing the nodal force, F, by the nodal mass, m:

$$a = \frac{F}{m} + b \qquad \text{Equation 13}$$

where b accounts for the components of body acceleration. These nodal accelerations are then integrated to determine the nodal velocities. An explicit time integration method such as central difference must be used. For example, the following equation for determining the velocity uses central difference method:

$$V_{n+1/2} = V_{n-1/2} + a_n \Delta t_n \qquad \text{Equation 14}$$

where the subscript n denotes the value at the current time step, n + ½ is at a half time step in the future, and n - ½ is at a half time step in the past. The equation is therefore stating that the velocity at a half time step in the future ($v_{n+1/2}$) is defined based on the known velocity at a half time step in the past ($v_{n-1/2}$) and the current acceleration (a_n), as calculated in Equation 13, multiplied by the current time step (Δt_n). The next step involves using the explicit integration method to derive the nodal displacements:

$$x_{n+1} = x_n + V_{n+1/2}\, \Delta t_{n+1/2} \qquad \text{Equation 15}$$

where x_{n+1} is the nodal displacement at one time step in the future, x_n is the current known displacement, $v_{n+1/2}$ is the value calculated in Equation 14, and $\Delta t_{n+1/2}$ is a half time step in the future [11].

The nodal displacements and velocities can then be used to calculate the new element volumes and strain rates. The material model (including equation of state, strength and failure) is then used to determine the element pressures and stresses. The conservation of momentum equation is then used to convert these pressures and stresses into nodal forces that may be used in the next solution cycle. Time would then be advanced a relatively short amount (time step) and the calculation would continue for the next cycle for the updated time [12].

One major advantage of the explicit method over the implicit method is that the equations are uncoupled and can be solved directly, whereas the implicit method requires solving a set of simultaneous equations. This means that there is no requirement for iteration and no convergence checks are required. Also, it is not necessary to invert a stiffness matrix in the explicit method as all the nonlinearities are included in the force vector [11]. These computational advantages are offset by the need for a critical time step to ensure stability. If the time step is too large, the solution may become unstable, meaning values may grow without bounds as time increases [24]. Therefore, an explicit solution requires numerous small time steps for a complete solution [14].

The critical time step is typically determined based on the Courant-Friedrichs-Lewy stability condition [18]. This condition requires that the time step be limited such that a stress wave cannot pass through the shortest dimension of a cell in one time step. A typical time step limit is defined as:

$$\Delta t \leq f\left(\frac{h}{c}\right)_{min} \qquad \text{Equation 16}$$

where f is a safety factor, h is the shortest dimension of a cell, and c is the local material sound speed in a cell.

2.1.7 Smooth Particle Hydrodynamics (SPH) Solution

When an SPH component is initially filled with particles, the spacing between the centers of particles must be specified. This distance between the initial particle centers is termed the smoothing length, h. The smoothing length therefore determines how many particles will be packed into a component. Since each of the particles act as interpolation points during the solution, a smaller smoothing length will result in greater accuracy. It should be noted that there are SPH algorithms that also allow variable smoothing lengths that can vary locally in space and time [27].

While the Lagrange, Euler and ALE methods rely on a grid to keep nodes connected, the SPH method allows particles to move freely such that the neighboring particles may not always be the same. A kernel approximation is used to determine the neighboring particles and their contribution to the value of a function for a specific particle. The kernel approximation basically takes all of the particles within a defined radius (circle for 2D problems, and sphere for 3D problems) from the center of the particle of interest. Typically, the radius is defined as two smoothing lengths (2h). It then applies a weighting function such that closer particles will contribute more than further particles [27]. For example, if the density of a particle is desired, a formula would be used such that the mass of a particle 0.5h away will contribute more than a particle that is 2h away.

A typical SPH solution cycle is shown in Figure 7.

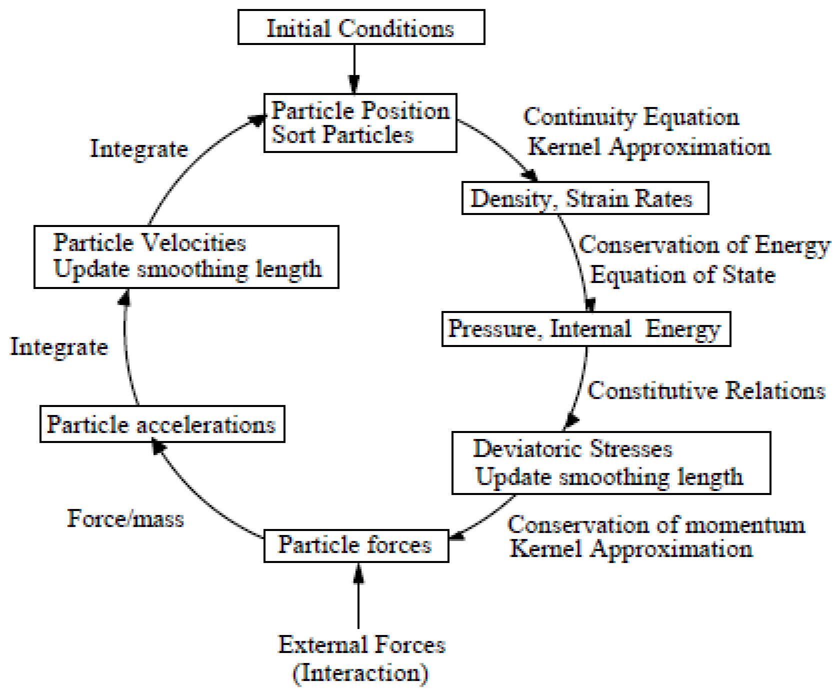

Figure 7 – Typical SPH solution cycle [27].

The solution cycle is very similar to the Explicit Lagrangian cycle, except for the use of the kernel approximations. The solution starts by using the initial conditions to determine the position of the particles. It then sorts through the particles to determine neighbors. A kernel approximation is then used to calculate the density based on neighboring masses, and the strain rates based on neighboring velocities. Conservation of energy and the material equations of state are then used to calculate the pressure and internal energy. The material strength and failure model are then applied to determine the deviatoric stresses. As indicated in the Figure 7, this would be the point in which the smoothing length is updated for a variable definition. A kernel approximation along with the conservation of momentum is used to compute particle forces from the stresses. Any external applied loads/interactions are then added to the particle forces and the total force is divided by the mass, which results in the particle accelerations. The accelerations are then integrated to derive the particle velocities. Once again, the smoothing length may be updated again at this point. Finally, the particle velocities are integrated to determine the new particle positions and the cycle continues for the next time increment.

2.1.8 Discretization Error and Convergence

A numerical simulation can be solved by discretizing time and space. These discrete methods introduce discretization error. Although the Courant-Friedrichs-Lewy condition (Equation 16) ensures stability of the solution in terms of the time step, it does not necessarily minimize discretization error. For this reason, it is necessary to use a convergence criterion to check that the time step sizes and element sizes are small enough to ensure acceptable discretization error [28].

Traditional error convergence analyses assume a relationship between the exact solution, f_{exact}, and the approximate numerical solution, f(h), as follows:

$$f_{exact} = f(h) + Ah^p + HOT \qquad \text{Equation 17}$$

Where A is a constant, h is a measure of the discretization (e.g., mesh size), p is the order (rate) of convergence, and HOT are Higher Order Terms involving powers of h. When the discretization is sufficiently refined (i.e., results are in asymptotic region), the HOT can be neglected and the discretization error, E(h), can be defined as:

$$E(h) = f_{exact} - f(h) = Ah^p \qquad \text{Equation 18}$$

In most cases, the exact solution is not known and therefore there are three unknowns in Equation 17: f_{exact}, A, and p. It should therefore be possible to solve for these unknowns by performing three refinement iterations. With this premise in mind, the Grid Convergence Index (GCI) method has been developed to help objectively define convergence [28].

The method of calculating the GCI is outlined below and its calculation requires several steps. Throughout these calculations the subscripts 1, 2, and 3 refer to three iterations from smallest discretization size to largest respectively (e.g., 1 represents a fine mesh, 2 a medium sized mesh, and 3 a course mesh)

1. Refinement Ratio (r):

$$r = \frac{h_3}{h_2} = \frac{h_2}{h_1} \qquad \text{Equation 19}$$

   For simplicity, a constant refinement ratio will be used, however, it should be noted that the GCI can be calculated for two different refinement ratios (i.e., $h_3/h_2 \neq h_2/h_1$) according to the procedure outlined in [28].

2. Order of convergence (p):

$$p = \frac{ln\left(\frac{f_3-f_2}{f_2-f_1}\right)}{ln(r)} \qquad \text{Equation 20}$$

   where f_i represent the solution value of interest for each refinement iteration.

3. Relative Error (ε_{21} and ε_{32}):

$$\varepsilon_{21} = \left|\frac{f_2 - f_1}{f_1}\right| \quad and \quad \varepsilon_{32} = \left|\frac{f_3 - f_2}{f_2}\right| \qquad \text{Equation 21}$$

4. Grid Convergence Index (GCI_{21} and GCI_{32}):

$$GCI_{21} = F_s \frac{\varepsilon_{21}}{r^p - 1} \quad and \quad GCI_{32} = F_s \frac{\varepsilon_{32}}{r^p - 1} \qquad \text{Equation 22}$$

where F_s is a safety factor. Based on experience, a value of 1.25 is recommended by Roache [29] and should represent a 95% confidence bound such that the following statement may be made:

> The converged numerical solution lies within the interval [$f_1(1 - GCI_{21})$, $f_1(1 + GCI_{21})$], with a 95% confidence level [28]. For example, if $f_1 = 10$ and $GCI_{21} = 0.02$ (i.e., 2%) then the numerical solution lies within the interval [9.8, 10.2] with a 95% confidence level.

5. It is also important to check that the solution is in the asymptotic range by checking the following condition:

$$GCI_{32} \approx r^p GCI_{21} \qquad \text{Equation 23}$$

2.2 Bird Modeling Techniques

Using a bird simulant as opposed to real birds for testing purposes has several advantages. In addition to being cheaper, cleaner, and animal friendly, it also allows for repeatability because real birds will vary slightly in material properties, structure, and geometry [30]. A common practice for bird strike modeling uses a cylinder with hemispherical ends as per

Figure 8 [31]. Nizampatnam [32] performed a comparative study between common bird model geometries and concluded that this shape produced the most consistently accurate pressure profiles when compared to the experimental data available at the time.

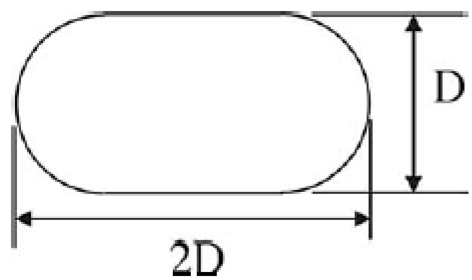

Figure 8 - Bird model geometry [31].

Chickens are commonly used in certification testing of aircraft [33]. Tudor [34] determined that the average density of various chicken parts was 1.06 g/cm^3. However, the average density of an entire chicken was determined to be between 0.90 g/cm^3 and 0.95 g/cm^3 [33]. A value of 0.95 g/cm^3 was also reported in [5]. From these results it was inferred that the solid parts of a chicken have an average density of 1.06 g/cm^3, but the voids and cavities in a chicken result in a lower average total density [33]. The industry standard therefore uses a conservative density of approximately 0.95 g/cm^3 [31]. Using the geometry and density defined above, the dimensions for a 1.814 kg (4 lb) bird can be calculated as having a diameter of 113.42 mm and overall length of 226.84 mm.

Wilbeck and Rand [33] tried various materials to create a synthetic bird using the geometry shown in Figure 8. The various methods were compared with impact pressures of actual chickens. Their experiments demonstrated that using ballistic gelatin, which has a density between 1.05-1.06 g/cm^3, with phenolic microballoons added to reduce the density to between 0.90-0.95 g/cm^3, realistically reproduces the impact loads caused by real birds.

During a bird strike event, it has typically been assumed that the stresses generated due to the deceleration of the bird greatly exceed its yield strength. In this hydrodynamic regime, the bird can be treated as a fluid and the material density dominates the event instead of the strength. For this reason, a material model for the bird usually only consists of an initial density and an equation of state [5].

One method to calibrate an equation of state for a bird model is the rigid plate method used by Wilbeck in [5]. By using a rigid plate, the bird behavior is isolated from the displacement response of the target [33]. A piezoelectric quartz pressure sensor is flush mounted at the center of the rigid plate and the bird is launched such that it hits the center of the plate with minimal misalignment in terms of pitch and yaw. The result is a pressure profile that can be divided into four phases: shock, release, steady-flow, and termination as shown in Figure 9 [30]:

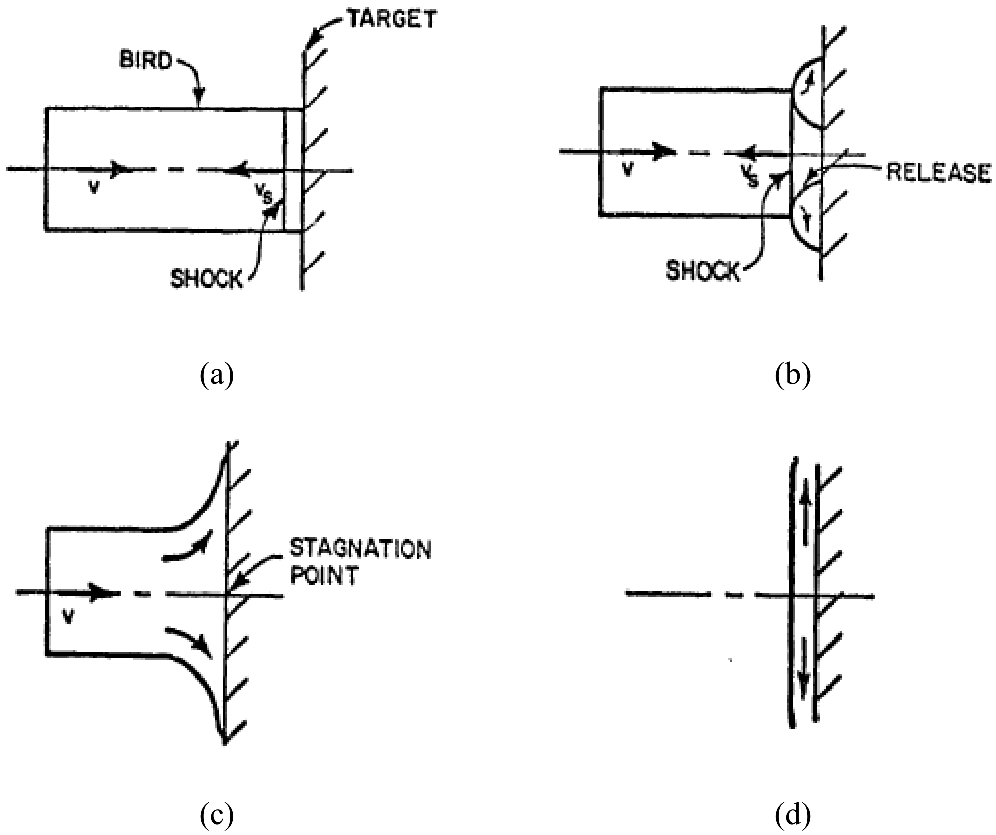

Figure 9 – Bird impact four phases of pressure profile: shock phase (a), release phase (b), steady-flow phase (c), termination phase (d) [30].

The shock phase occurs when the bird first impacts the rigid plate. This causes the particles at the front surface of the projectile to instantaneously come to rest, which creates a pressure wave that propagates through the bird and target. The pressure in the shock compressed region is initially very high. The free surfaces along the edge of the bird result in a stress gradient that causes the material to accelerate outward radially. This results in release waves that travel from the outer edges toward the center of impact. Once the release waves converge at the center of impact, the pressure begins to decay as the release waves weaken the shock. This initial decay is known as the release phase. After several reflections of the release waves, the speed of the shock will be reduced enough to cause a steady velocity of flowing material that is characterized by a near constant pressure termed the steady-flow phase [5]. The termination phase begins as the end of the bird nears the impact surface. During this phase, the pressures decrease until the free surface at the back of the bird reaches the rigid plate, at which point the impact event is finished [30]. The typical shape of a pressure profile from this type of rigid plate test can be seen in Figure 10.

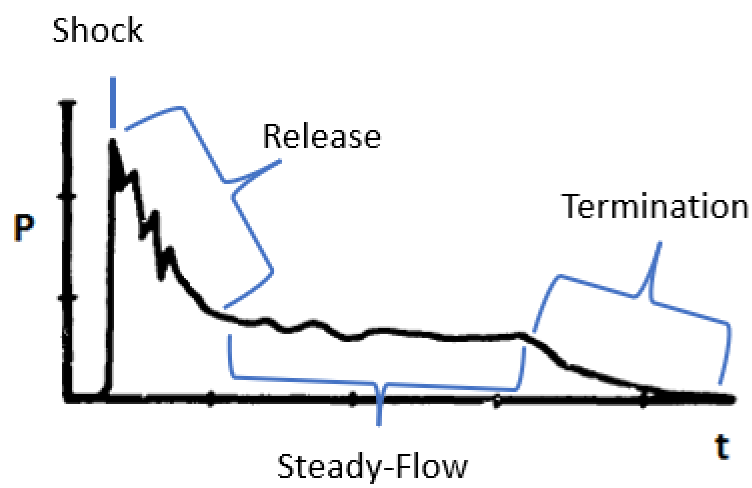

Figure 10 – Typical shape of pressure profile for porous gelatin (950 kg/m^3) impact with a rigid plate at airplane speeds [5].

The equation of state can be calibrated by duplicating the impact conditions with a computer model and then adjusting the EOS parameters until the pressure profile matches the physical tests. Three LS-DYNA equations of state that have been used for bird models include Tabulated, Gruneisen, and Linear Polynomial.

Walvekar [1] used a simplified form of the Tabulated EOS in which he neglected the temperature dependent terms and reduced the EOS to:

$$P = C(\varepsilon v) \qquad \text{Equation 24}$$

where P is pressure, C is a constant, and ε_V is the natural logarithm of the relative volume. By creating a table of ten C-values with corresponding ε_V values, it was possible to calibrate the EOS [1]. Doubrava et al. also used a tabulated EOS for their bird model used in a composite part optimization [35].

Mie-Gruneisen equations are commonly used in analyzing shock compressions that reach pressures up to a few hundred GPa [36]. The Mie-Gruneisen equations can be written in many different forms. A typical form used in hydrocode modeling is:

$$P = P_r(v) + \frac{\Gamma(v)}{v}\left(e - e_r(v)\right) \qquad \text{Equation 25}$$

where P is pressure, v is specific volume, and e is internal energy. $\Gamma(v)$ is known as the Gruneisen parameter/coefficient and can typically be found in literature for most common materials. Otherwise, it must be determined through experiments or molecular dynamics simulations [37]. $P_r(v)$ and $e_r(v)$ are known functions of specific volume taken from a reference curve [38].

There exists an empirical equation in shock wave physics known as the Rankine-Hugoniot equation. This equation provides a linear relationship between the shock velocity, U_s, and the particle velocity, U_p. The shock velocity is the speed at which the shock wave travels through the material. The particle velocity is the speed at which the material moves directly after passage of the shock wave front. A typical form of the Rankine-Hugoniot expression is:

$$U_s = C + SU_p \qquad \text{Equation 26}$$

where C can be approximated by the bulk sound velocity and S is an experimentally determined material constant [39]. Typically, an impact experiment, such as those described by Isbell et al. [40] is used to generate a shock velocity versus particle velocity plot. From this plot, a linear approximation can be made to where the material constant S represents the slope of the approximation, and C is the intercept of the shock velocity axis [41].

The Mie-Gruneisen equation of state available in most commercial finite element codes allows for a cubic form of the Rankine-Hugoniot expression, which results in an expression for the pressure, P, as follows for compressed materials [42]:

$$P = \frac{\rho_0 C^2 \mu \left[1 + \left(1 - \frac{\gamma_0}{2}\right)\mu - \frac{a}{2}\mu^2\right]}{\left[1 - (S_1 - 1)\mu - S_2 \frac{\mu^2}{\mu + 1} - S_3 \frac{\mu^3}{(\mu + 1)^2}\right]^2} + (\gamma_0 + a\mu)E \qquad \text{Equation 27}$$

and for expanded materials as:

$$P = \rho_0 C^2 \mu + (\gamma_0 + a\mu)E \qquad \text{Equation 28}$$

where ρ_0 is the initial density, γ_0 is the Gruneisen parameter, E is internal energy, S_1-S_3 are the constants for the cubic fit of the U_s-U_p curve, 'a' is the first order volume correction to γ_0, and μ is the compression, which is defined as:

$$\mu = \frac{1}{V} - 1 \qquad \text{Equation 29}$$

where V is the relative volume, which is defined as the volume divided by the initial volume [42]. The linear form of the Rankine-Hugoniot equation can be used by setting the values of S_2 and S_3 equal to zero. Wilbeck used the linear form for water with C = 1482.9 m/s and $S_1 = 2$ for one of his bird models [5].

The Linear Polynomial EOS was used by Chuan in [3]. The equation is linear in terms of internal energy, E, as the pressure, P, is defined as:

$$P = C_0 + C_1\mu + C_2\mu^2 + C_3\mu^3 + (C_4 + C_5\mu + C_6\mu^2)E \qquad \text{Equation 30}$$

where C_0 to C_6 are user defined constants. Chuan reduced this equation to a linear relationship between pressure and compression by setting C_1 equal to 2250 MPa and all other constants equal to zero.

Another bird EOS that is not built into LS-DYNA, and would require a user subroutine to be written, is the Impact Event EOS as implemented by Nizampatnam and laid out in the remainder of this section [32]. This method combines two equations of state developed by Wilbeck [5] to form an equation of state for a homogeneous porous bird model. The two equations of state used are Wilbeck's shock EOS and steady-state EOS. Both are subdivided into equations for water and equations for air. These subdivisions are then combined using a porosity parameter [32].

Wilbeck's shock EOS for water is based on empirical data:

$$\frac{\rho_2}{\rho_1} = \left(\frac{P_2}{A} + 1\right)^{\frac{1}{B}} \qquad \text{Equation 31}$$

where ρ_1 and ρ_2 are the previous density and new density respectively, P_2 is the new pressure, and A and B are defined as:

$$A = \frac{\rho_1 (c_{0,water})^2}{(4k_{water} - 1)} \quad and \quad B = (4k_{water} - 1) \qquad \text{Equation 32}$$

where $c_{0,water}$ is the speed of sound in water (1482.9 m/s) and k_{water} is an experimentally determined constant which has a value of 2 [32].

Wilbeck's shock EOS for air is defined as:

$$\frac{\rho_1}{\rho_2} = 1 - q \qquad \text{Equation 33}$$

where q is defined as:

$$q = \left(\frac{2\bar{P}K_{air} + \frac{\rho_1 \left(c_{0,air}\right)^2}{P_1}}{2\bar{P}(K_{air})^2}\right) - \frac{\left\{\left[2\bar{P}K_{air} + \frac{\rho_1 \left(c_{0,air}\right)^2}{P_1}\right]^2 - 4\bar{P}^2 (K_{air})^2\right\}^{1/2}}{2\bar{P}(K_{air})^2} \qquad \text{Equation 34}$$

and $c_{0,air}$ is the speed of sound in air (340.9 m/s) and k_{air} is an experimentally determined constant which has a value of 1.03, and the ratio of new pressure to the previous pressure is defined as:

$$\bar{P} = \frac{P_2}{P_1} \qquad \text{Equation 35}$$

Wilbeck combined the two shock equations of state using mixture theory:

$$\frac{\rho_{1,porous}}{\rho_{2,porous}} = (1-z)\left[\frac{P_2}{A}+1\right]^{-\frac{1}{B}} + z(1-q) \qquad \text{Equation 36}$$

where z defines the amount of porosity (0 = pure water and 1 = pure air). This equation of state can be simultaneously solved along with the one-dimensional equations of conservation of mass and momentum across a shock to determine the new density and pressure. The conservation equations are defined as:

$$\rho_1\mu_s = \rho_2(\mu_s - \mu_p) \qquad \text{Equation 37}$$

and

$$P_1 + \rho_1{\mu_s}^2 = P_2 + \rho_2\left(\mu_s - \mu_p\right)^2 \qquad \text{Equation 38}$$

where u_s and u_p are the shock velocity and particle/projectile velocity, respectively [32]. The projectile/particle velocity is known from the nodal velocities of the finite element simulation and therefore we have three equations and three unknowns.

Wilbeck's Steady-State EOS uses the same equation for water, as was used in the shock EOS as per Equation 31. However, for air he uses an EOS for isentropic compression:

$$\frac{\rho_2}{\rho_1} = \left(\frac{P_2}{P_1}\right)^{1/\gamma} \qquad \text{Equation 39}$$

Once again, using mixture theory, he combines the equations for water and air, which results in the following expression:

$$\left(\frac{\rho_1}{\rho_2}\right)_{porous} = (1-z)\left[\frac{P_2}{A}+1\right]^{-\frac{1}{B}} + z\left(\frac{P_2}{P_1}\right)^{-1/\gamma} \qquad \text{Equation 40}$$

The steady-state stagnation pressure is related to the velocity of impact by Bernoulli's equation for one-dimensional compressible flow as follows:

$$\int_{P_1}^{P_2} \frac{dP}{\rho} = \frac{{u_p}^2}{2} \qquad \text{Equation 41}$$

Simultaneous solution of the above two equations allows for the determination of the new pressure and density values [32].

Wilbeck's shock EOS performs very well for the shock phase of the pressure profile but performs rather poorly for the steady-flow phase as it was developed with the shock phase in mind. Wilbeck's steady-state EOS is very accurate for the steady-flow phase, but inaccurate during the shock phase as it was developed with the steady-flow phase in mind. The Impact Event EOS was developed by Nizampatnam in an effort to define a single EOS that can accurately represent the entire impact event [32]. Through examination of experimental data, Nizampatnam observed that the steady-flow phase is below 40 MPa for birds of all sizes tested. His EOS therefore used Wilbeck's shock EOS for pressures above 40 MPa and Wilbeck's Steady-State EOS for pressures below 40 MPa. He implemented a 3rd degree polynomial fit using the pressures from each of Wilbeck's EOS to determine whether the pressure is above or below the 40 MPa threshold [32]. Nizampatnam's results showed that the Impact Event EOS performed very well in predicting both the shock phase and steady flow phases of a bird strike impact. It was determined that a porosity value of z = 0.3 or z = 0.4 provided favorable results for his simulations.

As summarized by Hedayati and Sadighi in [43], there have been many more recent published papers regarding bird strike modeling; however, the work by Wilbeck [5] as well as the work by Barber, Taylor and Wilbeck [30] from 1978 have maintained their importance due to their good agreement with the experimental data. Hedayati and Sadighi specifically noted 11 papers that used the same geometry and characteristics for the birds as was first suggested by Wilbeck in 1978 [43]. Hedayati et al. [44] also attempted a model geometry in the shape of a mallard in flight; however, this geometry is not representative of an actual projectile during a certification test and therefore was not considered for this work. Liu et al. used an SPH model with just a Murnaghan equation of state for the simulation of a bird strike at 170 m/s and claimed reasonable results as compared to their own generated experimental data [45]. Zhang and Zhou compared four different material model and EOS combinations and determined the null material model and Gruneisen EOS matched their experimental data the best [46]. Cwiklak et al. determined that bird model based on 10% porosity and a linear polynomial EOS resulted in a pressure profile closest to their experimental results [47]. A new alternative to the SPH method called Finite Element Method-Discrete Element Method (FEM-DEM) Adaptive Transfer Method was proposed by Song et al. and resulted in similar results to the SPH method [48].

2.3 Experimental Data Literature Review

There is not a lot of published experimental data for bird strike pressure profile characterization. Data was generated by the Group of Aeronautical Research and Technology in Europe (GARTEUR); however, the results were not made public [43]. Lavoie et al. performed rigid plate impact tests using a 1kg gelatin bird at 100m/s.

However, they determined that a likely error in the experimental set up invalidated the pressure readings [49]. The largest resource available is from Wilbeck [5] and Barber et al. [30]. They both performed rigid plate experiments with pressure transducers to generate their data. The peak pressure and steady-state pressure versus impact speed results from Barber et al. [30] for varying sizes of chickens are shown in Figure 11 and Figure 12 respectively. The solid line in these figures is the theoretical peak pressure based on Wilbeck's EOS described in section 2.2 [30]. The red numbers in the figures represent an interpolation that was made to get the theoretical peak pressure for 170 m/s. The theoretical peak pressure according to Wilbeck's EOS is 182 MPa and this was an over-prediction as compared to any of the experimental results that occurred. The theoretical steady-state pressure is 14.4 MPa for an impact speed of 170 m/s. This is not a conservative result as there is an experimental result that for a 2kg chicken that was approximately 18.5 MPa at an impact speed of approximately 155 m/s (based on interpolation of the plot).

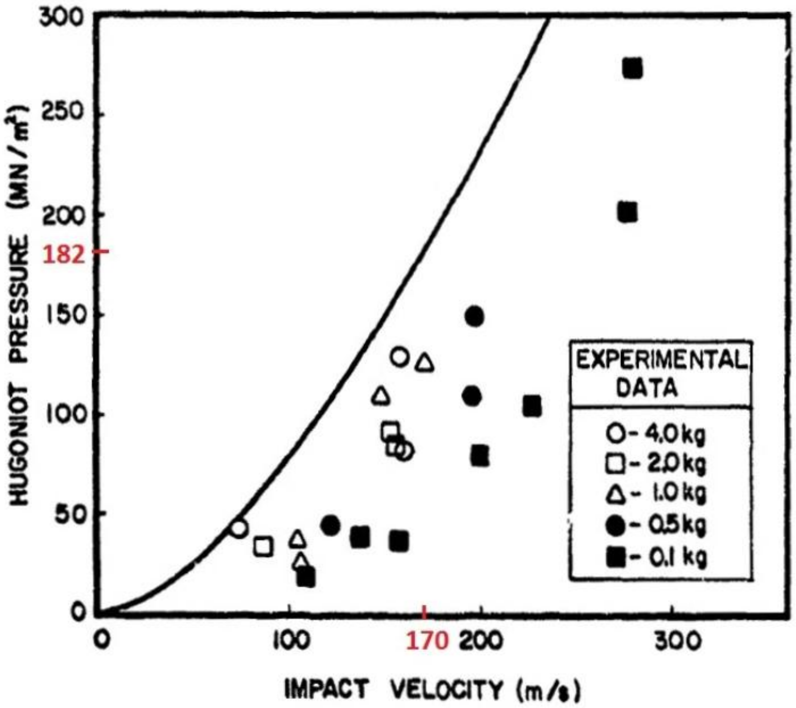

Figure 11 – Peak pressure vs impact velocity from experimental results of chicken impacts and Wilbeck's theoretical calculation for porous gelatin (solid line) [30].

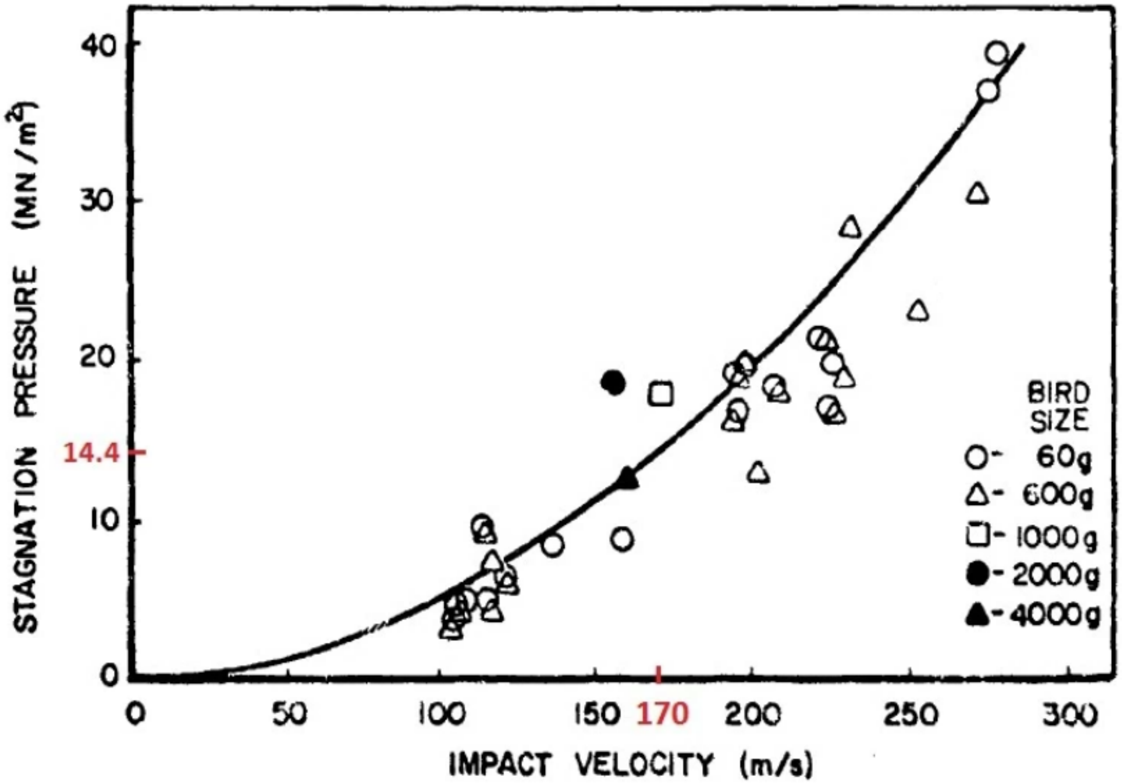

Figure 12 - Steady-state pressure vs impact velocity from experimental results of chicken impacts and Wilbeck's theoretical calculation for porous gelatin (solid line) [30].

Wilbeck performed rigid plate experiments using porous gelatin [5]. The mass of the gelatin bird was not disclosed. The peak pressure vs impact speed is shown in Figure 13. For a speed of 171 m/s, the peak pressure was 88 MPa.

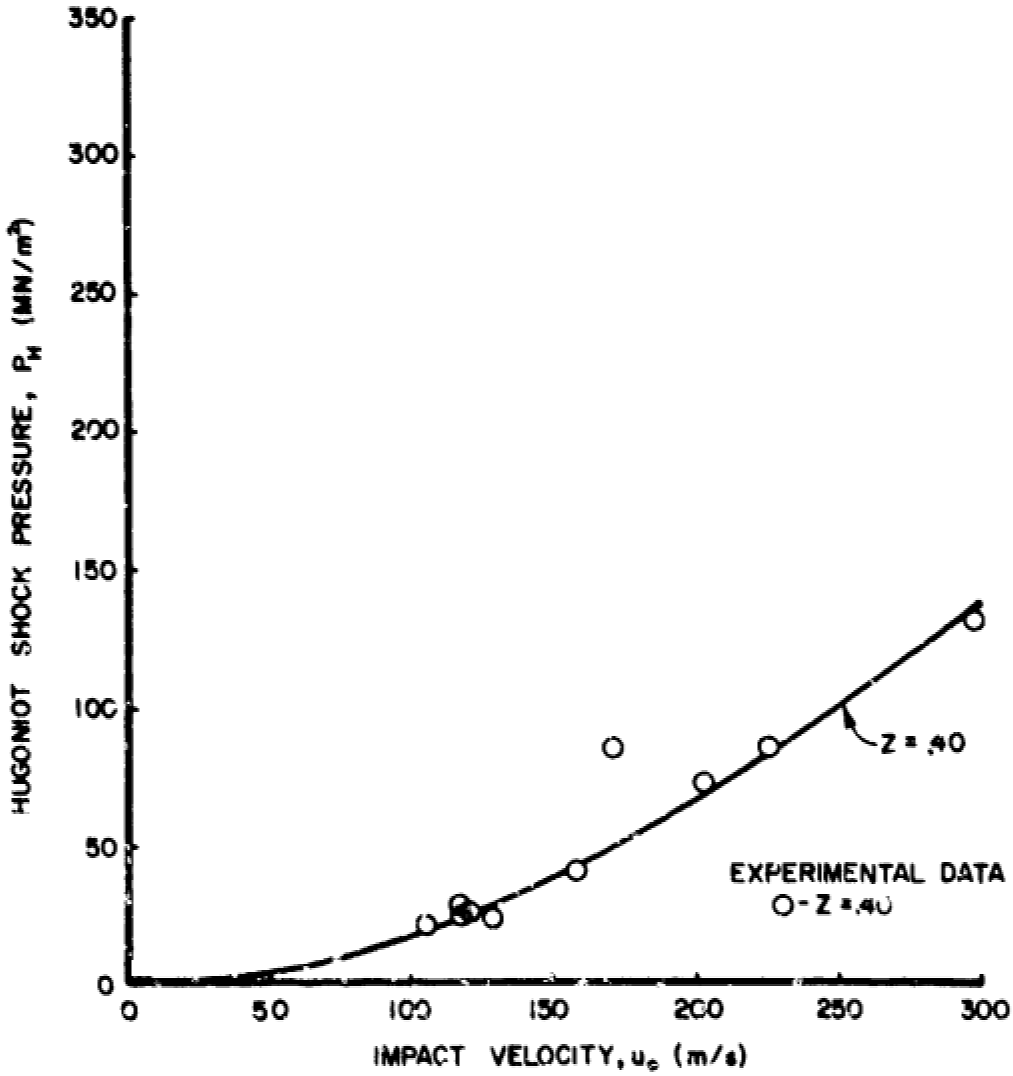

Figure 13 – Peak Pressure vs impact velocity for porous gelatin as per [5].

The steady-state pressure vs. impact speed for pure and porous gelatin is shown in Figure 15 [5]. The experimental result for the porous gelatin was 11.2 MPa at 171 m/s. The theoretical result was 11.3 MPa at 170 m/s.

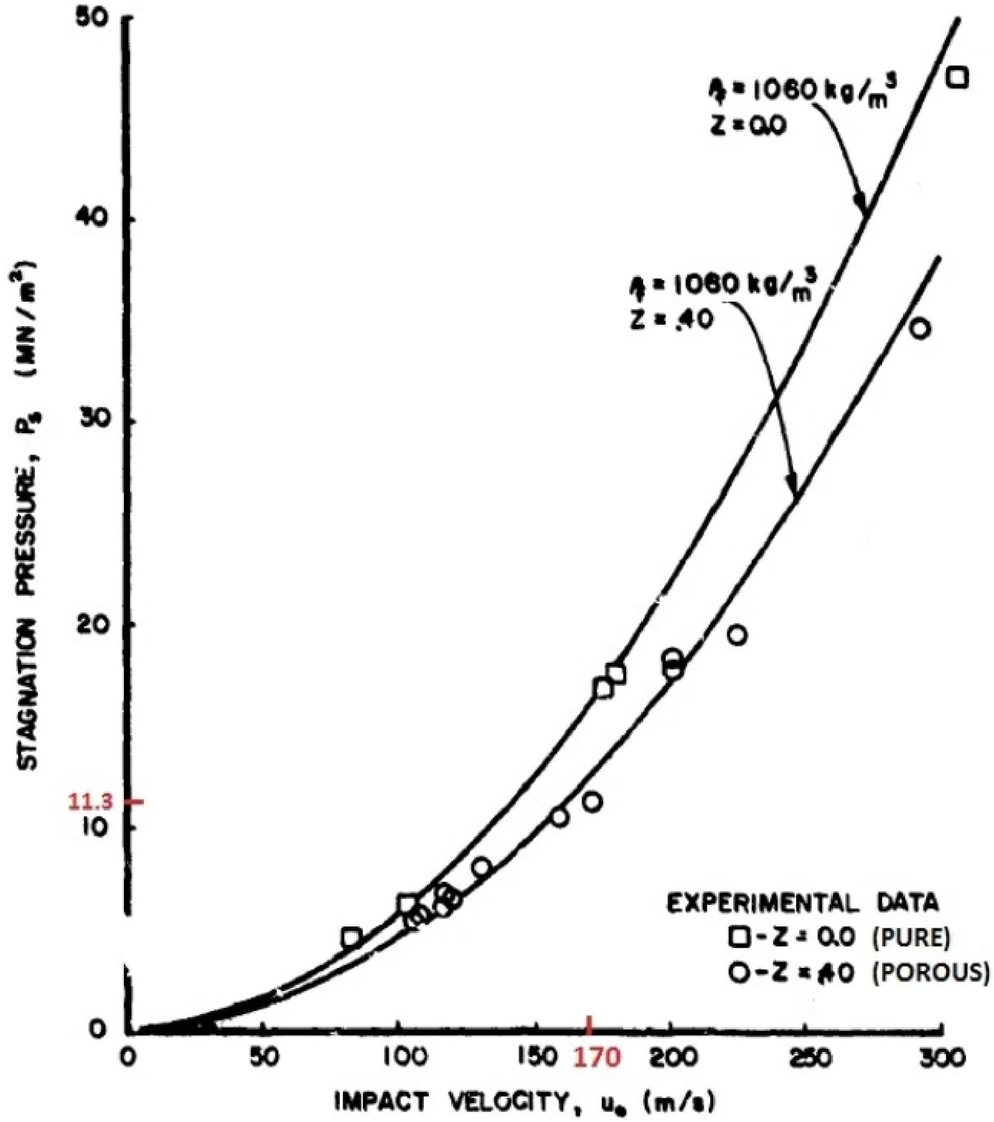

Figure 14 – Steady-state pressure vs impact velocity for pure and porous gelatin as per [5].

Figure 15 shows the pressure profile from the experiment performed by Wilbeck for porous gelatin in [5].

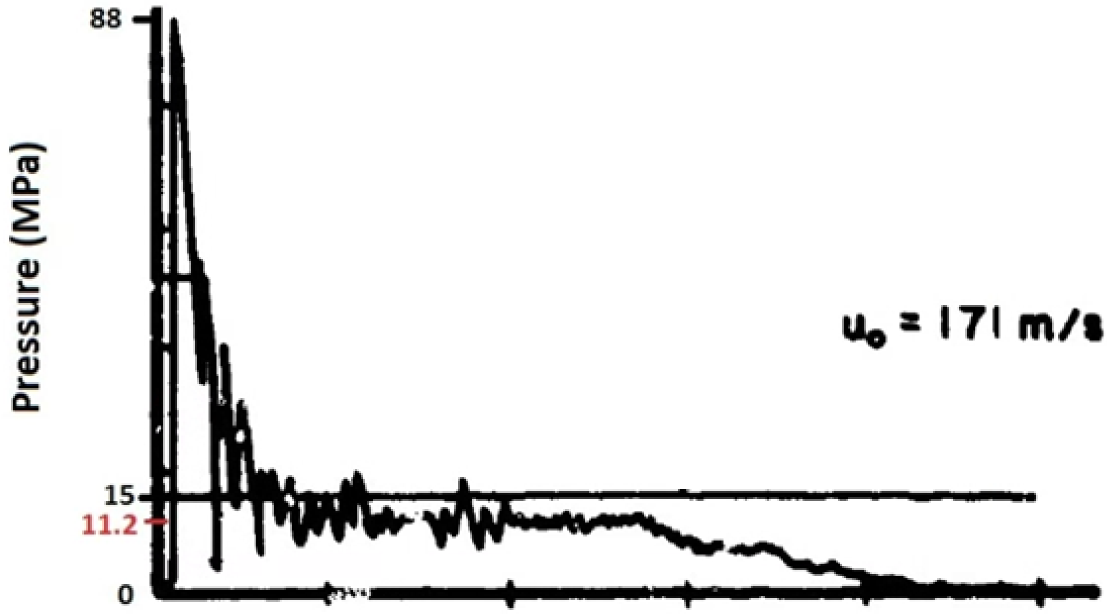

Figure 15 -Experimental result of pressure profile for porous gelatin as per Wilbeck [5] .

It should be noted that Liu et al. performed experiments with real birds using a different type of experimental set up with force sensors, strain gauges, and displacement measurements [45]. Zhang and Zhou [46] as well as Cwiklak et al. [47] also generated their own limited experimental data for validation of their bird strike models. Hedayati and Sadighi summarized that there is an obvious shortage of experimental data for bird strike studies and that most researchers still use the experimental data published in the 1980's for validating their simulations [43]. For this reason, one of the major focuses of this work was on the generation of high-quality experimental data.

3 Gelatin Bird Pressure Profile Characterization

The characterization of the gelatin bird pressure profile was based on the rigid plate method used by Wilbeck [5]. From these tests, pressure profiles were created that could then be analyzed using statistical methods to determine the desired pressure profile for a simulation. The model of the gelatin bird was then created in an attempt to match this pressure profile.

The critical elements of the experimental setup include:

- Foreign Object Damage (FOD) gun
- Gelatin bird simulant
- Sabot
- Rigid structure
- Pressure sensor
- Data acquisition system
- Camera

An explanation and description of their use is provided in this section.

3.1 Rigid Plate Experimental Set Up

The set up for the rigid plate tests is shown in Figure 16.

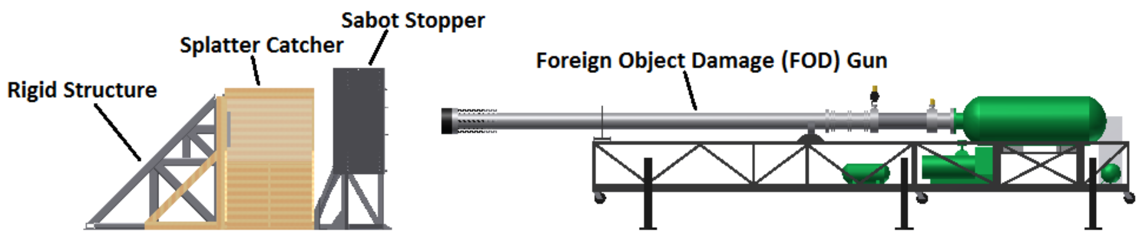

(a)

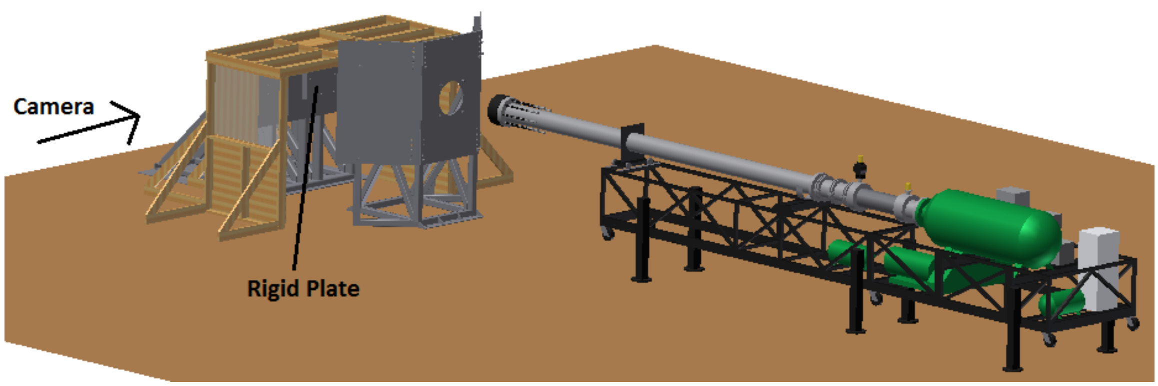

(b)

Figure 16 – Rigid plate test set up. Side view (a) and isometric view (b).

The Foreign Object Damage (FOD) Gun was used to launch the projectile. The Sabot Stopper served the purpose of minimizing the amount of debris from the sabot (e.g., foam) that would hit the target. The Rigid Plate held the sensor(s) and was mounted to a rigid structure. The target area was enclosed in a structure called the Splatter Catcher that contained the splatter from the impact. A high-speed camera was positioned perpendicular to the line of flight in order to record the event.

3.1.1 Foreign Object Damage Gun

A Foreign Object Damage (FOD) gun was used to launch the gelatin bird to the desired speed. This particular FOD gun has a 6 m long barrel with a 250 mm bore. The gun operates using compressed air from a reservoir designed for a maximum air pressure of 1.7 MPa. The gun is capable of firing an 8 kg mass at 200 m/s. Of course, as the mass is decreased, the maximum obtainable speed is increased. The FOD gun is shown in Figure 17.

Figure 17 – University of New Brunswick's Foreign Object Damage (FOD) gun.

3.1.2 Gelatin Bird Simulant

The gelatin bird was created using ballistic gelatin and phenolic microballoons as per Wilbeck and Rand [33]. A mold was created so that the shape of the bird would conform to that of Figure 8. The mold drawings can be found in Appendix A. Microballoons were added to the ballistic gelatin until the weight of the projectile was reduced to 1.814 kg (i.e., a density of 950 kg/m^3).

3.1.3 Sabot

Since the barrel of the FOD gun had an inner diameter of 250 mm and the gelatin bird had a smaller diameter, a device called a sabot was required to hold the projectile centered in the barrel during launch, while also preventing too much air from blowing by and therefore increasing the efficiency of the gun. The standard sabot for this gun consists of a thin cylindrical piece of steel with a hemispherical back on one end and an opening on the front end. A high-density foam was inserted into this metal casing and was machined to the geometry of the gelatin bird and then cut into four segments as shown in the sabot assembly in Figure 18. This figure also shows that the inside of the foam was lined with plastic to prevent the gelatin bird from squeezing back through the foam upon acceleration.

Figure 18 – Sabot assembly.

As the sabot reached the end of the barrel, the outer metal casing was stopped by a feature of the FOD gun called the Sabot Catcher. As the sabot hit the Sabot Catcher it was turned partially inside out and several large springs allow the Sabot Catcher assembly to move forward, which allows the trapped high-pressure air behind it to exit radially from the end of the barrel. Everything inside of the metal casing continued out of the end of the barrel. The front end of the foam pieces was tapered to allow for the aerodynamic forces to separate the foam from the gelatin bird so that they would be stopped by the sabot stopper and would not hit the target plate. The high-speed video had shown that the plastic lining fell back from the gelatin bird and did not affect the pressure profile.

3.1.4 Rigid Structure

For the rigid plate tests, it was necessary to design and build a rigid structure to support the plate that would hold the sensors. The rigid structure was designed using a 4lb bird model with the properties of water, since at this point the bird model was unknown. A speed of 220 m/s was used in the simulations as this is a relatively high-speed design case for a future client of the impact facility. The rigid structure also had to meet the weight restrictions of the 5-ton overhead crane, and had to be large enough to support a leading edge of an aircraft wing for future testing. Various structures with different sizes of plates and structural tubing were simulated and a design was selected that resulted in a maximum deflection of 0.1 mm. This was deemed sufficiently rigid, based on the weight limitations of the structure along with budget and time constraints. Another concern with the rigid structure was that it had to be bolted to a wooden floor. The wooden floor would allow movement no matter how rigid the structure was. To ensure the wooden floor would not affect the results, the structure was designed, modeled and analyzed to ensure that it had enough inertia so that it would not lift off the floor until after the bird impact event was finished (approx. 2.5 ms). The chosen design met this requirement. The rigid structure is shown in Figure 19.

Figure 19 – Rigid structure.

To ensure that the target plate did not plastically deform and that it had adequate rigidty, a simulation was built and run to determine the target plate thickness. Ultimately, a target plate thickness of 101.6 mm (4 in) was selected. The plate was square with a height and width of 609.6 mm (2 ft) and had a hole in the center to accommodate the sensor as per Appendix B. It was later modified to accommodate four sensors as per Appendix C. The rigid plate is shown mounted to the rigid structure in Figure 20.

Figure 20 – Rigid Plate

3.1.5 Pressure Sensor

A PCB Model 109C12 pressure sensor was used during the rigid plate calibration tests. This is a piezoelectric quartz sensor that is designed to measure very fast transient pressure pulses up to 690 MPa. Although most of the specifications were similar between this sensor and its competitors, it did have a higher natural frequency (≥ 400 kHz), which minimizes ringing effects typical of short rise time input pulses. It also had the highest maximum shock value (50,000 g). For these reasons, this particular sensor was chosen. The specification sheet for this sensor can be found in Appendix D. The sensor was connected to a PCB model 480C02 signal conditioner, which both powers the sensor and conditions the signal for data acquisition.

3.1.6 Data Acquisition System

The output from the signal conditioner was connected to two sources for reading/recording. The first source was routed through a National Instruments BNC-2110 shielded connector block to ensure isolation of the signals. This connector block then routed the signals to a National Instruments PXIe-6366 data acquisition (DAQ) device. This device had a sample rate of 2 MS/s, which meant that it could read a sample every 0.5 µs. It had a resolution of 16 bits, which meant the full-scale measurement could be divided into $2^{16} = 65536$ steps. The sensor operated over a range of +/- 7V and therefore it was necessary to set the voltage range of the DAQ to +/- 10V. This corresponds to a full-scale voltage range of 20 V, and the voltage resolution could be calculated as:

$$\frac{20V}{65536} = 3.05e^{-4}\,V \qquad \text{Equation 42}$$

Since the full scale of the senor was +/- 690 MPa over +/-7 V, the pressure resolution using this DAQ was:

$$3.05e^{-4}\,V \times \frac{690\ MPa}{7\ V} = 30\ kPa \qquad \text{Equation 43}$$

The second source to receive the signal from the signal conditioner was a Tectronix MSO3014 oscilloscope. This oscilloscope had a maximum sample rate of 2.5 GS/s, which meant that it could read a sample every 0.4 ns. However, the scope could only record 5 million samples. At the maximum sample rate, the scope would therefore only be able to record 2 ms of data. Unfortunately, the duration of the gelatin bird impact event could be longer than this. It was also desirable to have extra samples before and after the event to account for any delays in triggering and to ensure the event was fully captured. The sample rate was therefore reduced to 625 MS/s, which corresponded to reading one sample every 1.6 ns and allowed the storage of 8 ms of data.

The oscilloscope had 8 bits of resolution and could be set to a range of 10 V, which would correspond to a voltage resolution of:

$$\frac{10\ V}{2^8} = 0.0391\ V \qquad \text{Equation 44}$$

The resolution for the pressure could then be calculated as:

$$0.0391\ V \times \frac{690\ MPa}{7\ V} = 3.85\ MPa \qquad \text{Equation 45}$$

However, the oscilloscope had an option for a quasi-11-bit resolution. This quasi-resolution worked by sampling at the maximum rate of 2.5 GS/s, but only storing the average of the samples at the specified lower sampling rate. The number of samples used in the average was determined by dividing the maximum sample rate by the desired sample rate. For the sampling rate of 625 MS/s, this meant that each stored data point was actually an average of four samples at 2.5 GS/s. The resolution was not straightforward in this case as it was dependent on how many points varied in the calculation of the average. For example, assuming that the first four samples were all 0 MPa, then the first recorded point would be 0 MPa. Now assuming the second set of four samples consisted of two readings of 0 MPa and two of 3.85 MPa. The average of the second recorded data point would have been 1.93 MPa. It had therefore improved the resolution from 3.85 MPa to 1.93 MPa. The best possible resolution using this method would result from only one change of data point. Assuming the first recorded data point was an average of 0 MPa again. Now assuming that the second set of samples consist of three at 0 MPa and one at 3.85 MPa. This would result in an average value of 0.96 MPa having been recorded for the second data point. The best possible quasi-resolution for a sampling rate of 625 MS/s was therefore 0.96 MPa.

Since the Hugoniot pressures occur very quickly, the higher sampling rate of the oscilloscope was desired. The oscilloscopes resolution was adequate for measuring the Hugoniot pressures as they would be in the hundreds of MPa. However, the resolution of the oscilloscope was too large to accurately measure the steady-state values, which were expected to be approximately 15 MPa, and therefore the PXIe-6366 DAQ was used to determine the steady-state values.

3.1.7 Camera

A Photron FASTCAM SA-X high-speed video camera was used to capture the event. The camera was positioned outside of the Splatter Catcher, perpendicular to the line of flight. The high-speed video was used to determine the speed of the gelatin bird, as well as the geometry and orientation prior to impact. A mirror was also positioned below the target plate and oriented at a 45° angle to allow for measurements in an orthogonal plane. The camera was set to 12500 frames/sec and a resolution of 1024 x 1024 pixels to cover a viewable area of 1.8 m by 1.8 m.

3.2 Experimental Rigid Plate Test Results

A total of 17 successful gelatin bird shots were performed. The first nine shots had only one pressure sensor mounted in the center of the plate. After noting the variation in peak pressure, three additional sensors were added for the remaining shots to increase the chances of capturing the true maximum pressures.

3.2.1 Gelatin Geometry Results

Due to the large accelerations during launch, the gelatin bird geometry was different prior to impact as compared to its prelaunch condition. Figure 21 shows the gelatin shape prior to impact for all 17 shots.

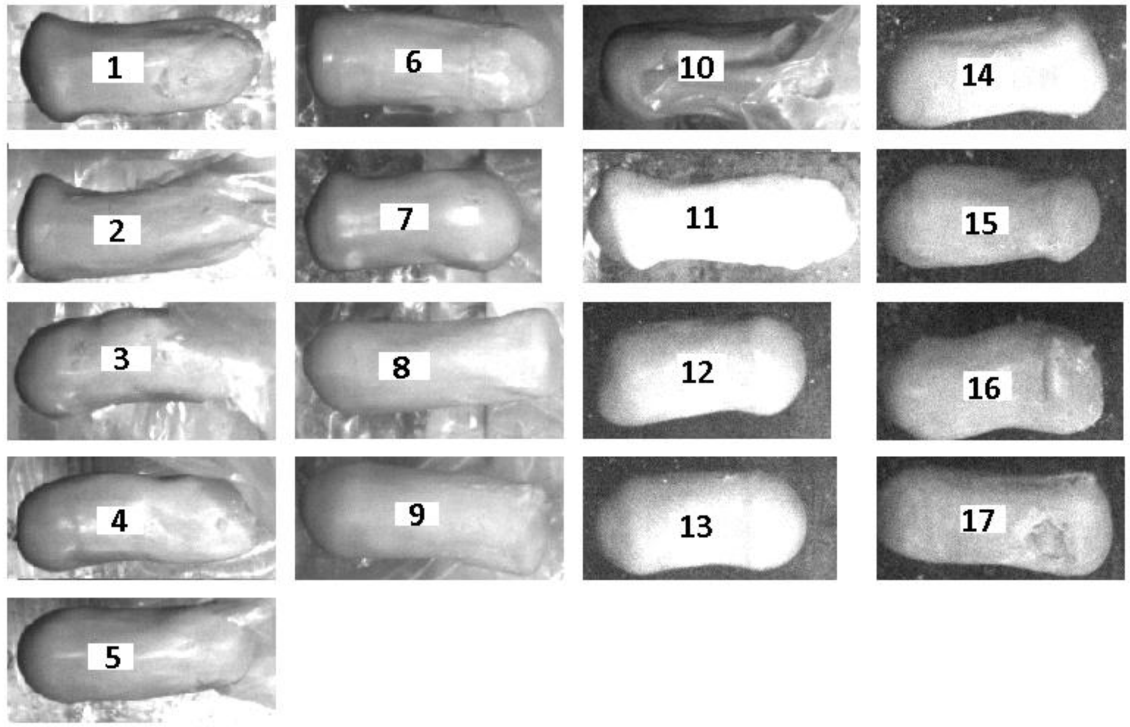

Figure 21 – Gelatin bird geometry prior to impact (direction of flight from right to left).

For each shot, the overall length was measured along with the maximum and minimum diameters just prior to impact. The average of the two diameter measurements was then calculated. The dimensions b and c are defined as the radii of the front and rear curvatures respectively as per Figure 22.

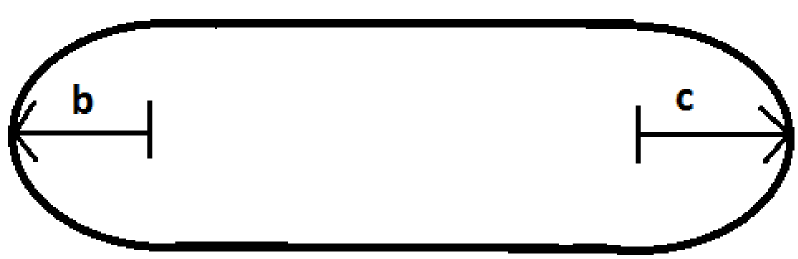

Figure 22 – Front and rear radii of gelatin bird.

A summary of the measurements taken from the high-speed video data are shown in Table 1.

Table 1- Gelatin Geometry Before Impact

Shot	Length (mm)	Maximum Diameter (mm)	Minimum Diameter (mm)	Average Diameter (mm)	b (mm)	c (mm)
1	262	119	97	108	36	50
2	273	117	88	103	23	41
3	273	103	101	102	44	50
4	261	99	99	99	44	52
5	259	107	91	99	55	36
6	271	103	95	99	29	47
7	240	110	97	104	32	44
8	282	101	95	98	36	43
9	271	107	95	101	59	14
10	270	106	93	100	32	48
11	297	120	81	101	41	35
12	220	123	101	112	30	40
13	228	110	101	106	40	45
14	243	108	97	103	32	34
15	238	113	90	102	39	40
16	234	119	101	110	45	39
17	256	114	103	109	50	27
Average	**258**	**111**	**96**	**103**	**39**	**40**
Min	**220**	**99**	**81**	**98**	**23**	**14**
Max	**297**	**123**	**103**	**112**	**59**	**52**

Since the pressure measurements were based on the gelatin geometry upon impact, it was decided to use the average values of the geometry just prior to impact instead of the initial geometry prior to launch for the simulations. It was decided to make the bird symmetric for the simulations because the front and back geometry were similar, and this would avoid potential errors of impacting the bird in the wrong direction. The starting geometry for the simulations would be a cylindrical shape with ellipsoidal ends with dimensions as shown in Figure 23.

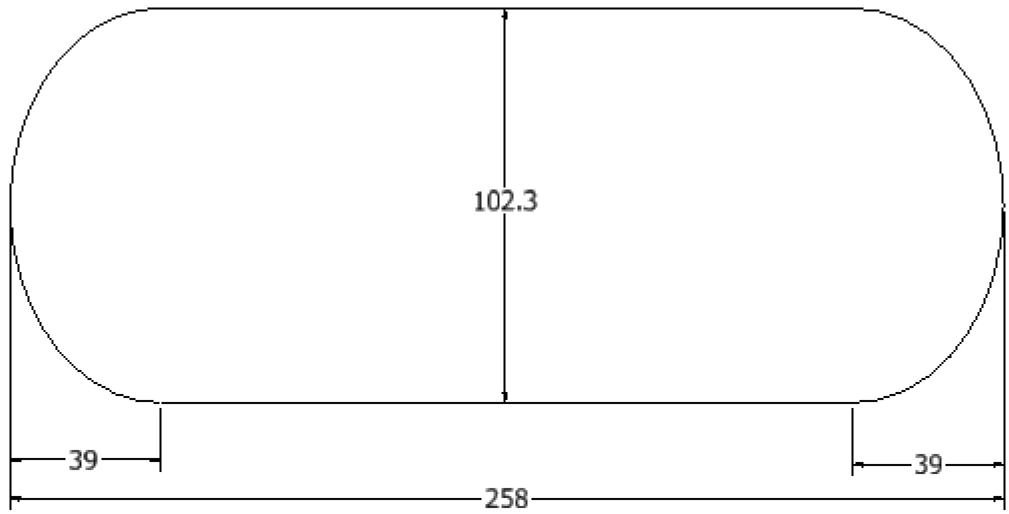

Figure 23 – Gelatin bird simulation starting geometry (dimensions in mm).

A diameter of 102.3 mm instead of 103 mm was used to ensure a density of 950 kg/m^3 and a mass of 1.814 kg.

3.2.2 Pressure Profile Results

The first nine useable shots for the rigid plate tests used only one sensor as per Appendix B. The distorted shape makes it difficult to capture the true peak pressure, since the peak pressure will occur at the point farthest from the free edges (i.e., the center) and that the peak pressure may decrease rapidly with radial location. The measured peak pressures ranged from 151 MPa to 301 MPa for the first nine shots using one sensor. In an attempt to improve the chances of capturing the actual peak pressure, a total of four sensors were used for the remaining tests as per Appendix C.

On some of the pressure profiles there was an offset from zero after the event was over. Figure 24 shows a sample of a pressure profile that had an offset of 7.7 MPa after the event was over. 37% of the readings had a zero offset that was greater than 2 MPa. The majority of the time the offset was negative, however, there were two significant positive offsets as in the case of Figure 24. With no clear cause for where or why the offset was occurring, the sensor manufacturer suggested the offset could be related to temperature effects, and suggested that the use of Kapton foil over the sensor in the future could help to mitigate this issue. There was a large variance in the steady-state pressures due to these offsets, however, when the pressures were corrected by subtracting the offsets, the variance in steady-state pressures was reduced significantly. For this reason, the pressure data was corrected by subtracting the final median offset at the end of the event from all pressure data. A sample of the corrected data is shown in Figure 25. The peak pressure was the only thing that was not corrected for by this offset as it is likely that the mechanism of the offset would not have had time to affect the peak pressure which occurs in such a short duration. Also, the offsets were insignificant compared to the peak pressures (the largest offset was 9 MPa).

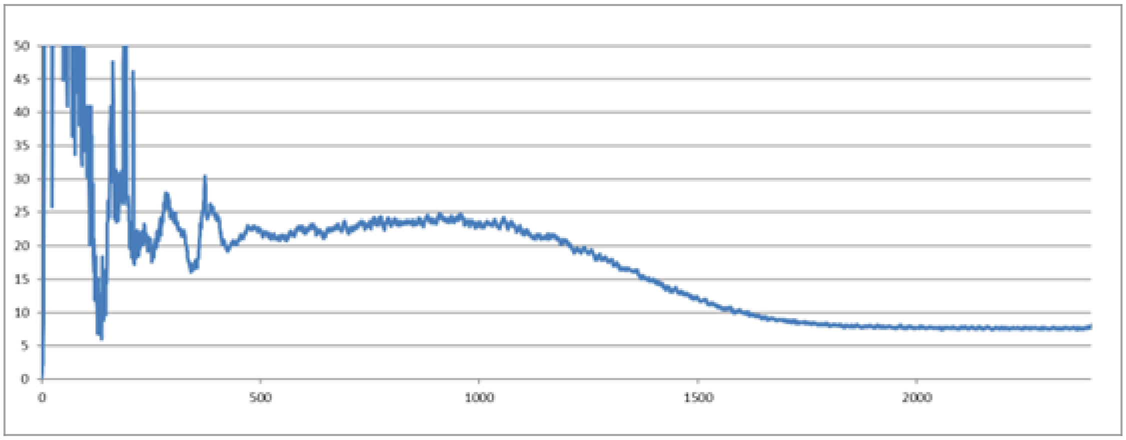

Figure 24 – Sample of pressure profile with zero offset.

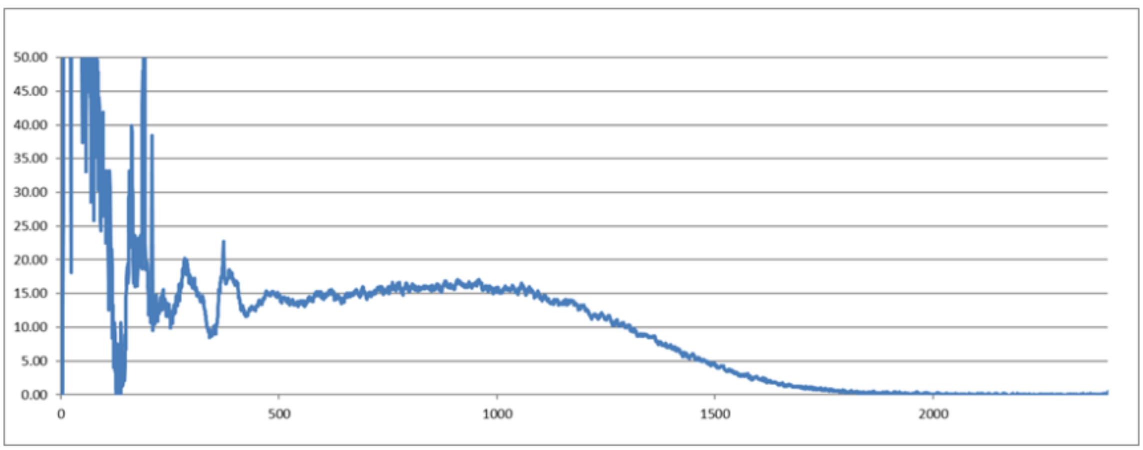

Figure 25 – Sample of pressure profile corrected for zero offset.

Sample pressure profiles from the DAQ can be found in Appendix E. By analyzing this data, a general shape of the pressure profile along with key characteristics is outlined in Figure 26. It should be noted that the experimental pressure profiles were all similar in shape to the experimentally measured shapes observed by other researchers as per Figure 10.

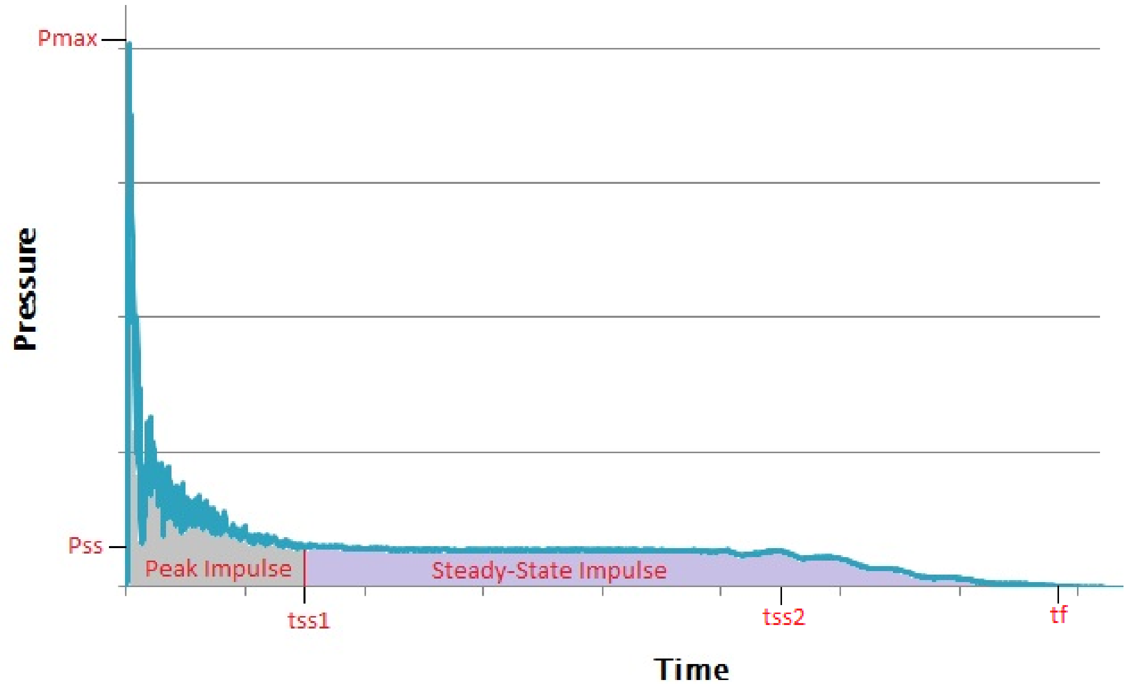

Figure 26 – Gelatin pressure profile characteristics.

The key characteristics that must be captured in the computer model are as follows:

- tss1 = start of steady-state pressure
- tss2 = end of steady-state pressure
- tf = final time when pressure drops back to zero.
- Pmax = maximum pressure (peak pressure)
- Pss = average steady-state pressure taken between tss1 and tss2
- Peak Impulse = the impulse from initial contact to the start of the steady-state (tss1)
- Steady-State Impulse = the impulse from the start of the steady-state (tss1) to the end of the event (tf)

For each shot, all of the characteristics listed above were calculated for all four sensors. All the data was calculated using the DAQ data, due to its better resolution, except for the peak pressure and peak impulse. The peak pressure was determined using the oscilloscope data due to its finer time resolution and hence ability to capture the true peak. The peak impulse was calculated using both the DAQ data as well as the oscilloscope data and the higher of the two values was used. This was necessary because the peak impulse includes pressures that approach the steady-state and the oscilloscope's relatively poor pressure resolution may have resulted in impulses slightly lower than those calculated using the DAQ data.

For the time characteristics (tss1, tss2, and tf), the minimum and maximum values were used as an acceptable range of times for each event to occur in the computer model. The use of a target range as opposed to a specific target value for the timings was chosen due to the difficulty in matching all parameters of the model exactly. It was decided to focus on the magnitude of the pressures and the impulses while ensuring the timing are within a realistic range. For all other characteristics, the maximum value from all four sensors was first determined. Due to the large variation in pressure measurements, it was assumed that the true maximum pressures are typically not being measured. For this reason, the target values for the remaining parameters were calculated as the 99% population maximum value based on a student t-distribution. It should be noted that the distorted shape of the gelatin prior to impact means that the maximum values of the characteristics may occur on different sensors for a single shot. For example, if the front of the gelatin is distorted slightly upwards, the maximum peak pressure may occur on the top sensor, while the maximum steady-state pressure may occur on the center sensor. The full data analysis can be found in Appendix F. The target values of the key characteristics of the pressure profile for the computer model are summarized in Table 2.

Table 2 – Target Values of Key Characteristics of Pressure Profile for Computer Model

Characteristic	**Target Value/Range**
tss1	105 μs – 271 μs
tss2	654 μs – 1182 μs
tf	1587 μs – 2699 μs
Pmax	376.5 MPa
Pss	17.07 MPa
Peak Impulse	10,632 Pa s
Steady-State Impulse	20,709 Pa s

4 Gelatin Bird Initial Model Creation

Based on the experimental testing and results from Chapter 3, a gelatin bird model was created. The model was developed and implemented into LS-Dyna which is commonly used across various industries for impact simulations.

4.1 Gelatin Bird Geometry and Discretization

The starting geometry for the simulation was based on the shape of the gelatin prior to impacting the plate, as described in section 3.2 with the dimensions shown in Figure 23. Due to the symmetry of this shape, the gelatin bird was simulated using 2D axisymmetric elements. The advantages of the SPH technique in modeling large deformations has resulted in it becoming increasingly popular among the bird strike research community [32]. Anghileri et al. [50] performed a comparison of Lagrange, Euler, ALE, and SPH for bird strike modeling and determined that SPH was the most reliable and feasible method for such an event. Frischbier and Kraus [51] also performed a study that concluded that the SPH method was best for modeling a bird strike event. The rationale for their conclusions is based on overcoming many of the obstacles that the other discretization methods encounter as previously discussed in Chapter 2. For these reasons, the SPH method was chosen for the gelatin bird model.

4.2 Rigid Plate Geometry and Discretization

The rigid plate was modeled using Rigid Wall Planar Finite Elements. These Rigid Wall elements provide a simple and efficient way to treat contact between a rigid surface and a deformable body [52]. When using these types of elements, it is not necessary to consider the material properties of the rigid component, which saves unnecessary calculations and reduces simulation time. A rigid contact algorithm is used with these types of elements. The nodes that may interact with the rigid wall are defined as slave nodes. In this case, every SPH node is a slave node as they may all contact the rigid wall. The algorithm checks every slave node to determine whether it has penetrated through a rigid wall. If this criterion is met, the velocity and acceleration components normal to the wall are set to zero for the penetrating node. The normal force, f_n, is defined as:

$$f_n = m_s a_{ns} \cdot n \qquad \text{Equation 46}$$

where m_s is the mass of the slave node, a_{ns} is the acceleration correction for the slave node, and n is a normal vector with respect to the rigid plane. The acceleration correction for the slave node is defined as:

$$a_{ns} = a_s - \frac{f_p}{m_s} \qquad \text{Equation 47}$$

where a_s is the acceleration of the slave node, and f_p is the penetration force, which is defined as:

$$f_p = \frac{m_s \Delta L}{\Delta t^2} n \qquad \text{Equation 48}$$

where ΔL is the penetration distance, and Δt is the time step [41].

This normal force, f_n, was used to calculate the pressure for comparison with the sensor data acquired during the rigid plate tests. To ensure consistency over the area in which the pressure is measured, two rigid wall elements were used. The first element represented the sensor and therefore had an edge length that matched the radius of the sensor (3.118 mm) so that the total force over the equivalent area of the sensor face would be reported. From this force, the pressure could be calculated by dividing by the area of the sensor face. The second rigid element was simply extended from the top of the first element to a radial distance of 304.8 mm to match the size of the rigid plate.

4.3 Discretization Convergence

As described in section 2.1.8, it is important to minimize the discretization error. For the initial model, the Gruneisen EOS was used with the starting values of C = 1450 m/s and S = 2. A Null material strength model was used which enables an EOS to be used with just an initial density and an optional viscosity based deviatoric stress term as defined below:

$$\sigma'_{ij} = 2\mu\dot{\varepsilon}'_{ij} \qquad \text{Equation 49}$$

where μ is the dynamic viscosity and $\dot{\varepsilon}'_{ij}$ is the deviatoric strain rate [53].

The Null material model was used with the density defined as 950 kg/m^3, and the dynamic viscosity set to zero. The peak pressure was used as the convergence variable since it is highly sensitive to discretization and is easy to extract for comparison. The starting SPH size used for the initial convergence check was 2 mm and the starting time step safety factor (TSSFAC) was 0.5. TSSFAC was reduced by a factor of 2 until acceptable convergence was achieved for that SPH size and then the SPH size was reduced by a factor of 2, and the procedure was repeated until there was acceptable convergence in both time step and SPH size. The detailed results of the convergence study are shown in Appendix G. A summary of the results is shown in Table 3 and Figure 27.

Table 3 – Discretization Convergence Summary

SPH Size (mm)	Peak Pressure (MPa)	% Change	Asymptotic Check	Grid Convergence Index
2	658	NA	NA	NA
1	382	-72.2%	NA	NA
0.5	401	4.7%	-1.05	0.38%
0.25	406	1.2%	1.01	0.52%

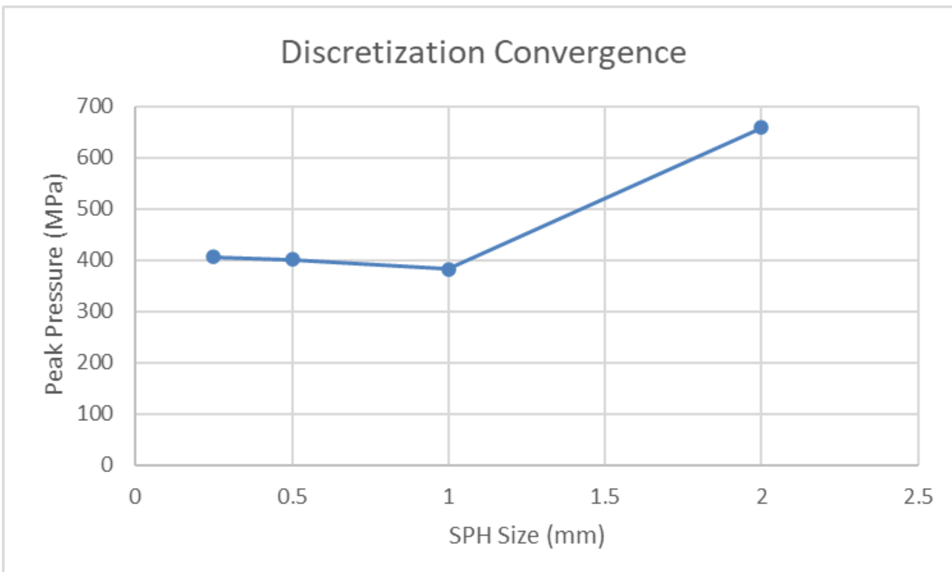

Figure 27 – Discretization convergence summary plot.

To reduce the duration of the simulations to a practical level, it was decided to use an SPH size of 0.5 mm and a TSSFAC of 0.031, since the peak pressure for this case was within 2% of the converged values as per Appendix G.

4.4 Existing Bird Models Check

As per the literature review, there were a few different material models proposed that claimed to satisfactorily match the target pressure profiles based on the data they had available. The data from these past experiments and researchers were based on a single, limited test run for each specific impact condition (bird size and speed). As a starting point for the gelatin model being created, the material models proposed from the literature review were used as an input for simulations. The simulations were run for each of these previous material models to determine whether they could adequately match the target pressure profile from the experimental data obtained and presented in the previous chapter.

Walvekar [1] used a simplified form of the Tabulated EOS as described in section 2.2. The results of the simulation are summarized in Table 4.

Table 4 – Simulation Results for Walvekar Tabulated Bird Model

	Target	**Walvekar Tabulated**	**% Error**
Start of Steady-State, tss1 (μs)	105 – 271	150	0%
End of Steady-State, tss2 (μs)	654 – 1182	1100	0%
Termination Time, tf (μs)	1587 – 2699	2270	0%
Peak Pressure (MPa)	376.5	868.4	131%
Steady-State Pressure (MPa)	17.07	14.62	-14.4%
Peak Impulse (Pa*s)	10632	6624	-37.7%
Steady-State Impulse (Pa*s)	20709	18070	-12.7%
Total Impulse (Pa*s)	31341	24694	-21.2%

Walvekar's tabulated material model over-predicted the peak pressure significantly and under-predicted the steady-state pressure and all impulses.

Wilbeck used the linear form of the Gruneisen EOS for water with C = 1482.9 m/s and S_1 = 2 for one of his bird models [5] as described in section 2.2. The results of the simulation are shown in Table 5.

Table 5 – Simulation Results for Wilbeck's Gruneisen Bird Model

	Target	**Wilbeck Gruneisen**	**% Error**
Start of Steady-State, tss1 (µs)	105 – 271	153	0%
End of Steady-State, tss2 (µs)	654 – 1182	1090	0%
Termination Time, tf (µs)	1587 – 2699	2300	0%
Peak Pressure (MPa)	376.5	406.6	8.0%
Steady-State Pressure (MPa)	17.07	14.21	-16.8%
Peak Impulse (Pa*s)	10632	6828	-35.8%
Steady-State Impulse (Pa*s)	20709	17293	-16.5%
Total Impulse (Pa*s)	31341	24121	-23.0%

Wilbeck's Gruneisen material model predicted the peak pressure within 8%, however it under-predicted the steady-state pressure and all impulses.

The Linear Polynomial EOS was used by Chuan in [3] as described in section 2.2. The results of the simulation are shown in Table 6.

Table 6 – Simulation Results for Chuan's Linear Polynomial Bird Model

	Target	**Linear Polynomial**	**% Error**
Start of Steady-State, tss1 (µs)	105 - 271	167	0%
End of Steady-State, tss2 (µs)	654 - 1182	1070	0%
Termination Time, tf (µs)	1587 - 2699	2300	0%
Peak Pressure (MPa)	376.5	347.9	-7.6%
Steady-State Pressure (MPa)	17.07	14.64	-14.2%
Peak Impulse (Pa*s)	10632	7171	-32.6%
Steady-State Impulse (Pa*s)	20709	17523	-15.4%
Total Impulse (Pa*s)	31341	24694	-21.2%

Chuan's Linear Polynomial material model also predicted the peak pressure within 8% and under-predicted the steady-state pressure and all impulses.

The Impact Event EOS was developed by Nizampatnam in an effort to define a single EOS that could accurately represent the entire impact event [32]. However, this material model requires a user defined material model to be written and it is based on a somewhat arbitrary 40 MPa switch between equations for predicting the peak versus steady-state portion of the event. For these reasons, this material model was not investigated further.

Clearly, based on the simulations using the data from previous researchers, the material models could not adequately predict peak-pressure, steady-state pressure or impulses simultaneously. They all underpredicted the peak impulse by a minimum of 32.6%. As a result, focus was shifted to examining the Gruneisen EOS material model in more detail to better understand the relationships of material model parameters and terms so that future modeling data more closely aligns with all the experimental data.

4.5 Material Model Parameter Sensitivity

As none of the existing proposed material models that were investigated adequately matched all of the target pressure profile characteristics, it was decided to perform a parametric study in an attempt to better tune the pressure profile to match the experimental data.

The study was performed using the Gruneisen EOS parameters C and S, along with the Null strength model dynamic viscosity parameter, μ.

4.5.1 Gruneisen C Sensitivity

The sensitivity to C was examined while holding S constant at 2 and μ constant at 0. The results are summarized in Table 7. Figure 28 shows that peak pressure increases linearly with increasing Gruneisen C, however, the peak impulse actually decreases nearly linearly with increasing Gruneisen C as shown in Figure 29. The explanation for this is that as the Gruneisen C is increased, the speed of sound is increased, which allows the release waves to travel faster and results in the steady-state region beginning sooner (i.e., the peak region does not last as long). Figure 30 and Figure 31 show no clear relationship between steady-state pressure or steady-state impulse and Gruneisen C for the range of values simulated. Based on the Mie-Gruneisen calculation per equation 27, it would be expected that pressure should increase with increasing Gruneisen C.

Table 7 – Sensitivity to Gruneisen C

Gruneisen C	Peak Pressure (MPa)	Start of Steady-State (µs)	End of Steady-State (us)	Final Time (us)	Median Steady-State (MPa)	Peak Impulse (Pa*s)	Steady-State Impulse (Pa*s)
1200	351.5	200	1100	2300	14.68	7779	16996
1450	398	164	1032	2250	14.67	7051	17968
1482.9	406.6	153	1090	2300	14.21	6828	17293
1600	430.2	148	1110	2250	14.28	6639	17808

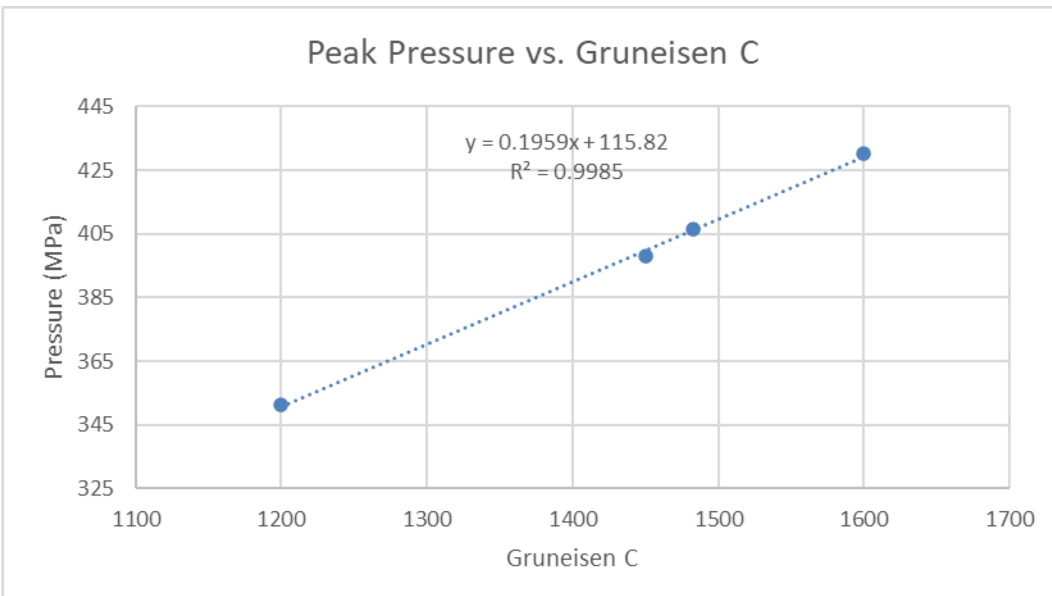

Figure 28 – Relationship of peak pressure to Gruneisen C.

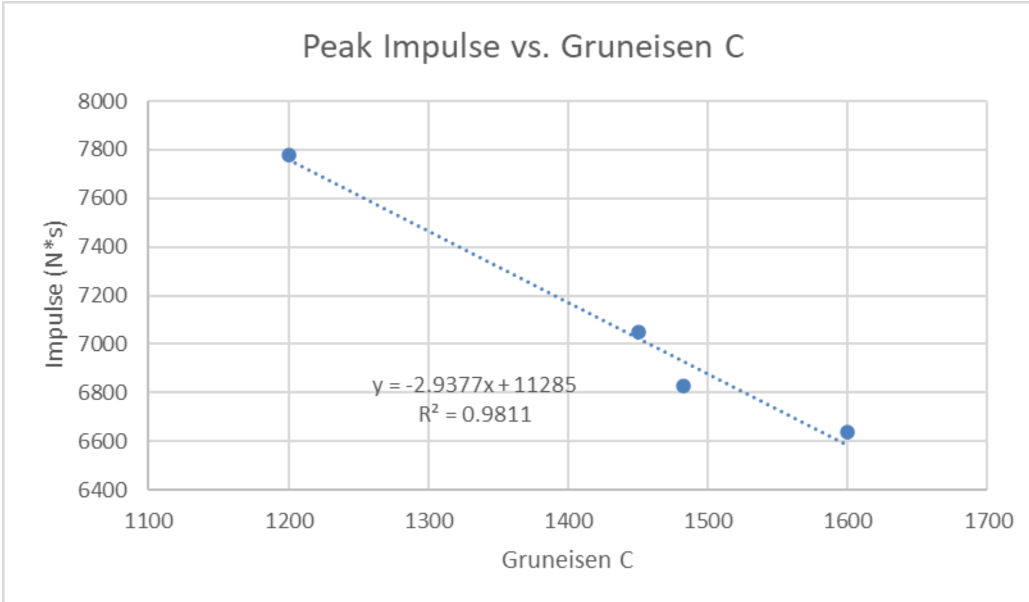

Figure 29 – Relationship of peak impulse to Gruneisen C.

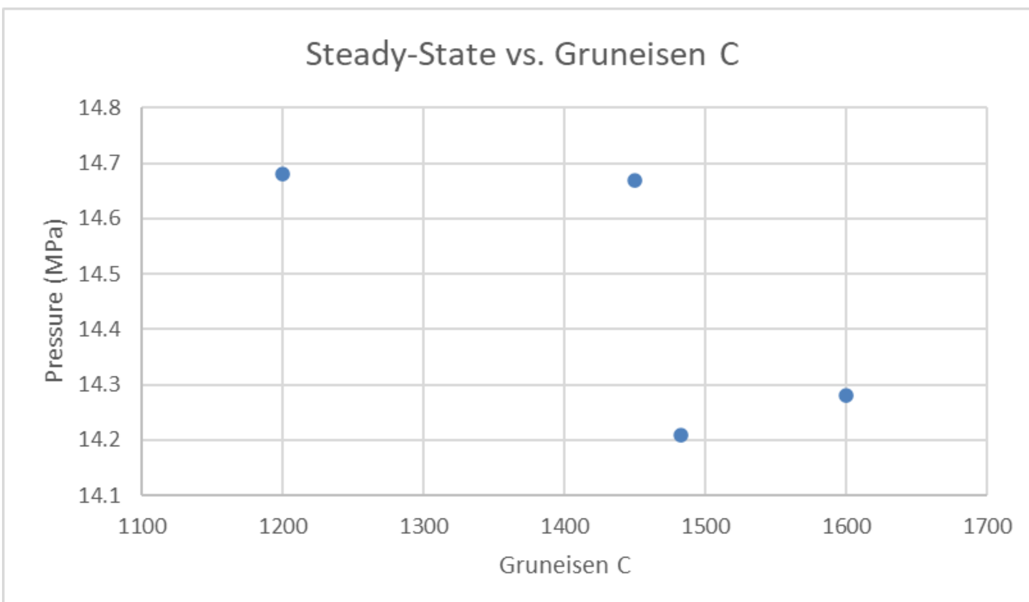

Figure 30 – Relationship of steady-state pressure to Gruneisen C.

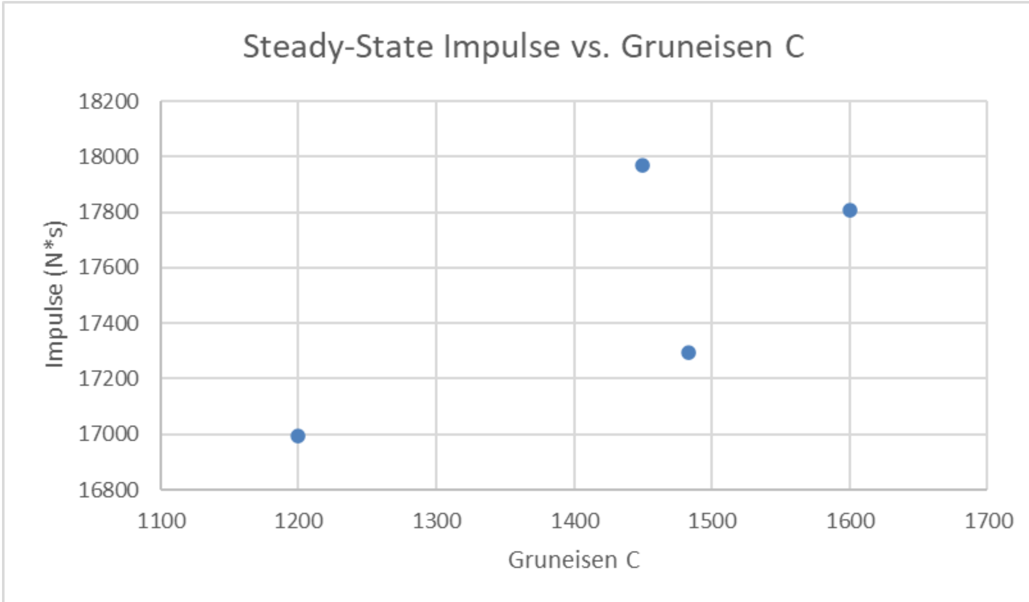

Figure 31 – Relationship of steady-state impulse to Gruneisen C.

With the dynamic viscosity set to zero, relationships between the Grunesien C parameter and peak pressure and impulse was observed. However, no steady-state relationships could be determined. As a result, focus shifted on examining the impact of the dynamic viscosity. While it is common to set it to zero and treat the bird (projectile) as essentially water, other studies have provided hints that viscosity may become important at high strain rates as per the work by Subhash et al [54] which will be discussed in detail in section 4.7.

After careful examination of many simulation results, it was discovered that the Gruneisen parameters have a different effect on the pressure profile when the dynamic viscosity is non-zero. To quantify this change, a new set of simulations were performed with a Gruneisen S fixed at 1 and dynamic viscosity fixed at 1000 Pa*s. This value of dynamic viscosity was chosen as a starting point based on the experimental results from Subhash et al. [54]. The results are summarized in Table 8.

*Table 8 - Sensitivity to Gruneisen C for Dynamic Viscosity of 1000 Pa*s*

Gruneisen C (m/s)	Peak Pressure (MPa)	Peak Impulse (Pa*s)	Steady-State Pressure (MPa)	Steady-State Impulse (Pa*s)
500	370.4	10698	19.97	21535
700	351.9	9116	20.48	22715
1000	417.8	8329	21.12	23678
1200	431.3	8469	19.98	23797
1450	401.1	8925	21.16	22900

The peak pressure increased linearly with Gruneisen C when the dynamic viscosity was zero, however, the trend is not clear when the dynamic viscosity is 1000 Pa*s as per Figure 32.

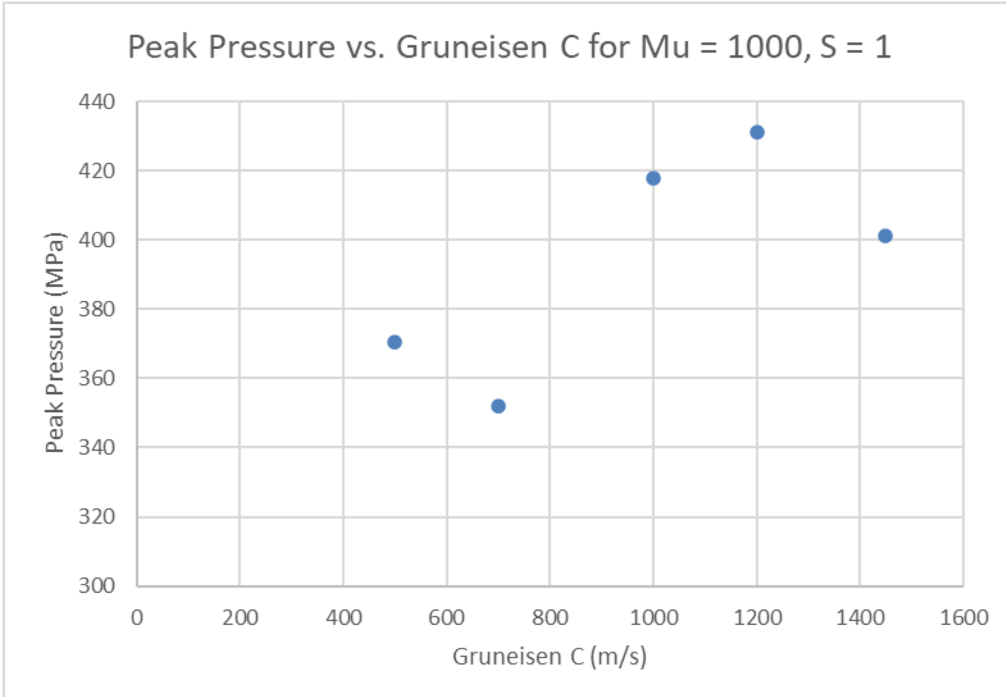

*Figure 32 – Relationship of peak pressure to Gruneisen C for dynamic viscosity of 1000 Pa*s.*

The peak impulse decreased linearly with Gruneisen C when the dynamic viscosity was zero, however, the trend is non-linear when the dynamic viscosity is 1000 Pa*s as per Figure 33.

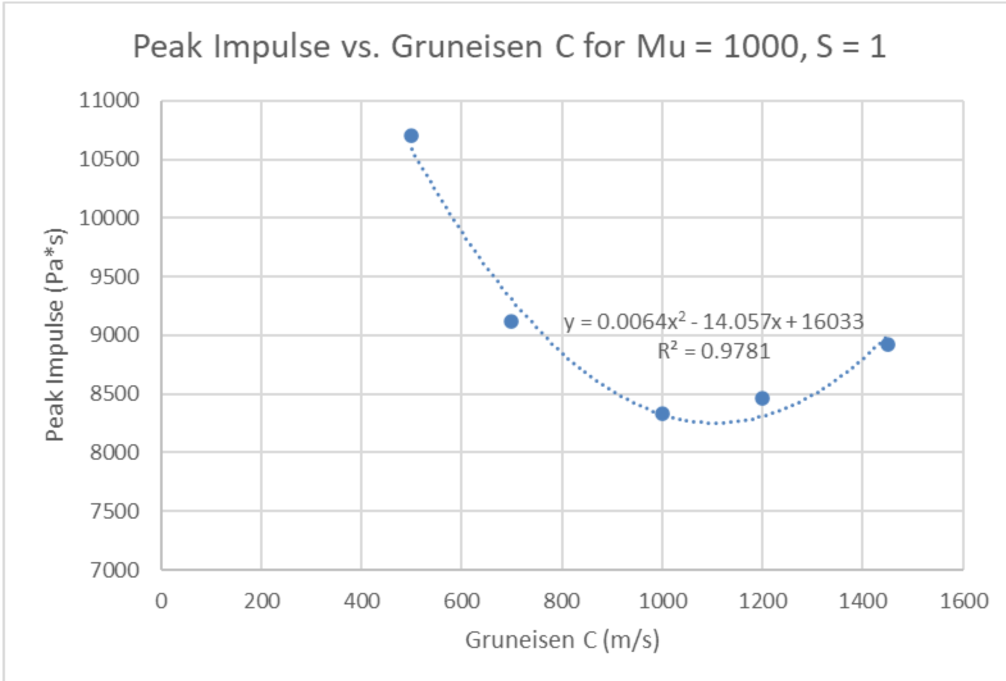

*Figure 33 – Relationship of peak impulse to Gruneisen C for dynamic viscosity of 1000 Pa*s.*

There was no clear trend for the steady-state pressure due to Gruneisen C when the dynamic viscosity was zero, and there is still no clear trend when the dynamic viscosity is 1000 Pa*s as per Figure 34.

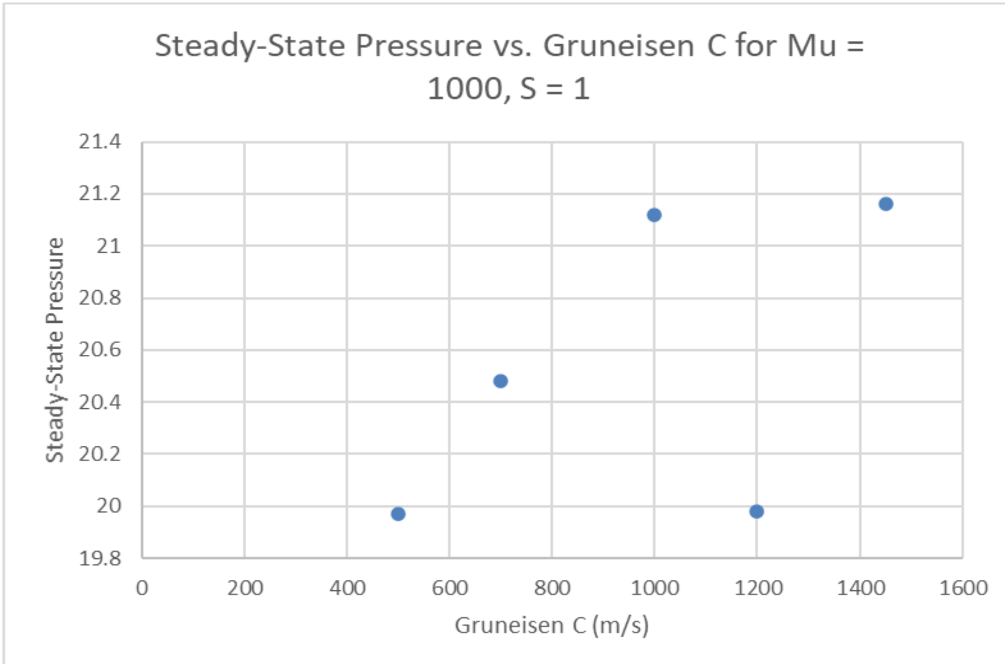

*Figure 34 – Relationship of steady-state pressure to Gruneisen C for dynamic viscosity of 1000 Pa*s.*

There was no clear trend for the steady-state impulse due to Gruneisen C when the dynamic viscosity was zero, however there is a clear non-linear trend when the dynamic viscosity is 1000 Pa*s as per Figure 35.

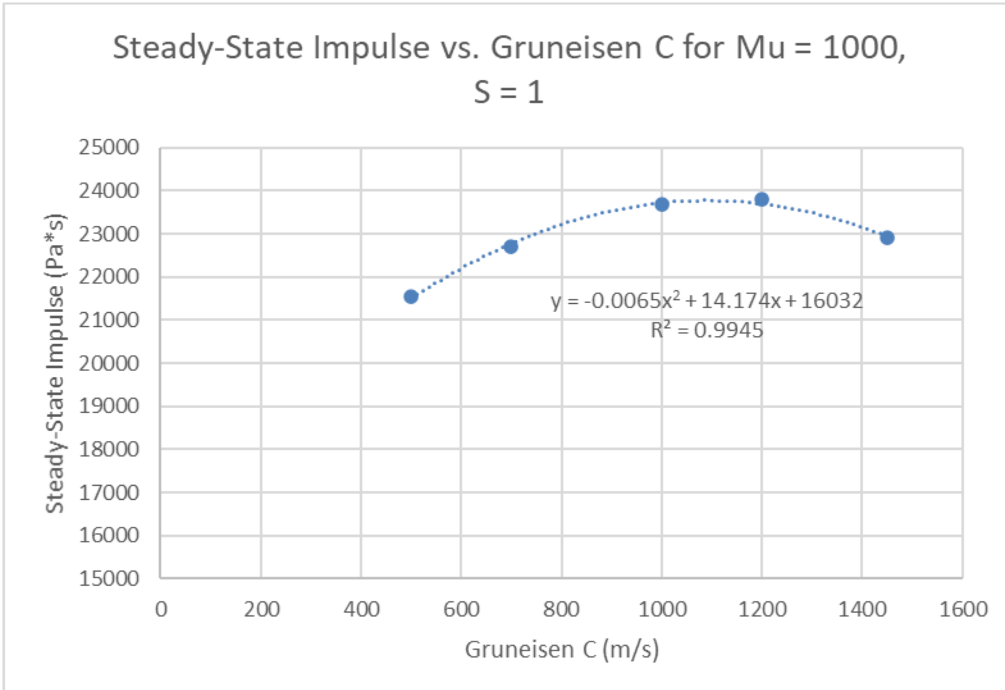

*Figure 35 – Relationship of steady-state impulse to Gruneisen C for dynamic viscosity of 1000 Pa*s.*

The changes in the trends once the viscosity term is applied is likely due to the fact that the viscosity has an effect on the amount of compression that occurs (i.e., the volume change) with time. This relative compression is a factor in the pressure calculation per the Mie-Gruneisen EOS (see equation 27).

4.5.2 Gruneisen S Sensitivity

The sensitivity to S was examined while holding C constant at 1450 m/s and μ constant at 0. The results are summarized in Table 9. Figure 36 shows that peak pressure increases linearly with increasing Gruneisen S and there is no clear relationship with the peak impulse for the range of values simulated as per Figure 37. Figure 38 and Figure 39 show no clear relationship for the range of values simulated for either the steady-state pressure or the steady-state impulse with respect to Gruneisen S. Examining the pressure definition for the Mie-Gruneisen EOS (see equation 27), the Gruneisen S term is in the denominator and the effect of the denominator is dependent on the combination of S and the compression term. During the peak pressure there is likely a near linear trend because the compression term is relatively small. However, in the later stages of the event, as the compression term increases, a non-linear behavior results. The pressure would increase asymptotically as the denominator tends towards zero after which it would reduce in pressure.

Table 9 – Sensitivity to Gruneisen S

Gruneisen S	Peak Pressure (MPa)	Start of Steady-State (μs)	End of Steady-State (us)	Final Time (us)	Median Steady-State (MPa)	Peak Impulse (Pa*s)	Steady-State Impulse (Pa*s)
4	504	169	1020	2300	14.39	7081	17112
2.5	423.2	163	1020	2450	15.04	6837	17789
2	398	164	1032	2250	14.67	7051	17968
1.56	376.7	171	1108	2500	14.06	7459	17277
1	350.1	178	1080	2450	14.03	7358	17110

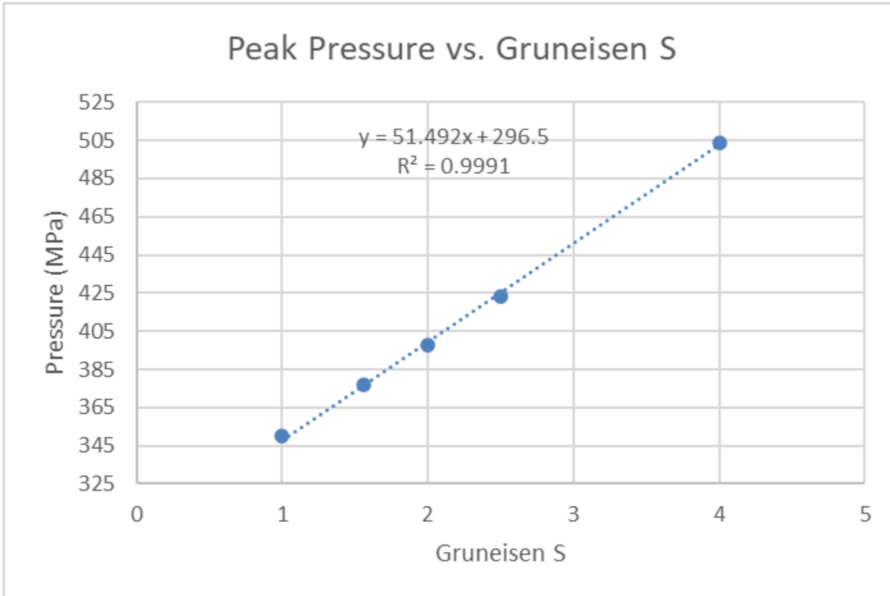

Figure 36 – Relationship of peak pressure to Gruneisen S.

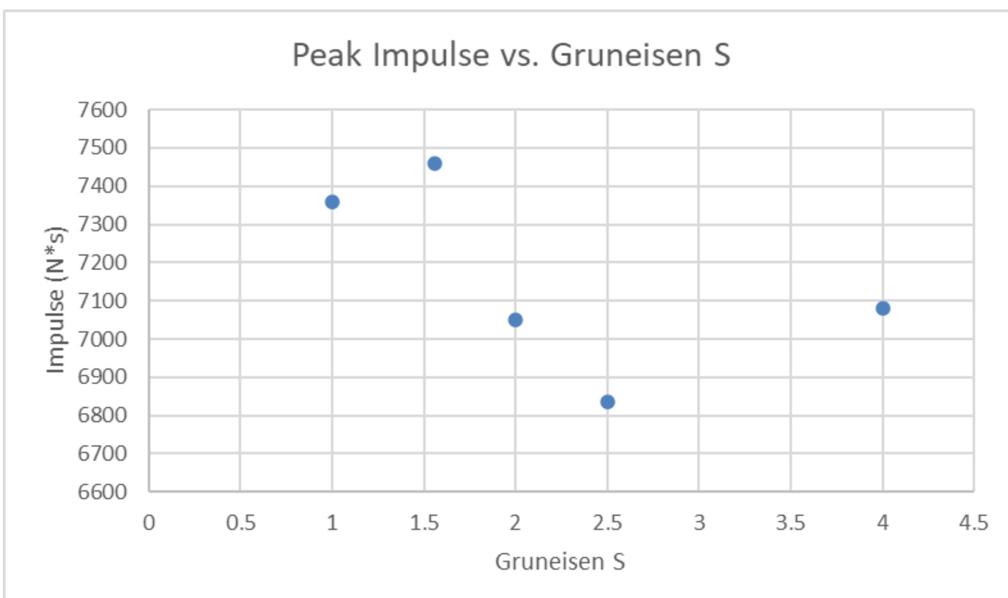

Figure 37 – Relationship of peak impulse to Gruneisen S.

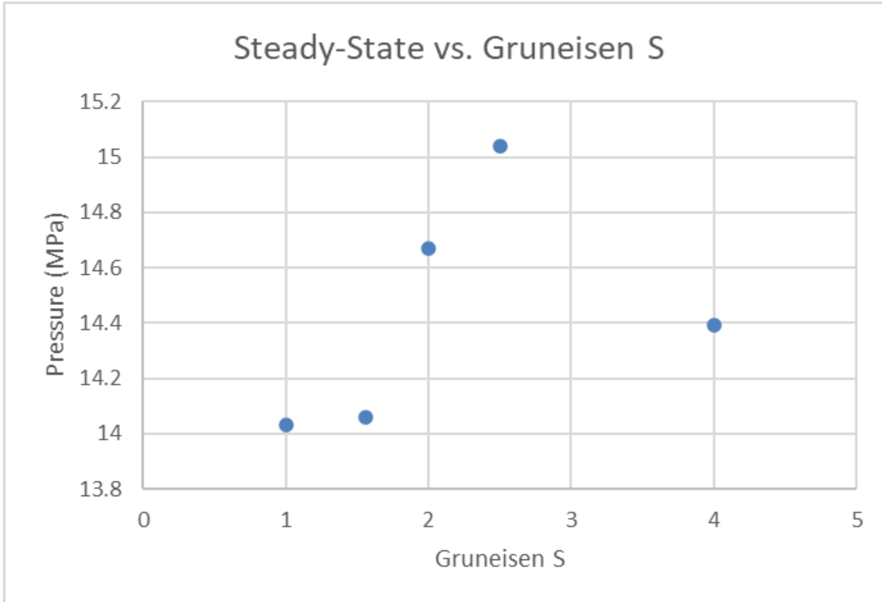

Figure 38 – Relationship of steady-state pressure to Gruneisen S.

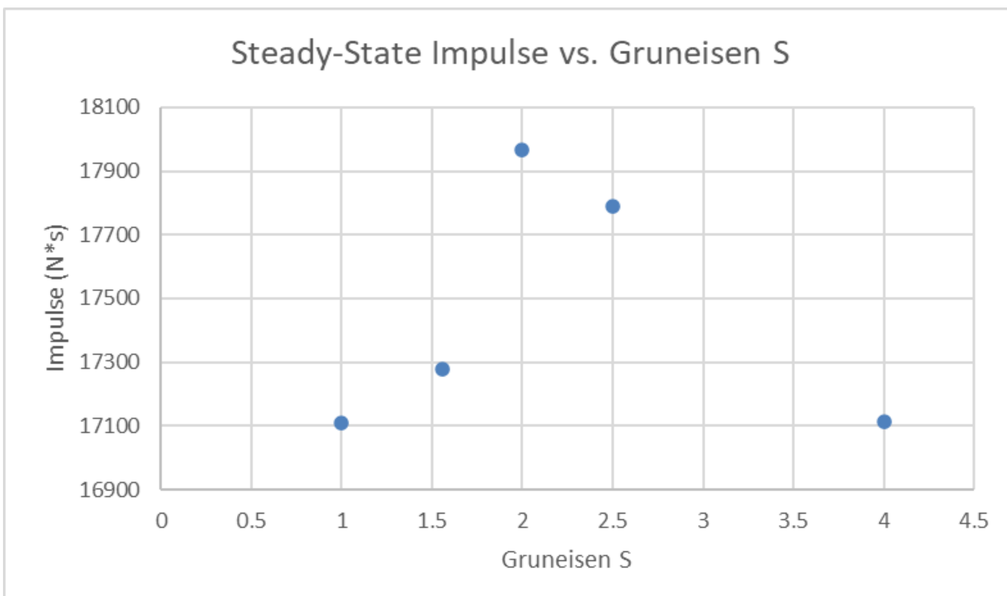

Figure 39 – Relationship of steady-state impulse to Gruneisen S.

As per the case of the Grunseisen C sensitivity, the Gruneisen S behaves differently when the dynamic viscosity is non-zero. To quantify this change, a new set of simulations were performed with a Gruneisen C fixed at 500 and dynamic viscosity fixed at 600 Pa*s. The results are summarized in Table 10. As can be seen in Figure 40 to Figure 43, there is a clear non-linear relationship between all of the pressure components and Gruneisen S when the dynamic viscosity is 600 Pa*s. The changes in the trends once the viscosity term is applied are again likely due to the fact that the viscosity has an effect on the amount of compression that occurs (i.e., the volume change) with time. This relative compression is a factor in the pressure calculation per the Mie-Gruneisen EOS (see equation 27).

*Table 10 - Sensitivity to Gruneisen S for Dynamic Viscosity of 600 Pa*s*

Gruneisen S	**Peak Pressure (MPa)**	**Peak Impulse (Pa*s)**	**Steady-State Pressure (MPa)**	**Steady-State Impulse (Pa*s)**
0	233	10541	16.43	18341
1	223	9830	16.54	19616
5	217.6	8564	17.73	20997
10	374.5	8391	18.52	20360

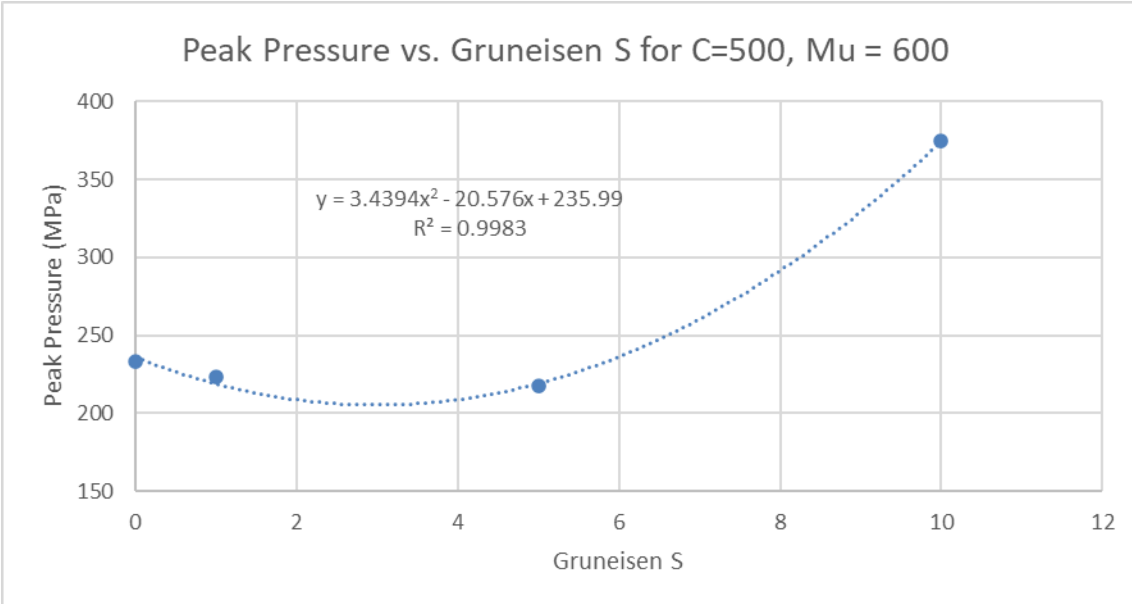

*Figure 40 – Relationship of peak pressure to Gruneisen S for dynamic viscosity of 600 Pa*s.*

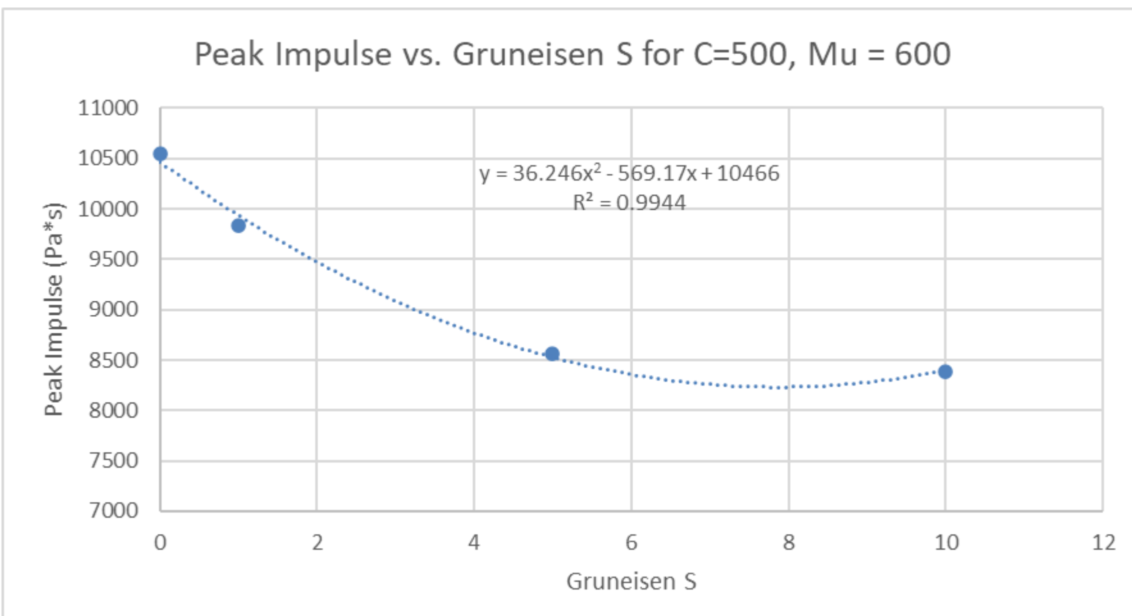

*Figure 41 – Relationship of peak impulse to Gruneisen S for dynamic viscosity of 600 Pa*s.*

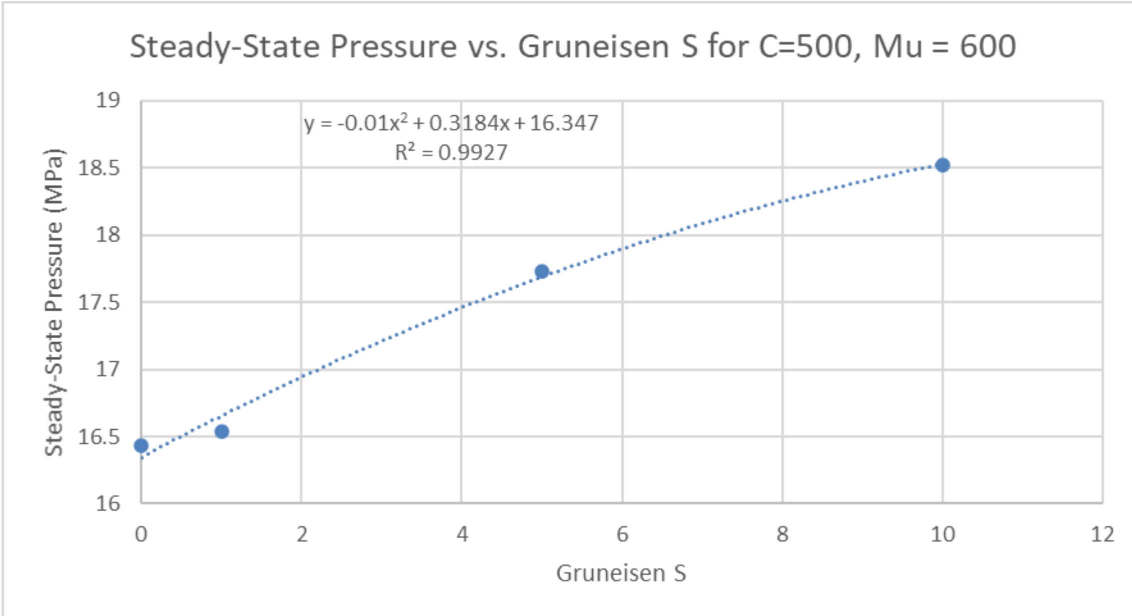

*Figure 42 – Relationship of steady-state pressure to Gruneisen S for dynamic viscosity of 600 Pa*s.*

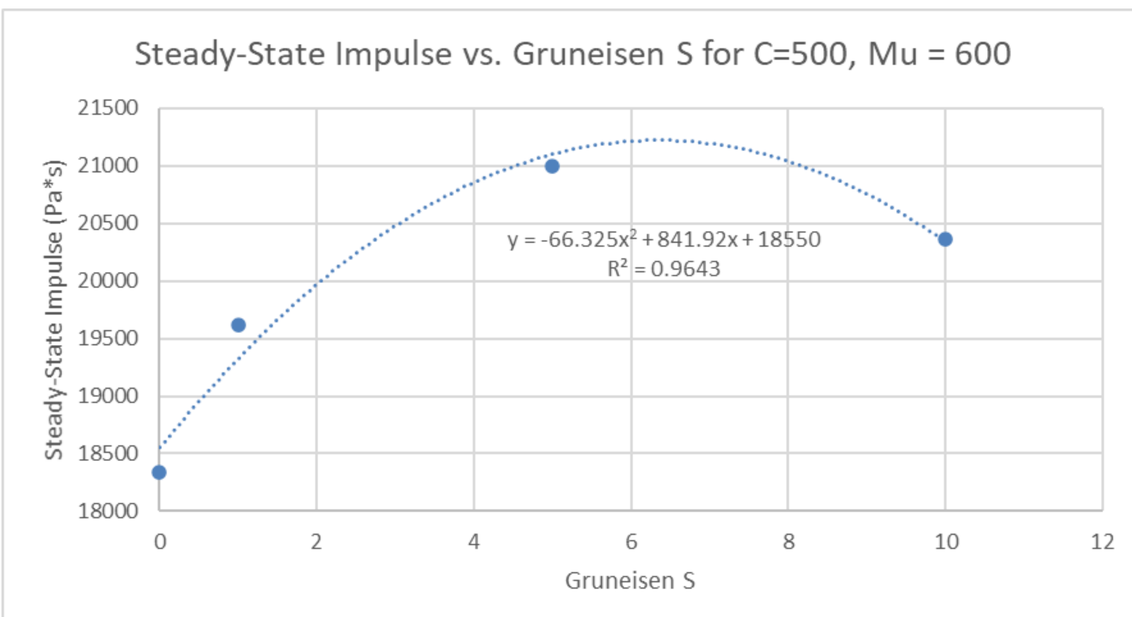

*Figure 43 –Relationship of steady-state impulse vs Gruneisen S for dynamic viscosity of 600 Pa*s.*

4.5.3 Dynamic Viscosity Sensitivity

The sensitivity to the dynamic viscosity, μ, was examined while holding C constant at 1450 m/s and S constant at 2. The dynamic viscosity was varied between 0 and 2000 Pa*s. The results are summarized in Table 11. Figure 44 shows that peak pressure initially decreases with increasing dynamic viscosity up until approximately 500 Pa*s at which point it begins increasing with further increases in dynamic viscosity.

Table 11 – Sensitivity to Dynamic Viscosity

Dynamic Viscosity (Pa*s)	Peak Pressure (MPa)	Start of Steady-State (μs)	End of Steady-State (us)	Final Time (us)	Median Steady-State (MPa)	Peak Impulse (Pa*s)	Steady-State Impulse (Pa*s)
0	398	164	1032	2500	14.67	7051	17980
50	379.5	162	1070	2350	14.06	7223	17509
100	363.8	147	1040	2300	14.43	6809	18132
200	339.1	155	998	2250	15.09	7295	18488
400	311.5	158	1010	2200	16.6	7625	19998
1000	405.6	157	818	2140	21.33	8761	23292
1500	516	160	924	2300	20.9	9791	24154
2000	690.1	164	828	2520	18.77	10864	22325

An additional partial simulation was performed with a dynamic viscosity of 700 Pa*s to help understand the trend of the peak pressure. The peak pressure for this case was 329.3 MPa.

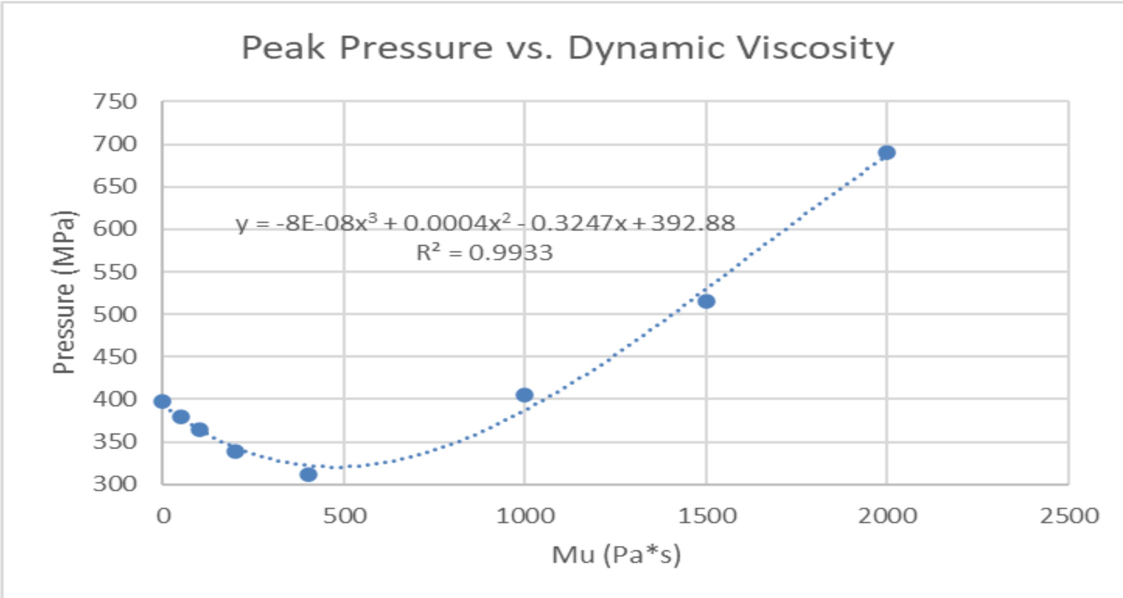

Figure 44 – Relationship of peak pressure to Dynamic Viscosity (μ).

To understand this behavior better, the shape of the peak pressure profile over the initial 5 µs were compared. As can be seen in Figure 45, there is an initial spike in pressure as the bird first makes contact with the wall, after which there is a gradual increase in pressure until the peak occurs at approximately 3.5 µs. As the dynamic viscosity is increased it has a dampening effect which lowers this peak near 3.5 µs. At the same time, the increases in dynamic viscosity are causing the peak pressure that occurs upon initial contact to increase as the bird becomes stiffer and these nodes decelerate at a greater rate, causing the shorter duration initial pressure to rise. At approximately 500 Pa*s, the initial peak pressure exceeds the peak at 3.5 µs. Figure 46, shows this trend for dynamic viscosities between 700 to 2000 Pa*s.

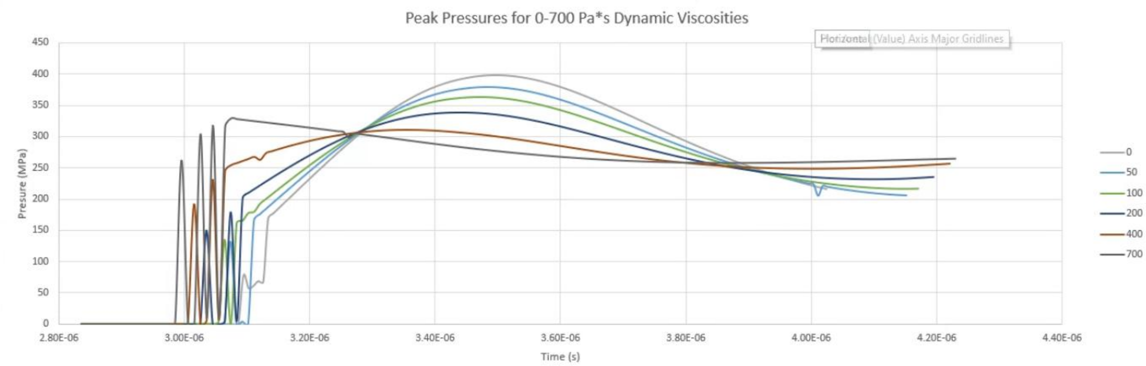

*Figure 45 – Peak pressures for 0-700 Pa*s dynamic viscosities (μ).*

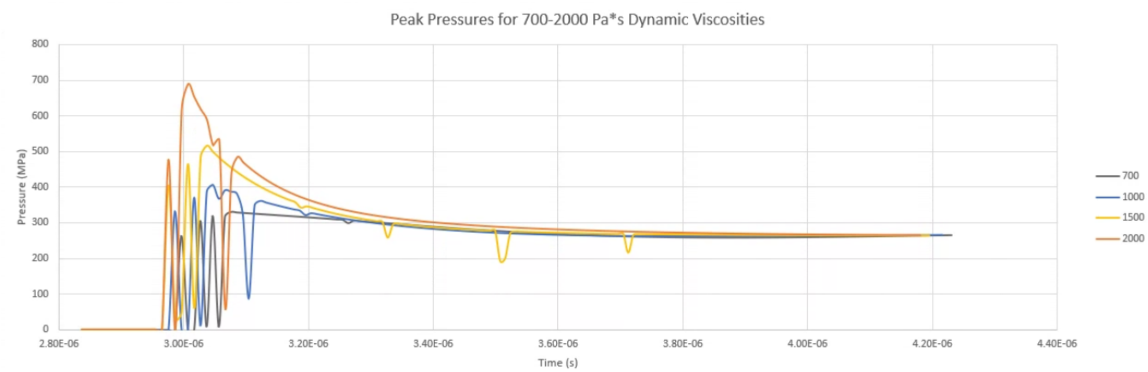

*Figure 46 – Peak pressures for 700-2000 Pa*s dynamic viscosities (μ).*

Figure 47 shows that the peak impulse increases with increasing dynamic viscosity. The 100 Pa*s case did not fit this trend. This could just be due the difference being within the noise of the results for this case.

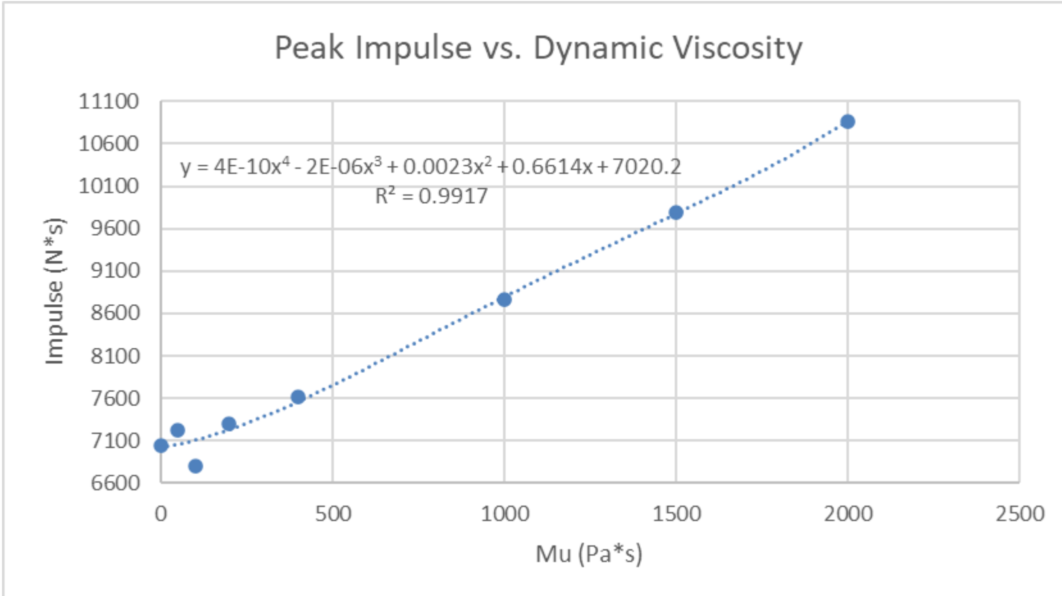

Figure 47 – Relationship of peak impulse to Dynamic Viscosity (μ).

Figure 48 shows that the steady-state pressure initially increases with dynamic viscosity and then somewhere between 1000 and 1500 Pa*s it begins decreasing with further increases in dynamic viscosity. A possible explanation for this can be seen in Figure 49, which shows the shape of the bird at the termination time for various dynamic viscosities. From 1500 Pa*s onward the bird flows outward radially significantly less as the dynamic viscosity is increased. It begins to act more like a solid than a fluid as can be seen most clearly in the 3000 Pa*s case in which the center of the bird does not ever fully compress and flow outward radially. It should be noted that this 3000 Pa*s case resulted in a very noisy pressure profile the results of which were not included in the plots for comparison in this section.

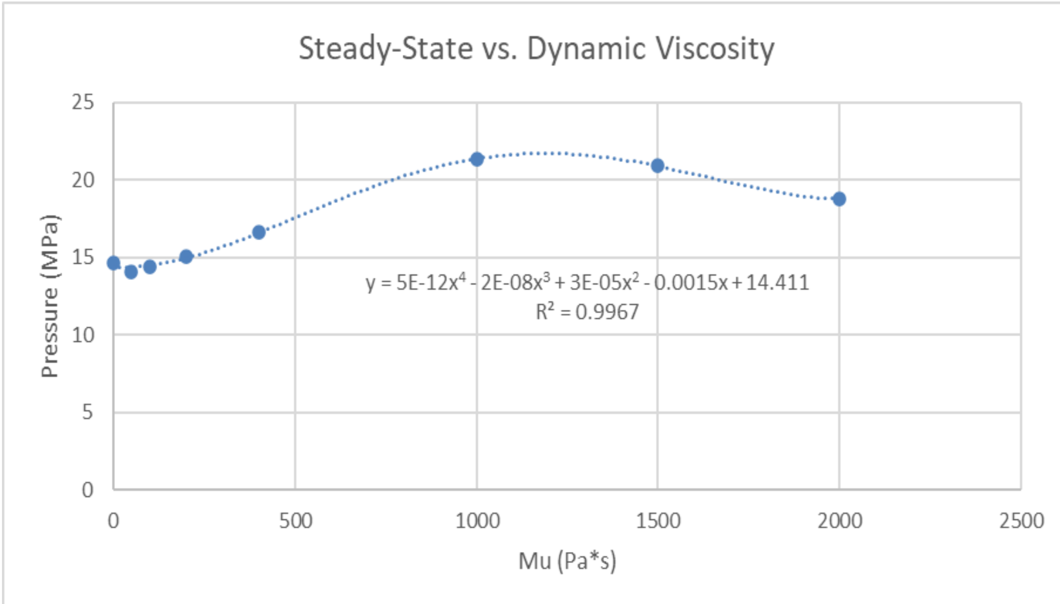

Figure 48 – Relationship of steady-state pressure to Dynamic Viscosity (μ).

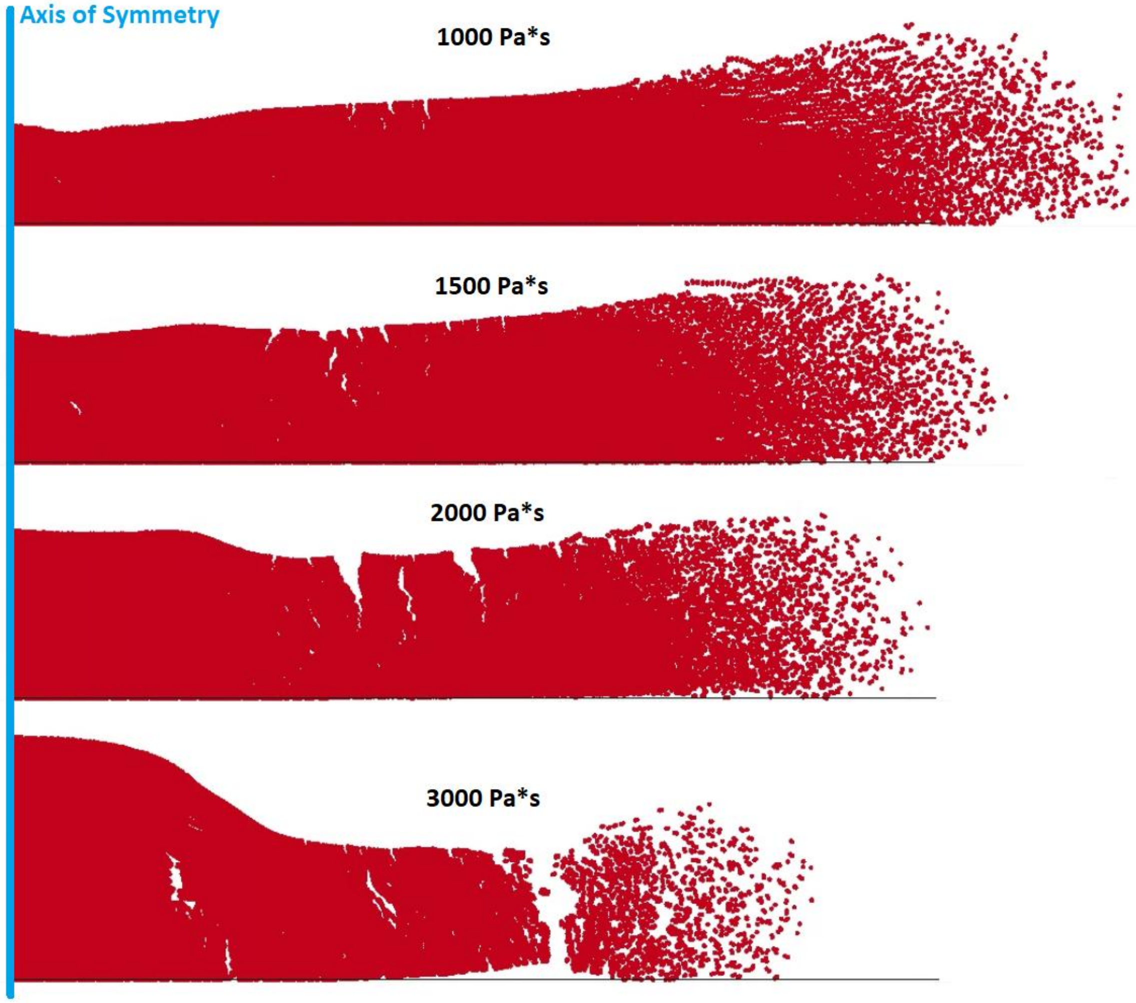

Figure 49 – Shape of bird at termination time for various dynamic viscosities (μ).

Figure 50 shows that the steady-state impulse generally increases with increasing dynamic viscosity up until approximately 1500 Pa*s after which it begins to decrease with further increases of dynamic viscosity. This change in behavior can be explained as per the discussion for the steady-state pressure above.

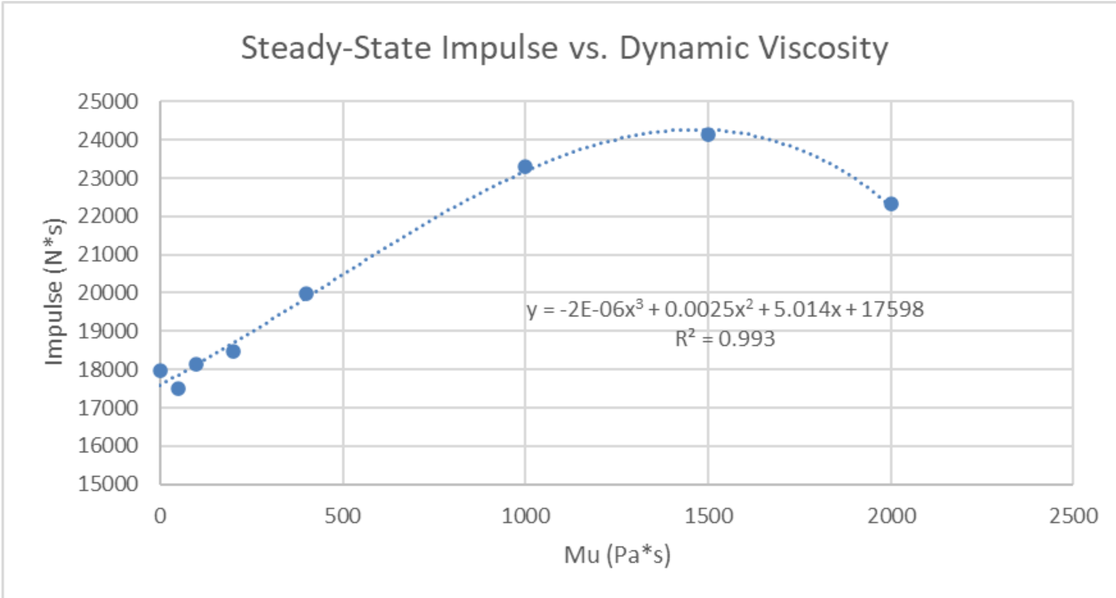

Figure 50 – Relationship of steady-state impulse to dynamic viscosity (μ).

Overall, this study shows that there is complex non-linear but important relationship between the pressure profile and dynamic viscosity.

4.5.4 Diameter Sensitivity

The sensitivity of the model to the diameter of the gelatin body was examined by varying the diameter through the range of values measured during the experiments. To ensure the mass remained the same, the length was adjusted accordingly. Therefore, the comparison made is actually the ratio of length to diameter (L/D). The results are summarized in Table 12 and plotted in Figure 51 to Figure 54.

Table 12 – Sensitivity to L/D

Diameter (mm)	Length (mm)	L/D	Peak Pressure (MPa)	Start of Steady-State (µs)	End of Steady-State (us)	Final Time (us)	Median Steady-State (MPa)	Peak Impulse (Pa*s)	Steady-State Impulse (Pa*s)
95	295.46	3.11	394.5	151	1330	2400	14.22	6400	20750
102.3	258	2.52	398	164	1032	2250	14.67	7051	17968
110	226.98	2.06	395.2	181	908	2250	14.77	7409	14688

There was no definitive trend for the peak pressure over this range. In reality, the peak pressure should increase with increasing diameter (decreasing L/D) as the release waves take longer to reach the center. For this case, the change in peak pressure was negligible and any discrepancies from the expected trend were most likely due to discretization error.

The peak impulse decreases with increasing L/D, which was caused by the peak pressure remaining relatively constant, but the start of the steady-state region was beginning earlier. The earlier steady-state region occurs due to the smaller diameter and thus less distance for the release waves to travel before reaching steady-state. This effect causes the duration of the peak impulse to be shorter, which results in a smaller peak impulse.

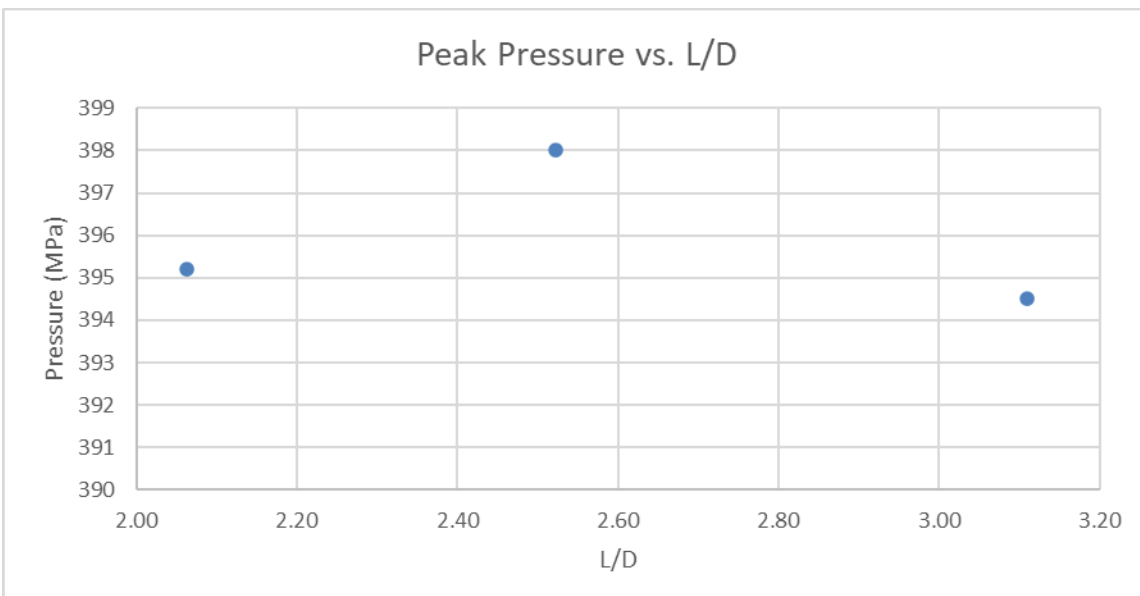

Figure 51 – Relationship of peak pressure to L/D.

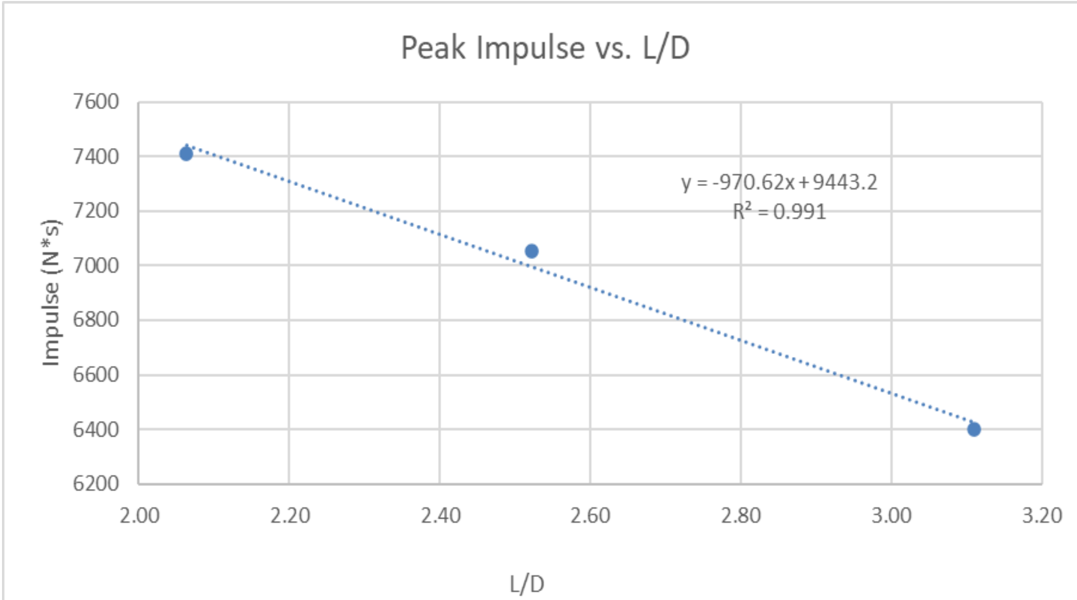

Figure 52 – Relationship of peak impulse to L/D.

The steady-state pressure decreases with increasing L/D, which can be attributed to the larger diameter allowing more pressure to build at the center of impact due to the larger distance the release waves must travel. However, the steady-state impulse increases with increasing L/D. At the larger L/D, even though the diameter is smaller, and the steady-state pressure is lower, the increased length causes the end of the state-state region to be delayed substantially such that the impulse increases.

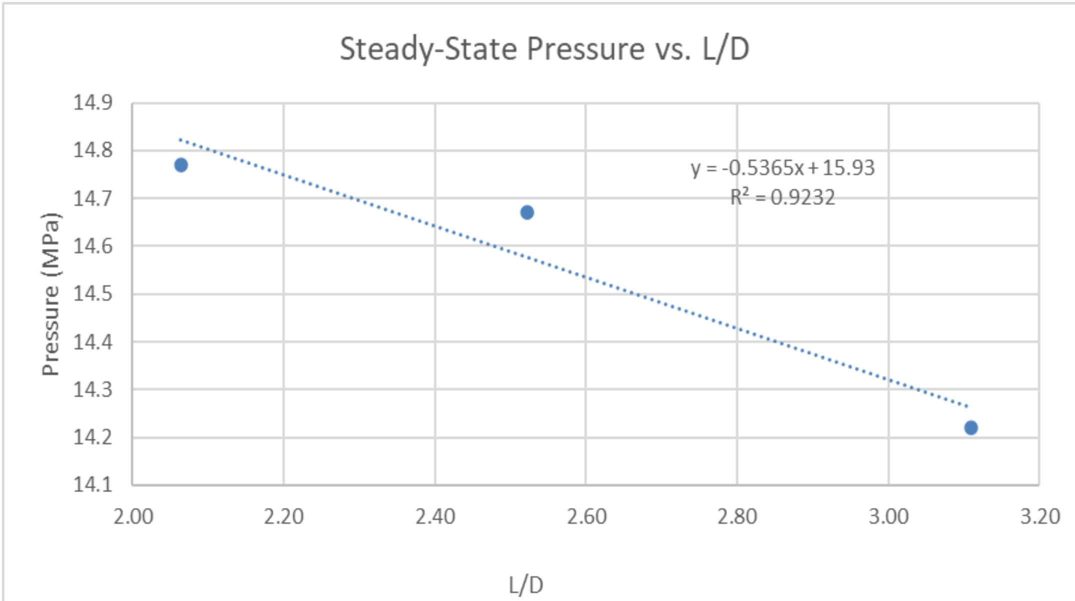

Figure 53 – Relationship of steady-state pressure to L/D.

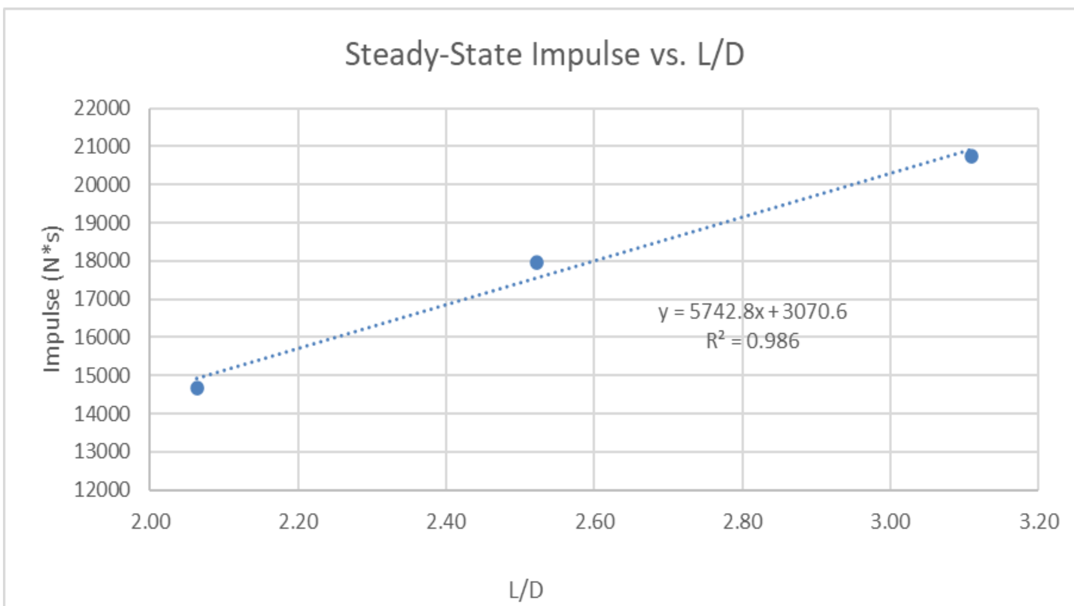

Figure 54 – Relationship of steady-state impulse to L/D.

4.5.5 Radius of Ends Sensitivity

The sensitivity to the radius of the ends was examined by varying the radius through the range of values measured during the experiments. To ensure the mass remained the same, the length was adjusted accordingly. Therefore, the comparison made is actually the ratio of radius to length (R/L). The results are summarized in Table 13 and plotted in Figure 55 to Figure 58.

Table 13 – Sensitivity to R/L

Radius (mm)	Length (mm)	R/L	Peak Pressure (MPa)	Start of Steady-State (µs)	End of Steady-State (us)	Final Time (us)	Median Steady-State (MPa)	Peak Impulse (Pa*s)	Steady-State Impulse (Pa*s)
20	245.71	0.081	391.9	149	969	2500	13.19	6857	15246
39	258	0.151	398	164	1032	2250	14.67	7051	17968
60	272.38	0.220	395.6	170	1010	2350	14.75	6730	18382

There is no clear relationship for either peak pressure or peak impulse versus R/L for this range of radii. The lack of a trend may be attributed to the results being within the expected noise of the discretization error as there is a relatively small change in values over the range. Theoretically speaking, the peak pressure should decrease with increasing radius as the release waves will have a shorter distance to travel.

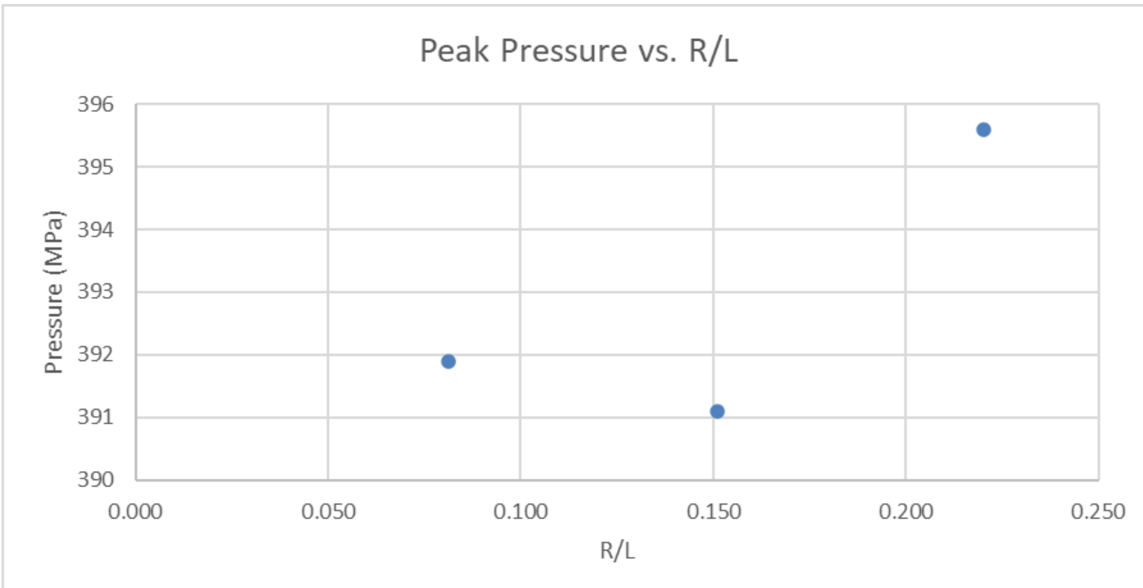

Figure 55 – Relationship of peak pressure to R/L.

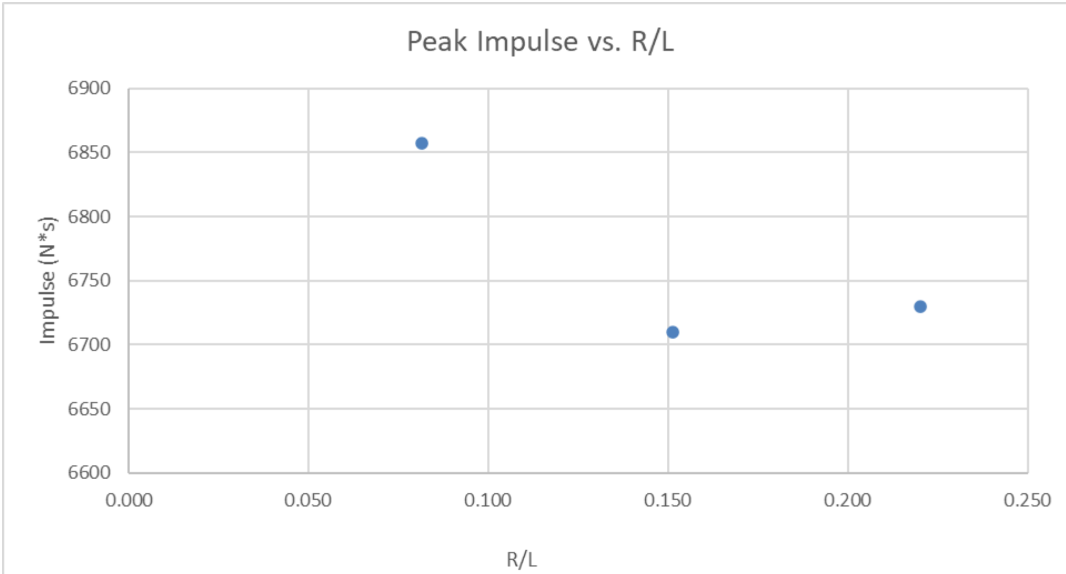

Figure 56 – Relationship of peak impulse to R/L.

The steady-state pressure and impulse appear to increase linearly with increasing R/L over this range. This was surprising since the radius of the ends should have very little effect on the steady-state pressure. The increase in the impulse is expected because the length is increasing with R/L and therefore the steady-state pressure has a longer duration. Closer examination of the case where R/L was 0.081 indicated that there may be some numerical problems with the model. It could be seen that the back of the bird was expanding in the opposite direction of the impact direction quite early in the simulation. To confirm these suspicions, a model was created with a cylindrical bird and from this model it was clear that there was a numerical error which resulted in the lower steady-state pressures. In the cylindrical model, the SPH nodes were rebounding quickly off the rigid plate and causing the bird to release pressure outward throughout the length of its body almost immediately (i.e., the bird was essentially exploding). Correcting this numerical error was left for future work.

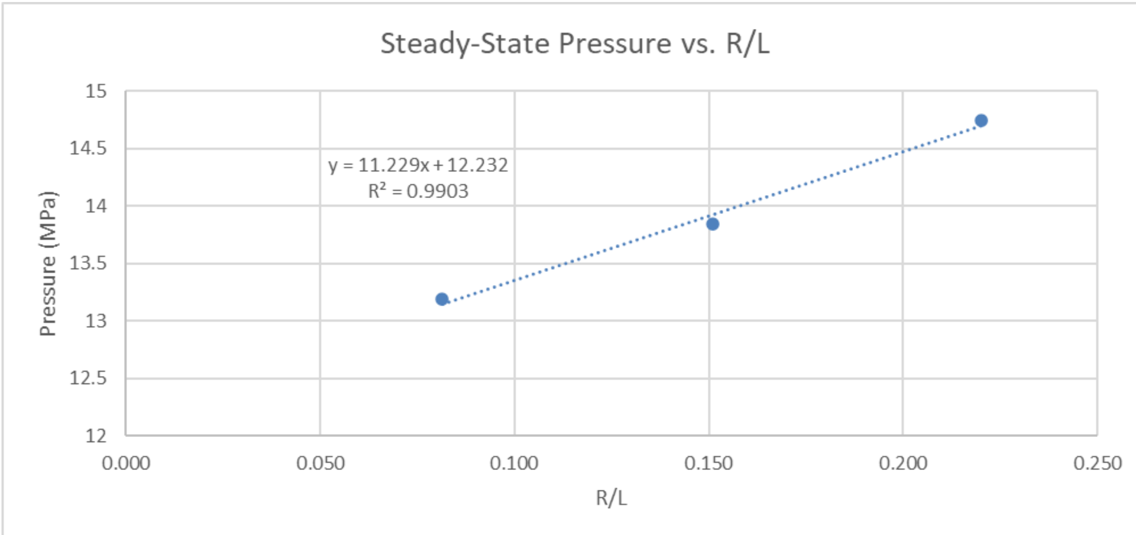

Figure 57 – Relationship of steady-state pressure to R/L.

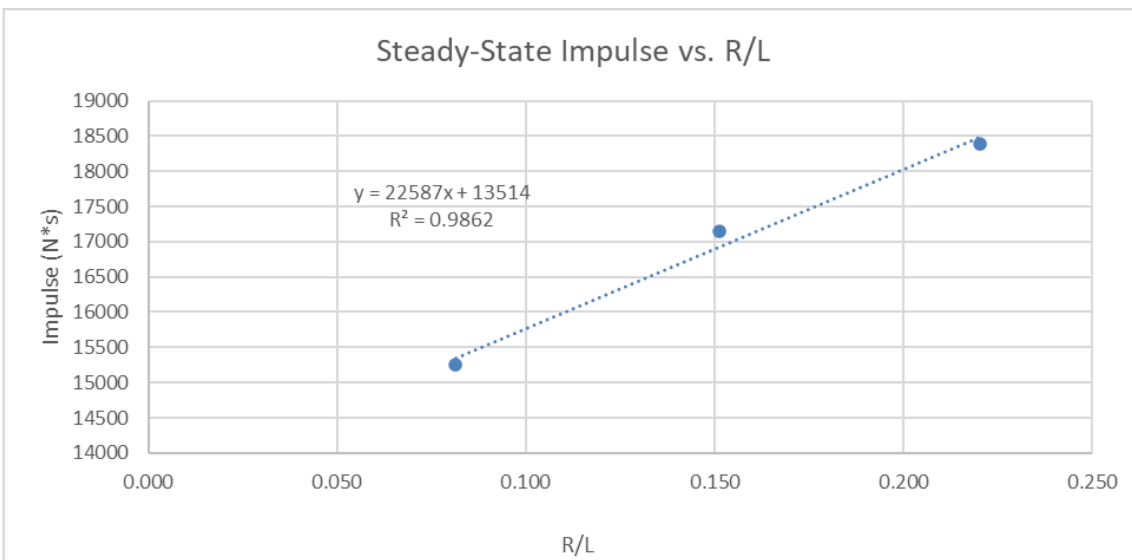

Figure 58 – Relationship of steady-state impulse to R/L.

4.5.6 Density Sensitivity

Since the gelatin bird was elastically strained due to the launch loads, it is possible that the density changes prior to impact. For this reason, it was decided to examine the sensitivity to density as well. For an initial study, the density was varied from 750 to 1250 kg/m^3. It should be noted that the mass of the bird was changing due to these density changes and therefore changing the mass alone would not be realistic. These results are just to see the effects of changing the density. The results are summarized in Table 14 and Figure 59 to Figure 62 and show that all of the pressures and impulses increase nearly linearly with increasing density. This makes sense as the Mie-Gruneisen pressure calculation (see equation 27) includes the density term in the numerator.

Table 14 – Sensitivity to Density

Density (kg/m^3)	Mass (kg)	Peak Pressure (MPa)	Start of Steady-State (µs)	End of Steady-State (us)	Final Time (us)	Median Steady-State (MPa)	Peak Impulse (Pa*s)	Steady-State Impulse (Pa*s)
750	1.432	314.2	168	1070	2400	10.89	5709	13442
950	1.814	397.9	164	1032	2500	14.67	7051	17980
1250	2.387	523.6	170	1030	2430	19.58	9726	23219

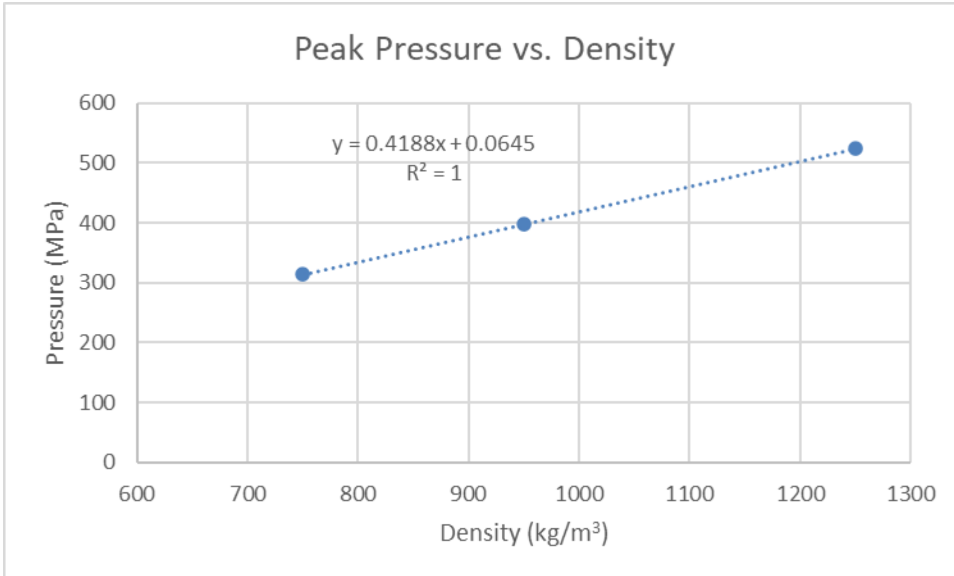

Figure 59 – Relationship of peak pressure to density.

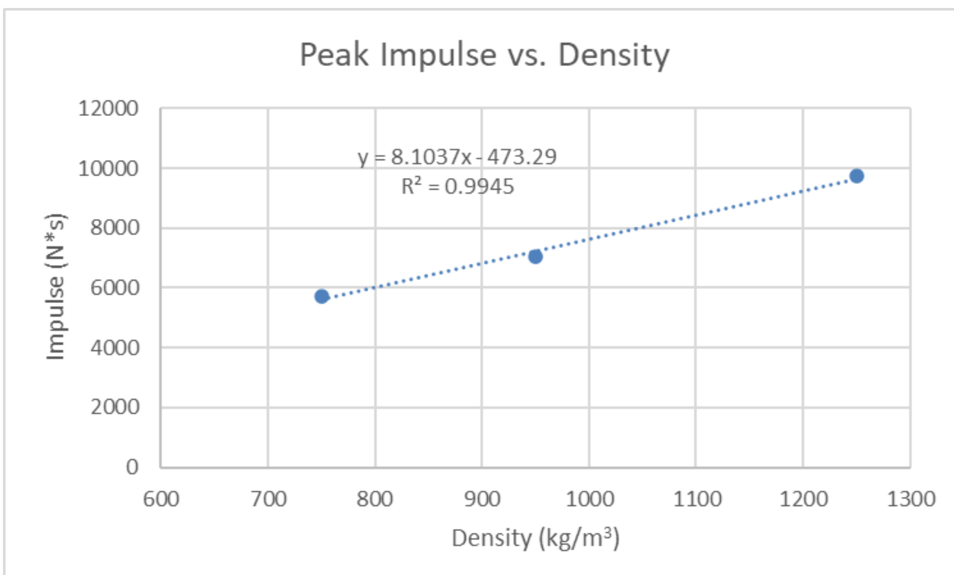

Figure 60 – Relationship of peak impulse to density.

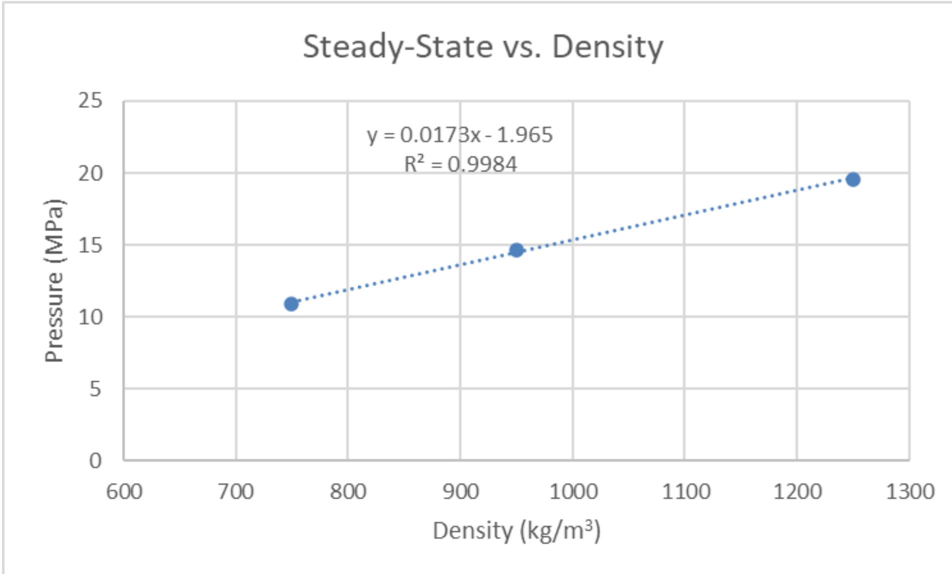

Figure 61 – Relationship of steady-state pressure to density.

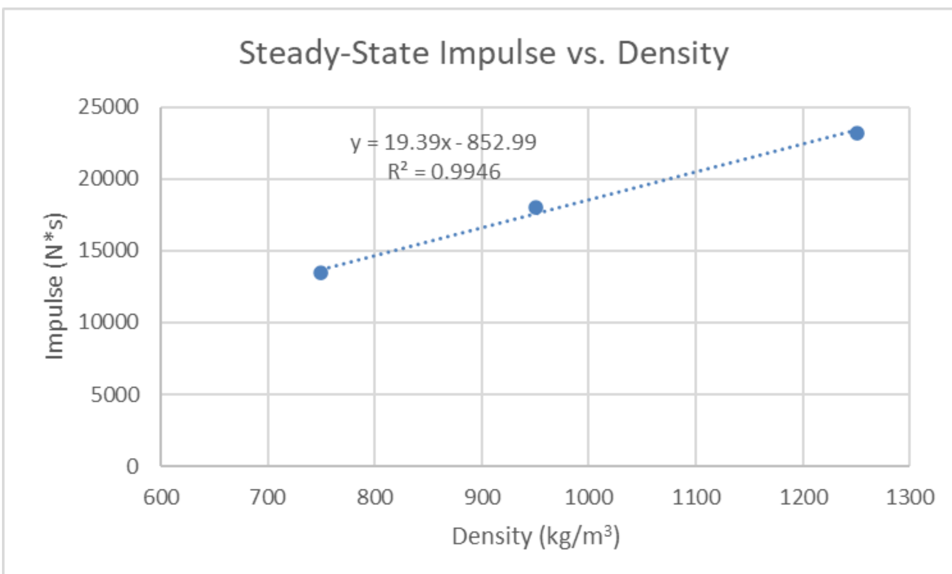

Figure 62 – Relationship of steady-state impulse to density.

4.5.7 Variable Density Sensitivity

As mentioned in the previous section, changing the density resulted in an unrealistic mass change. This can be countered by changing the geometry of the bird, but another possibility is to have a variable density throughout the bird. From the high-speed videos of the rigid plate tests, it could be seen that the bird is stretching and compressing while in flight before hitting the target. Therefore, the possibility of a variation in density throughout the bird is probable. A C++ program was written that creates an LS-Dyna K-file of a bird with variable density. The program allows the user to enter the desired geometry and mass of the bird, the SPH size, and the desired density at the front and rear of the bird. The program then creates all of the SPH nodes along with nodal densities such that there is a smooth gradient of density from the front of the bird to the rear of the bird, while maintaining the correct total mass.

A parametric study was performed using variable density birds with a defined front and rear densities and had a linear gradient of density from front to rear. The results are summarized in Table 15. As per Figure 63 and Figure 62, the peak pressure and peak impulse increased as the front density increased. Figure 65 and Figure 66 show that the steady-state pressure and impulses both decreased with increasing front density. This is consistent with the explanation above in that the Mie Gruneisen pressure calculation is dependent on the density in the numerator. With a higher density towards the front, the early stages (i.e., the peak stages) would result in higher pressures, while the later stages with lower densities would result in lower pressures.

Table 15 – Sensitivity to Variable Density

Front Density (kg/m^3)	Rear Density (kg/m^3)	Peak Pressure (MPa)	Start of Steady-State (µs)	End of Steady-State (us)	Final Time (us)	Median Steady-State (MPa)	Peak Impulse (Pa*s)	Steady-State Impulse (Pa*s)
1300	600	565.9	168	1020	2240	13.93	9013	16284
950	950	397.9	164	1032	2500	14.67	7051	17980
600	1300	136.4	119	1140	2350	14.76	4559	18772

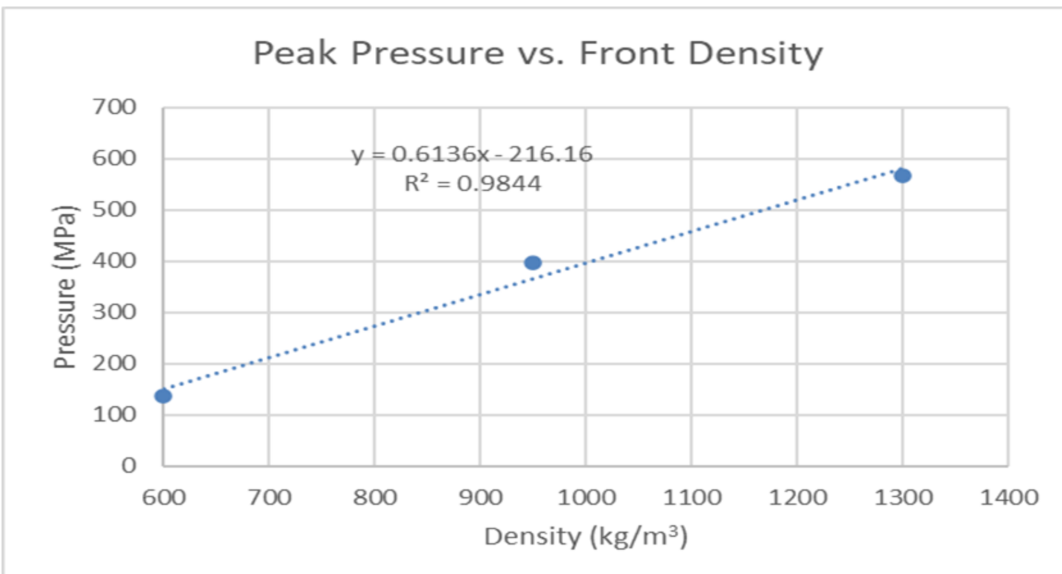

Figure 63 – Relationship of peak pressure to front density.

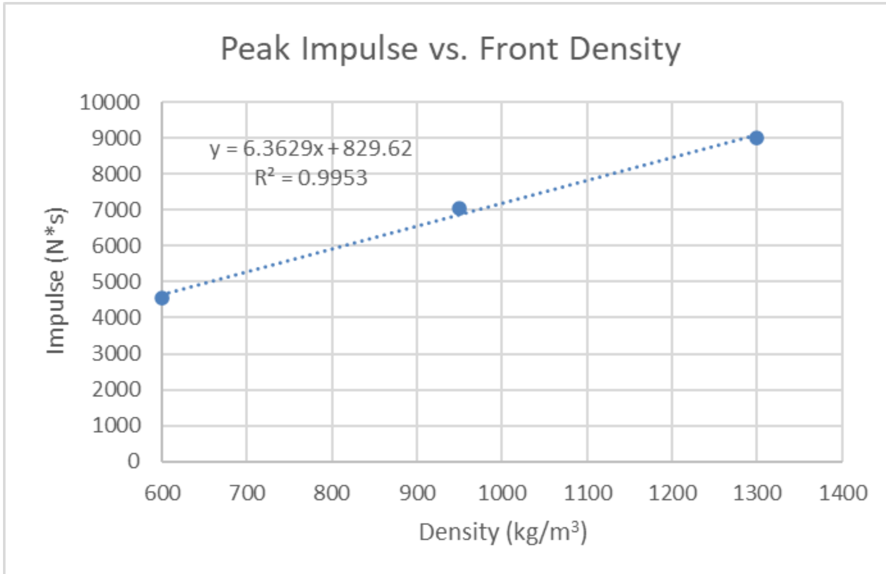

Figure 64 – Relationship of peak impulse to front density.

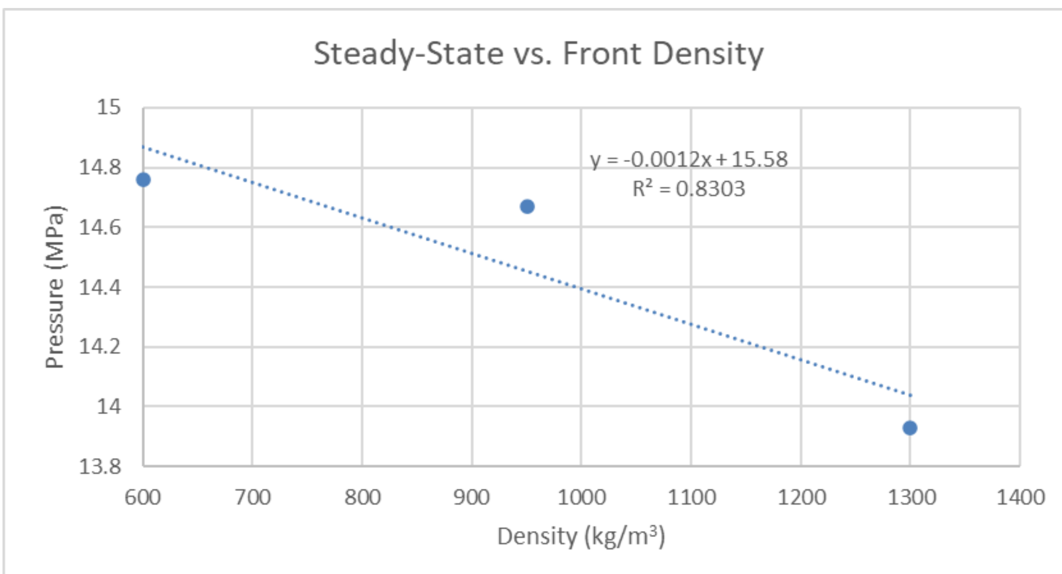

Figure 65 – Relationship of steady-state pressure to front density.

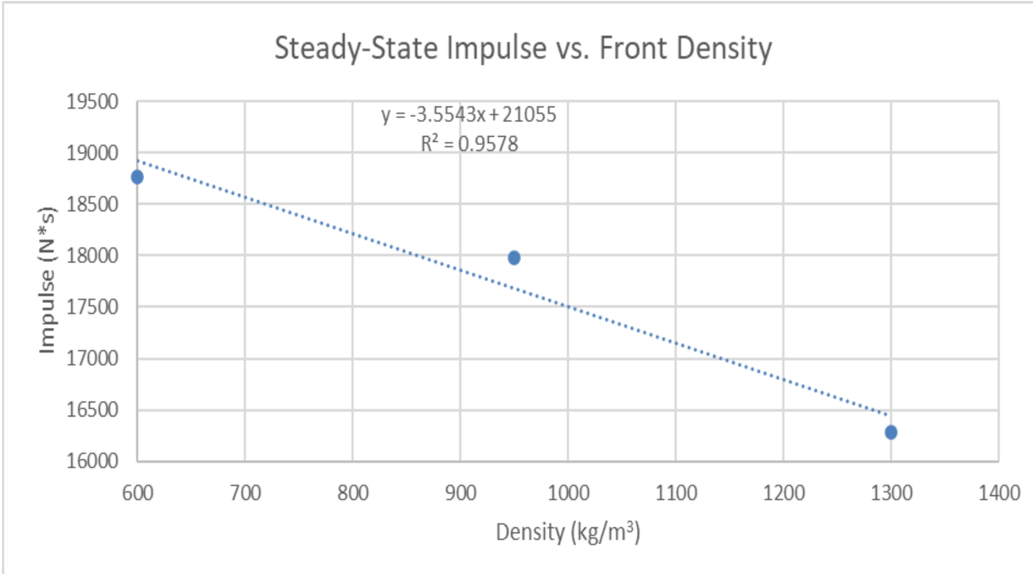

Figure 66 – Relationship of steady-state impulse to front density.

4.5.8 Radial Offset Sensitivity

Simulation accuracy is directly tied to having an accurate gelatin bird model. The accuracy of this model is largely dependent on the accuracy of the experimental data from which it is based. As discussed in Chapter 3, a key potential source of experimental error was related to the distance from the center of the gelatin bird to the center of the pressure sensor at the point of impact. The experimental work originally only used one pressure sensor but found this to be inadequate and three more sensors were added. This was also one of the reasons why the data from previous research, which was also based on using a single pressure sensor, was not adequate.

The sensitivity to radial offset from the center of impact was studied by including 16 equally spaced simulated sensors. The peak pressure and steady-state pressure were then calculated for each offset location. Figure 67 shows the rapid decrease in peak pressure with radial offset. This rapid decrease helps explain the difficulty in capturing the peak pressure consistently in the experiments. The slight rise in pressure at approximately 14mm offset corresponds to the point at which curvature starts in the model. Prior to this point, due to the discretization, there is not yet any curvature and the impact essentially occurred on a flat face. A possible explanation for this slight rise is that the point of curvature creates a new initiation point of impact with combines with the pressure wave from the previous points to create a momentary rise in pressure. For confirmation of this effect, the point of curvature was moved and the rise in pressure shifted along with the curvature.

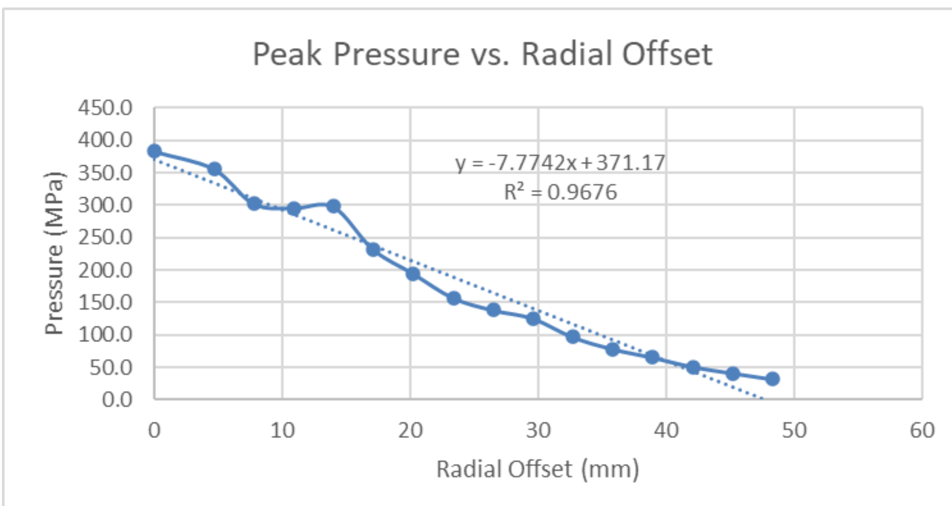

Figure 67 – Relationship of peak pressure to radial offset.

Figure 68 shows a more gradual decrease of steady-state pressure with radial offset. Close examination of the plot shows that pressure at zero offset is marginally lower than the pressure at approximately 5mm offset. This is most likely an artifact of the discretization as the SPH nodes must be offset from the symmetry axis. This offset combined with the smoothing length may result in more nodes impacting the second sensor (and therefore more mass) than the first sensor and thus a slightly higher pressure.

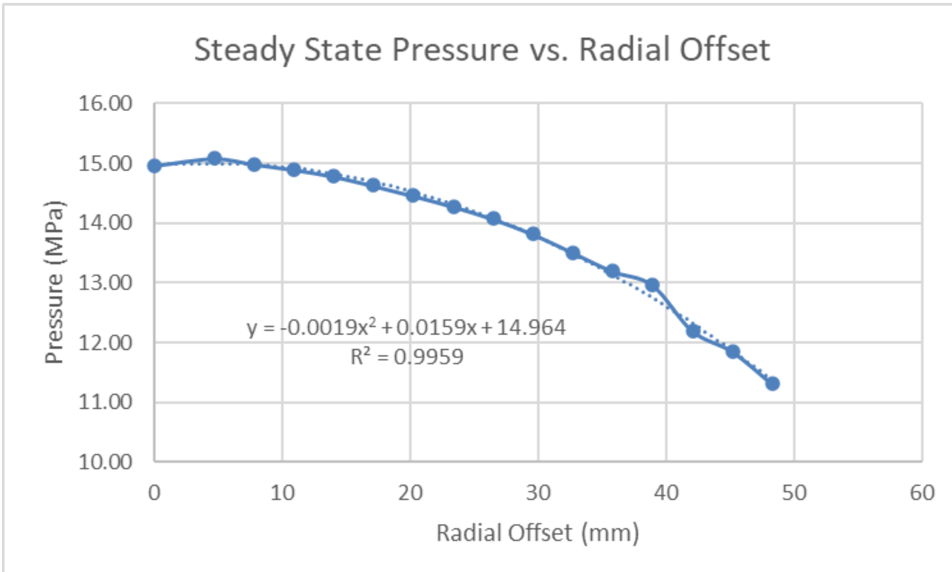

Figure 68 – Relationship of steady-state pressure to radial offset.

4.6 Steady-State Pressure Control for Fixed Peak Pressure

It was attempted to control the steady-state pressure for a given peak pressure by varying only the Gruneisen C and S values. The C and S parameters were adjusted such that each combination resulted in a peak pressure of 376.5 MPa. The results in Table 16 and plotted in Figure 69 show that there was no clear trend in controlling the steady-state pressure while maintaining a desired peak pressure using only the Gruneisen parameters C and S.

Table 16 – Constant Peak Pressure with Variable Gruneisen C and S

C (m/s)	S	Median Steady-State Pressure (MPa)
1000	3.07	14.47
1200	2.47	14.26
1400	1.75	14.73
1450	1.56	14.06
1500	1.31	14.75
1791	0.00001	15.19

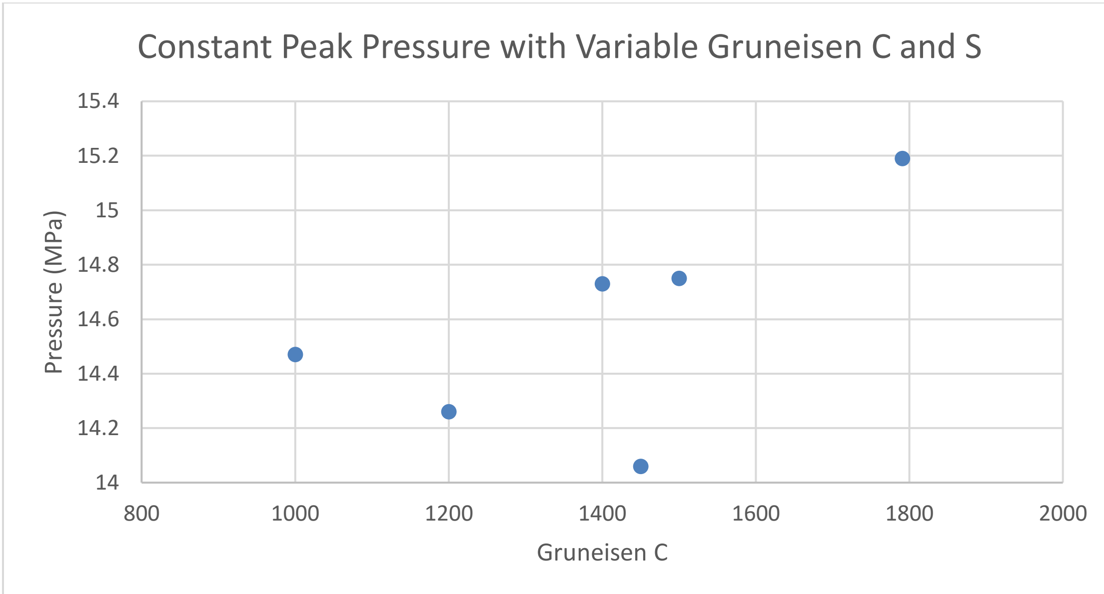

Figure 69 – Relationship of steady-state pressure to Gruneisen C for a constant peak pressure with variable Gruneisen C and S.

A second attempt at controlling the steady-state pressure for a given peak pressure was made by holding the Gruneisen C constant and varying the Gruneisen S and dynamic viscosity, μ, values. The parameters S and μ were adjusted such that each combination resulted in a peak pressure of 376.5 MPa. The results in Table 17 and plotted in Figure 70 show that the steady-state pressure can be controlled with nearly a linear relationship while maintaining a desired peak pressure for a given Gruneisen parameter C, by varying only the Gruneisen S and dynamic viscosity μ.

Table 17 – Constant Peak Pressure and Gruneisen C with Variable Grunseisen S and Dynamic Viscosity μ

S	**μ (Pa*s)**	**Median Steady-State Pressure (MPa)**
5.5	700	18.45
5.02	580	17.59
4.13	400	16.46
2.96	200	15.02
1.56	0	14.06

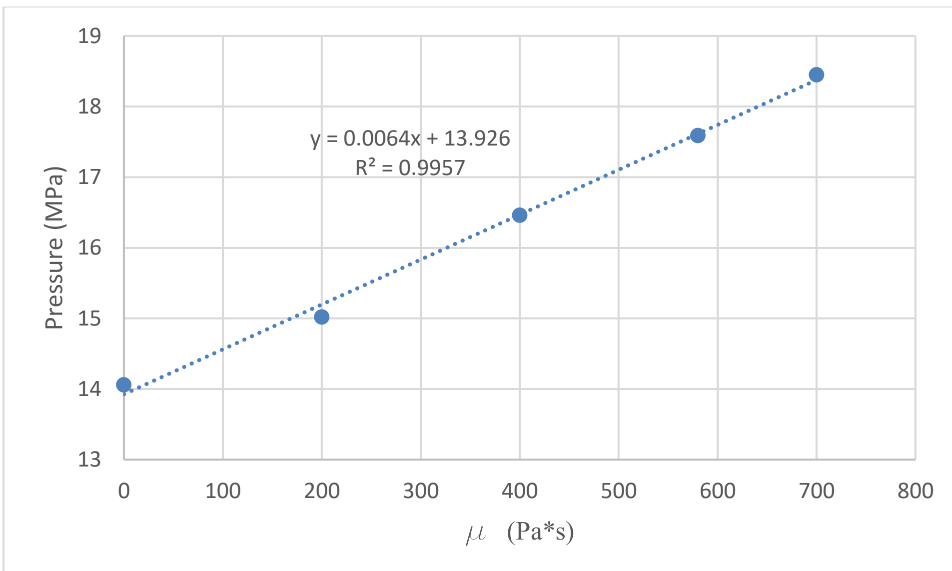

Figure 70 – Relationship of steady-state pressure to dynamic viscosity for a constant peak pressure and Gruneisen C with variable Gruneisen S and dynamic viscosity μ.

4.7 Significance of Dynamic Viscosity and Shear Thickening

It was shown in section 4.6 that incorporating the dynamic viscosity into the material model enables for independent control of the peak pressure and steady-state pressure when combined with the Gruneisen parameters. Before using the dynamic viscosity for a bird model, it is first necessary to determine if the dynamic viscosity could play an important role in reality.

As mentioned in the literature review, during a bird strike event, it is typically assumed that the stresses generated due to the deceleration of the bird greatly exceed its yield strength and the bird can be treated as a fluid where the material density dominates the event instead of the strength. For this reason, a material model for the bird usually only consists of an initial density and an equation of state [5]. However, ballistic gelatin is known to act as a shear-thickening non-Newtonian fluid at high strain rates as per [54] and [55], which may invalidate the assumption that the strength is negligible.

Kwon and Subhash showed that the compressive strength of ballistic gelatin increased from 6 kPa at quasi-static rates to 6 MPa at strain rates of approximately 3200 /s primarily due to the increase in viscosity [55].

Subhash et al [54] performed studies on the non-Newtonian behavior of ballistic gelatin at high shear rates. They experimentally determined the maximum shear stress for given strain rates and then calculated the dynamic viscosity assuming a power law model for capturing the shear thickening behavior. Their results are shown in Figure 71.

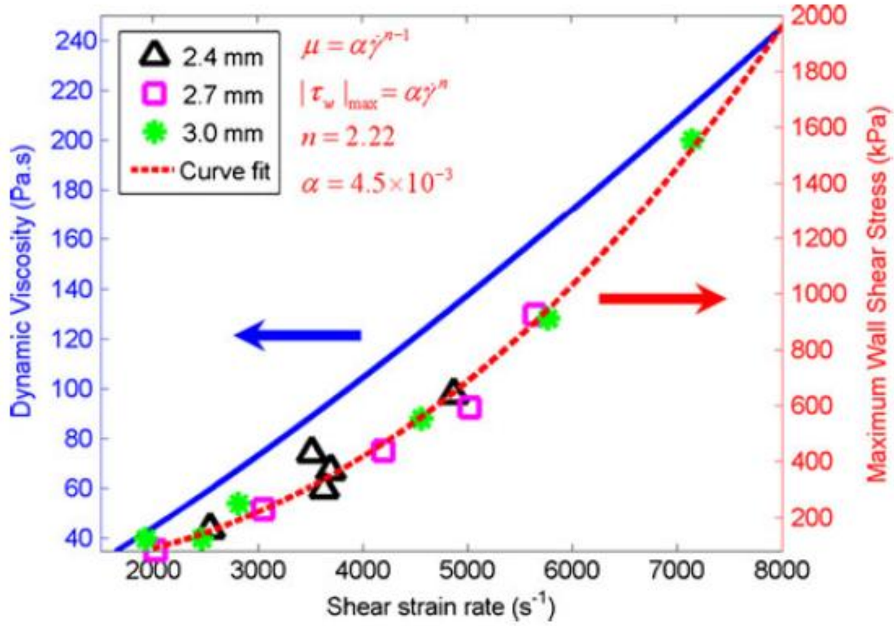

Figure 71 – Dynamic viscosity versus shear strain rate for ballistic gelatin as per Subhash et al [54].

The strain rates from the rigid plate simulations were on the order of 10^4 and 10^5 /s. In accordance with the power law model proposed by Subhash et al in [54], this means the viscosities could be from hundreds of Pa*s to tens of thousands of Pa*s (assuming the extrapolation to these higher strain rates continues to follow this trend). The highest strain rates occur during the initial impact and therefore it is likely that there would be a short duration increase in dynamic viscosity on the order of 10^4 Pa*s followed by a dynamic viscosity on the order of 10^2 Pa*s during the steady-state phase.

This demonstrates that the strength portion of the material model is likely very important at these high strain rates due to the dramatic increase in dynamic viscosity due to the shear thickening behavior of the gelatin bird.

4.8 Gelatin Bird Material Model

For the initial attempt at creating a bird model capable of matching the pressure profiles from the rigid plate experiments, it was decided to use the Gruneisen EOS and dynamic viscosity only to tune the model.

Hundreds of simulations were performed in an attempt to tune the pressure profile to match the experimental data. The most relevant simulation results are summarized in Appendix H. Using the method described in section 4.6, it was possible to precisely match the target peak pressure every time provided the viscosity was not too high. All the timings (start of steady-state, end of steady-state, and final time) fell within the range of values expected as per the experiments. A summary of the errors can be seen in Table 18. In the table, errors less than 10% are highlighted green, within 20% are highlighted yellow, and more than 20% are highlighted red.

Table 18 – Summary of Select Bird Model Errors

Gruneisen C (m/s)	Dynamic Viscosity (Pa*s)	Gruneisen S	Peak Pressure Error	Steady-State Pressure Error	Peak Impulse Error	Steady-State Impulse Error	Total Impulse Error
500	600	0	-38.1%	-3.7%	-0.9%	-11.4%	-7.8%
	600	1	-40.8%	-3.1%	-7.5%	-5.3%	-6.0%
	600	5	-42.2%	3.9%	-19.5%	1.4%	-5.7%
	600	10	-0.5%	8.5%	-21.1%	-1.7%	-8.3%
	1000	1	-1.6%	17.0%	0.6%	4.0%	2.8%
	1500	2	-1.1%	16.7%	0.8%	13.5%	9.2%
	2000	1	79.4%	32.9%	25.4%	8.8%	14.5%
700	400	8	4.2%	-5.0%	-33.5%	-0.1%	-11.4%
	1000	1	-6.8%	20.0%	-14.2%	9.7%	1.6%
1000	0	3.07	0.0%	-15.2%	-42.6%	-12.7%	-22.8%
	200	4.92	0.0%	-13.1%	-37.1%	-8.4%	-18.1%
	400	6.55	-0.1%	-3.2%	-35.6%	0.3%	-11.9%
	500	7.3	0.0%	-0.5%	-34.0%	4.7%	-8.4%
	930	0	-2.7%	18.7%	-23.2%	12.6%	0.4%
	1000	1	11.0%	23.7%	-21.7%	14.3%	2.1%
	1000	7.3	0.6%	27.8%	-23.4%	13.2%	0.8%
1200	0	2	-6.6%	-13.5%	-42.9%	-9.7%	-20.9%
	0	2.47	0.1%	-16.5%	-27.9%	-19.8%	-22.5%
	1000	1	14.6%	17.0%	-20.3%	14.9%	3.0%
1400	0	1.75	0.1%	-13.7%	-29.7%	-16.3%	-20.9%
1450	0	1	-7.0%	-17.8%	-30.8%	-17.4%	-21.9%
	0	1.56	0.1%	-17.6%	-29.8%	-16.6%	-21.1%
	0	2	5.7%	-14.1%	-33.7%	-13.2%	-20.2%
	0	2.5	12.4%	-11.9%	-35.7%	-14.1%	-21.4%
	0	4	33.9%	-15.7%	-33.4%	-17.4%	-22.8%
	50	2	0.8%	-17.8%	-27.4%	-17.8%	-21.1%
	100	2	-3.4%	-15.5%	-36.0%	-12.4%	-20.4%
	200	2	-9.9%	-11.6%	-31.4%	-10.7%	-17.7%
	200	2.96	0.0%	-12.0%	-32.5%	-10.3%	-17.8%
	400	4.13	-0.1%	-3.6%	-31.8%	-1.3%	-11.7%
	540	4.85	0.1%	4.3%	-27.9%	2.2%	-8.0%
	560	4.95	0.1%	-0.8%	-26.1%	2.1%	-7.5%
	580	5.02	0.0%	3.0%	-27.2%	2.6%	-7.5%
	700	5.5	0.0%	8.1%	-24.7%	6.5%	-4.0%

	850	0	0.4%	12.2%	-18.7%	8.0%	-1.0%
	1000	1	6.5%	24.0%	-16.1%	10.6%	1.5%
1482.9	0	2	8.0%	-16.8%	-35.8%	-16.5%	-23.0%
1500	0	1.31	0.1%	-13.6%	-33.4%	-15.3%	-21.4%
1600	0	2	14.3%	-16.3%	-37.6%	-14.0%	-22.0%
1791	0	0.00001	0.0%	-11.0%	-35.7%	-9.9%	-18.7%
2000	700	0	0.8%	7.0%	-30.1%	9.0%	-4.3%

The peak impulse could only be matched using this approach when the Gruneisen C was 500 m/s. It should be noted that this may not be a realistic value as the Gruneisen C is typically tied to the speed of sound in the material, while the microballoons would have a relatively low speed of sound similar to air (approx. 331 m/s at 0°C [56]), the ballistic gelatin has a speed of sound typically above 1500 m/s [57] and therefore it would be expected that the speed of sound would be closer to that magnitude in reality. For the purpose of studying the ability to control the pressure profile with the result of the parametric data, it was decided to allow this potentially low value of Gruneisen C to be used at this stage. The best match overall was with Gruneisen C = 500, S = 1, and dynamic viscosity of 1000 Pa*s. In this model the steady-state pressure was over-predicted by 17%, but all other target values were achieved within 4%. The simulation results for this case at key time instances is shown in Figure 72 and the corresponding pressure profile is shown in Figure 73. Another good match was with Gruneisen C = 500, S = 1, and dynamic viscosity of 600 Pa*s. This model under-predicted the peak pressure significantly (-40.8%) but matched all other target values within 7.5%.

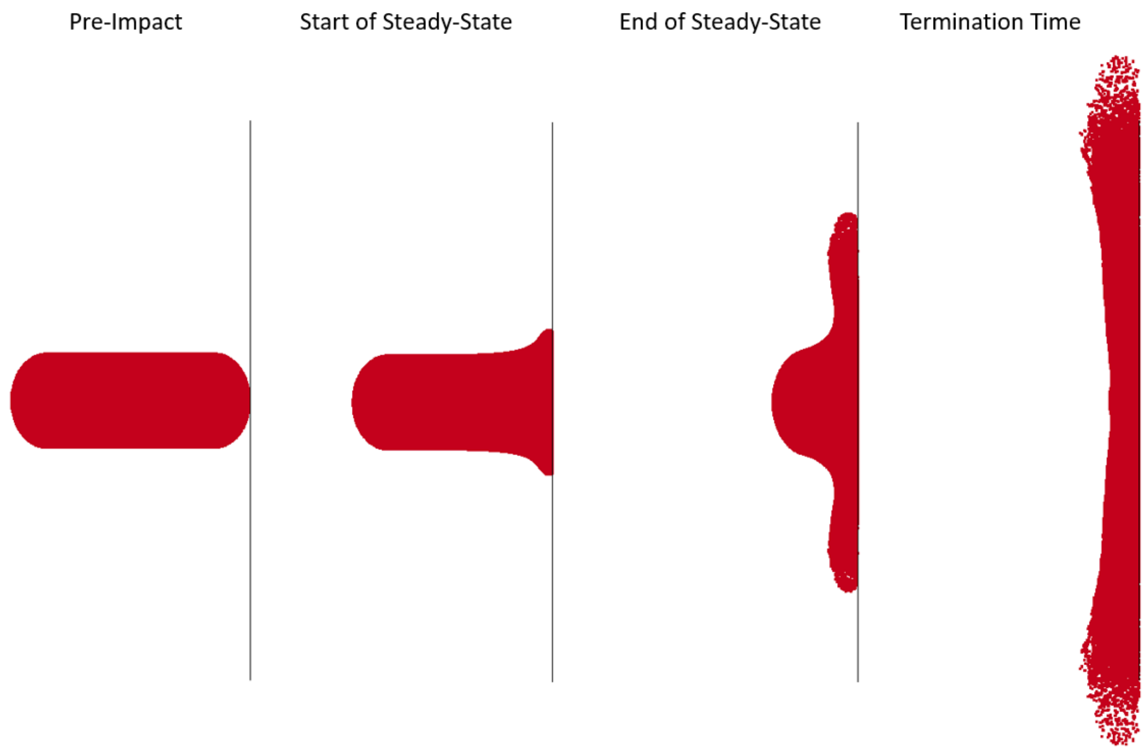

*Figure 72 – Simulation results at key time instances for Gruneisen C = 500 m/s, S = 1, and dynamic viscosity of 1000 Pa*s.*

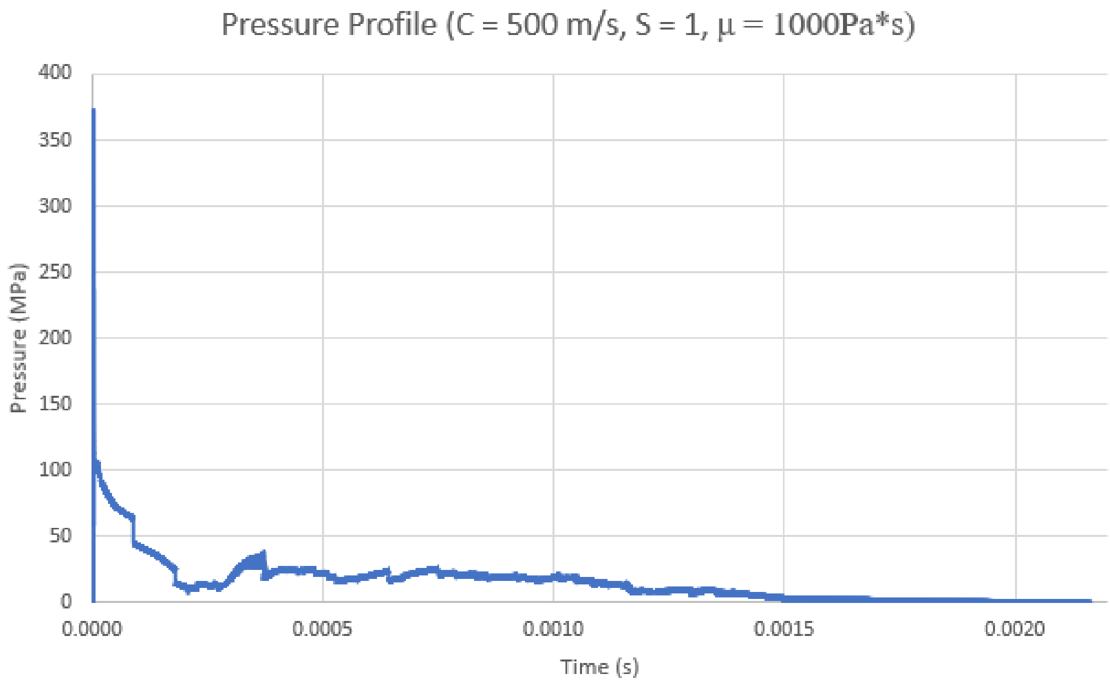

*Figure 73 – Pressure Profile for simulation with Gruneisen C = 500 m/s, S = 1, and dynamic viscosity of 1000 Pa*s.*

The other methods to increase the peak impulse are to increase the diameter and/or the density of the bird. When the diameter is increased to the maximum value that occurred (123mm) and the length is reduced to the smallest that occurred (220 mm), the mass is still too high. Therefore, beyond changing the geometry in a complex manor, the density must be lowered to ensure the proper mass is maintained. Based on an analysis of the trends from the parametric studies, the density has a bigger effect than the diameter and therefore reducing the diameter to its smallest allowable and increasing the density as much as possible will increase the peak impulse the greatest.

A simulation was run with an increased density, which had a diameter of 99 mm, a radius of 59 mm, and a density of 1304.6 kg/m^3. The Gruneisen C and S were set to 500 and 2 respectively. The dynamic viscosity was set to 1000 Pa*s. With these settings the simulation was able to successfully match both the peak pressure and impulse with an over-prediction of the steady-state pressure and impulse. The results are summarized in Table 19.

Table 19 – Simulation results for density of 1304.6 kg/m^3

Peak Pressure Error	Steady-State Pressure Error	Peak Impulse Error	Steady-State Impulse Error	Total Impulse Error
1.3%	19.6%	-1.6%	23.6%	15.0%

At this point, while the results are not perfect, there is a significant improvement as compared to the results of the existing bird models from precious research as presented in section 4.4. The results demonstrate the complexity/difficulty of the problem. Further improvements of the material model will possibly involve the implementation of a custom material model which is outside of the scope of work of this thesis. For this reason, it was decided to move on to the validation simulations to investigate whether any of the models created thus far could match the validation experiments.

5 Bird Model Validation

For validation of the model, a set of flexible plate tests were performed. During these tests, the gelatin bird was fired into a flexible plate of known material properties and a simulation of the same test was used to compare the resulting deflections in the plate as a means of validating the gelatin bird model.

5.1 Flexible Plate Experimental Set Up

For the flexible plate experiment a 6061-T6 aluminum plate was used because aluminum is commonly used in aerospace applications and 6061-T6 is well characterized and relatively inexpensive. The plate was square with outer dimensions of 610mm (2 ft) and a nominal thickness of 9.525mm (3/8”). The actual thickness of each plate was measured, and they were all closer to 9.9mm thick. The 9.9mm thickness was used in all simulations.

The aluminum plate was mounted to the facility’s Sabot Stopper as this structure was very rigid and had a 508mm (20”) hole in it already. The 6.35mm (1/4”) thick steel plate on the front of the Sabot Stopper was modified to add a 6.35mm radius around the 508mm hole to avoid any stress concentrations that may occur due to the aluminum plate bending against a sharp edge. The unsupported diameter of aluminum plate when considering the added radius is 520.7mm. An additional 25.4mm (1”) thick steel plate with a matching 508mm hole was used on the upstream side of the aluminum plate to clamp it in place. Twelve 3/4”-10 UNC Grade 5 bolts with a bolt circle diameter of 552mm (21.75”) were used to clamp the aluminum plate assembly to the Sabot Stopper.

Cameras were mounted behind the Sabot Stopper for deflection measurements using Digital Image Correlation (DIC). The experimental set up is shown in Figure 74 with a rear view of the aluminum plate mounted to the Sabot Stopper shown in Figure 75. It should be noted that the aluminum plate was painted with a random speckle pattern for the DIC measurements as discussed in section 5.1.1.

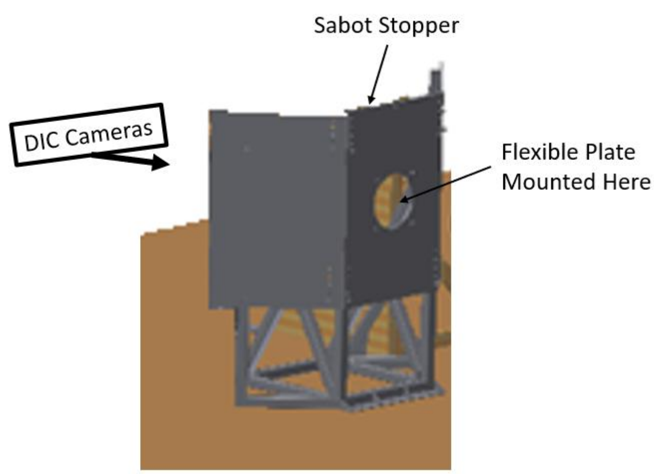

Figure 74 –Flexible plate experiment set up.

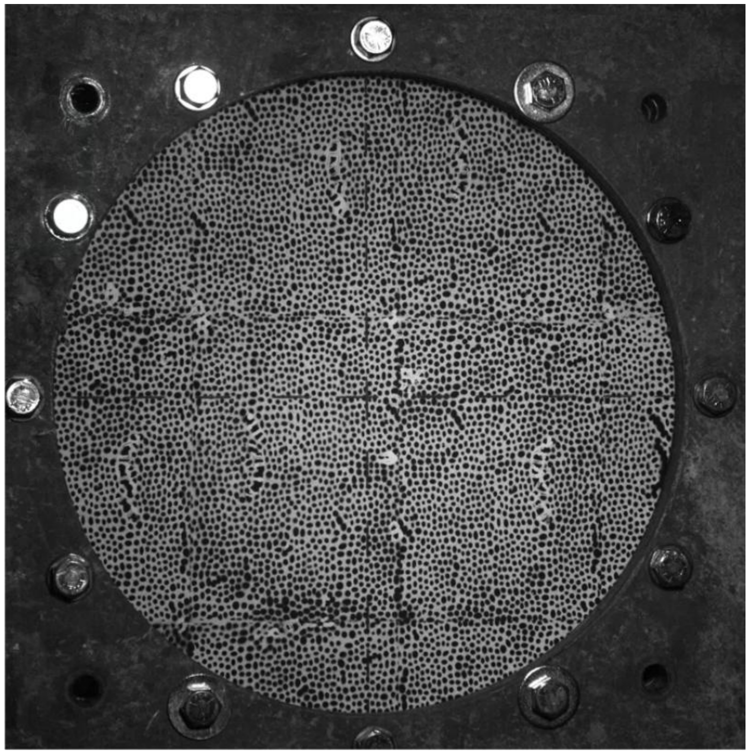

Figure 75 – rear view of flexible plate experiment.

5.1.1 Digital Image Correlation

Digital Image Correlation (DIC) was developed in the 1980s to measure full field displacement and strain profile histories [58]. A typical 3D DIC setup uses two cameras mounted on angles to one another on a rigid bar. The cameras are calibrated prior to the experiment. The calibration process defines the camera internal parameters (intrinsics) as well as the relative position of them to one another (extrinsics). At the beginning of an experiment, an image from one camera is divided into subsets (or facets). The DIC algorithms are used to find the corresponding location of the subset in the second camera with subpixel accuracy. The 3D coordinates can then be calculated by using the known pixel locations in each image combined with the camera calibration parameters. This process continues as deformation occurs over time and the deformation and strains can be calculated over the entire image [59].

For this work, the aluminum plate of interest was painted with a thin coat of white primer. A semi-irregular pattern of black dots was then painted over the white background. Two high speed cameras were pointed at the plate with an approximate angle of 25 degrees between them. The digital image correlation software (ARAMIS) was then used to track the movement of the plate surface. Having two cameras, which are synchronized and calibrated prior to testing, allows the software to triangulate the out-of-plane displacements as well for a full 3D deformation history.

Given the allowable standoff distance of the two high speed cameras from the target plate, the maximum resolution of 1024 x 1024 was required to capture the full field of view. The field of view required an additional amount beyond the aluminum plate to enable the view of the rigid mounting structure as well. This is necessary to allow the software to remove any rigid body motion that may have occurred during the test. This was not done for the first four tests but was done for the final three tests. For this reason, the rigid structure also had a painted dot pattern applied in the last three tests.

The resolution requirement limited the cameras to a framing rate of 12,500 frames per second. This is a contributing source of error for the peak displacement measurement as it is possible the true peak happens between frames. To minimize this error, the time history of three frames before and three frames after the peak value were used with a polynomial fit to interpolate the peak value.

5.2 Flexible Plate Test Results

A total of seven tests were performed and the results are summarized in Table 20. Rigid body motion was removed based on the movement of the Stopper Plate as measured in the final three tests. The average of these three measurements was used to correct for the rigid body movements of the first four tests. The average deflection of 45.29 mm was used as the target value for simulation comparisons.

Table 20 – Flexible Plate Test Results

Test #	Uncorrected Peak Deflection (mm)	Rigid Body Correction (mm)	Corrected Peak Deflection (mm)
1	47.80	1.13*	46.67
2	47.44	1.13*	46.31
3	47.27	1.13*	46.14
4	45.60	1.13*	44.47
5	47.50	1.04	46.46
6	44.30	1.25	43.05
7	45.05	1.09	43.96
Average	**46.42**	**1.13**	**45.29**
Max	**47.80**	**1.25**	**46.67**
Min	**44.30**	**1.04**	**43.05**
Stdev	**1.41**	**0.11**	**1.44**

*These rigid body corrections were not measured and instead just taken as the average of the three that were measured.

A sample DIC measurement is shown in Figure 76.

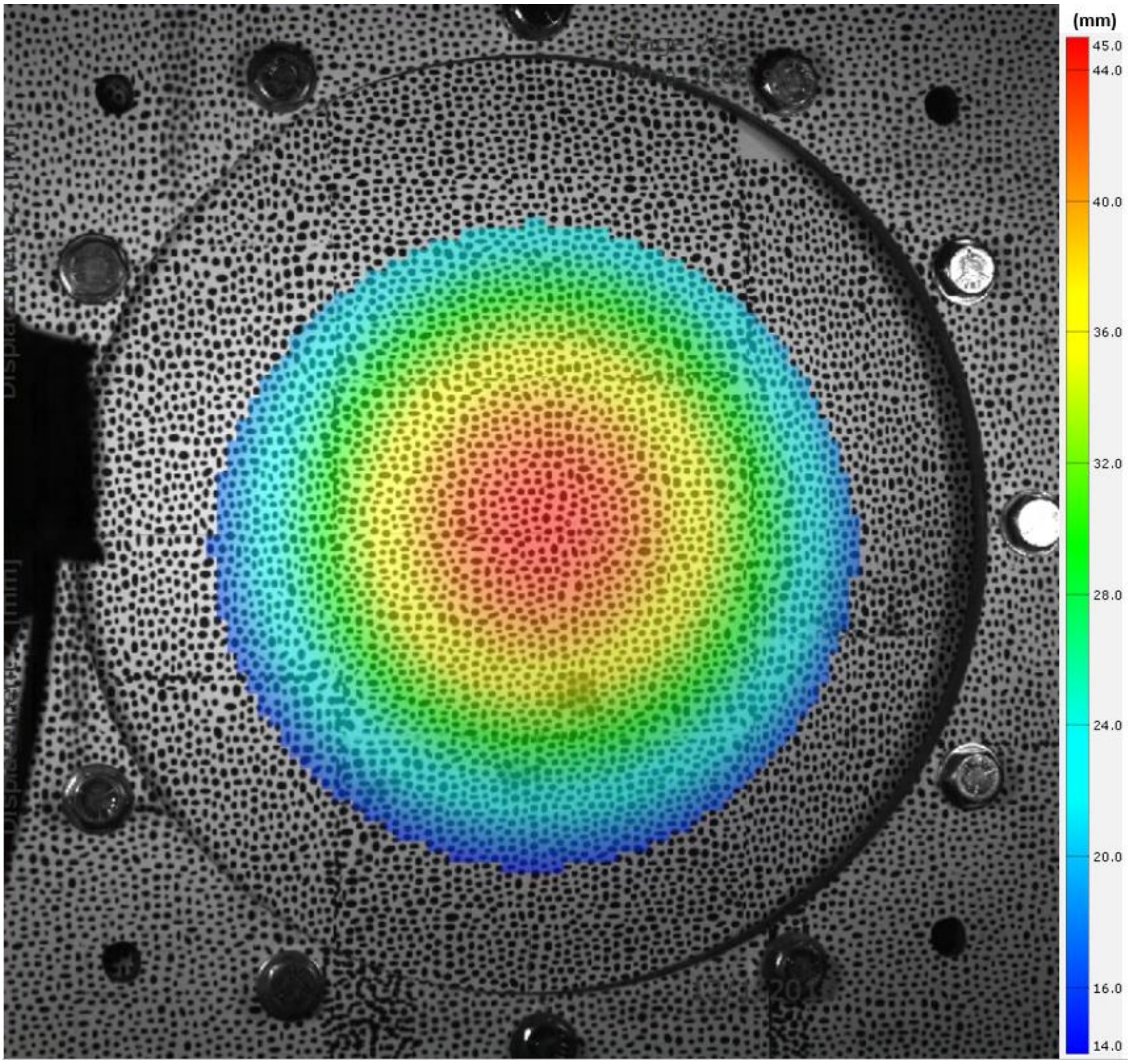

Figure 76 – Sample DIC results showing maximum out of plane deflection.

5.3 Flexible Plate Simulations

A 2D axisymmetric simulation was used for the flexible plate simulations. The plate was given a radius of 260.35mm which represents the radial distance to the outer edge of the radius on the Sabot Stopper plate hole cut-out. A fixed boundary condition was placed at the edge of the plate.

5.3.1 Aluminum Plate Material Model

Aluminum 6061-T6 is well characterized in the literature, with a Johnson Cook material model being one of the most commonly used in high-speed impact simulations. The Johnson-Cook strength model defines a flow stress that is dependent on strain hardening, strain rate effects, and thermal softening:

$$\sigma_Y = (A + B\varepsilon_p^n)(1 + c \ln \acute{\varepsilon}^*)(1 - T_H^m) \qquad \text{Equation 50}$$

where ε_p is the effective plastic strain, $\acute{\varepsilon}^*$ is the effective normalized plastic strain rate, T_H is the homologous temperature, and A, B, n, c, and m are material constants. The three sets of parentheses in Equation 50 define the stress in terms of strain, strain rate, and temperature respectively [42]. The homologous temperature in LS-DYNA is defined as:

$$T_H = (T-T_R)/(T_M-T_R) \qquad \text{Equation 51}$$

where T is the current temperature, T_R is room temperature, and T_M is the melt temperature [42].

Shang et al. compared four different Johnson Cook material models for Al 6061-T6 for high strain rate deformation purposes in LS-Dyna [60]. The models are summarized in Table 21.

Table 21 – Johnson Cook Material Models for Al 6061-T6 [60]

	A (MPa)	**B (MPa)**	**C**	**n**	**m**	**Tm (K)**
Model 1 [61]	324	114	0.002	0.42	1.34	925
Model 2 [62]	275	500	0.02	0.3	1.0	925
Model 3 [63]	293	121.3	0.002	0.23	1.34	925
Model 4 [64]	289.6	203.4	0.011	0.35	1.34	925

Shang et al. concluded that Models 1 and 3 were suitable for Al 6061-T6, and that Models 2 and 4 were incorrect [60]. The simulations began with Model 1 and then Model 3 was used to determine if there is any difference in the results.

The Gruneisen EOS was used with C = 5240 m/s, S = 1.4, and Gamma = 1.97 as per [65].

5.3.2 Flexible Plate Simulation Discretization Convergence

It was decided to use Lagrangian elements for the aluminum plate since the plate would not fail and the Lagrange method should be able to capture the response accurately with a faster computation time than SPH particles. Specifically, axisymmetric shell elements were used for the plate. The bird was still modeled with SPH elements and the SPH size and time-step size used for the rigid plate simulations was used for the flexible plate simulations as well (SPH size = 0.5mm and TSSFAC = 0.031). It was therefore only necessary to determine the element size for the aluminum plate for this convergence study. For the bird model, the Gruneisen C and S were set to 1450 m/s and 5.02 respectively, while the dynamic viscosity was set to 580 Pa*s. The results of the convergence study are summarized in Table 22.

Table 22 – Convergence Results for Aluminum Plate

Element Size (mm)	**# of Elements Across Plate**	**Peak Deflection (mm)**	**% Change**
4.95	2	34.80	N/A
2.475	4	34.17	-1.82%
1.2375	8	34.11	-0.17%
0.99	10	34.12	0.03%
0.825	12	34.10	-0.05%

Without performing a Grid Convergence Index calculation, it is clear that convergence is achieved with a satisfactory accuracy at an element size of 2.475 mm (4 elements across the thickness of the plate).

5.3.3 Flexible Plate Material Model Check

The simulation from the convergence check was repeated with each of the four Johnson-Cook material models for the aluminum plate defined in section 5.3.1. The results are summarized in Table 23.

Table 23 – Results of Each Material Model for the Aluminum Plate

	Deflection (mm)	**% Change**
Model 1	34.17	N/A
Model 2	30.87	- 9.7 %
Model 3	34.52	1.0 %
Model 4	34.01	- 0.5 %

Material Models 1, 3, and 4 all agree within 1% of each other. Material model 2 was deemed to be invalid by Shang et al. [60] which agrees with it being an outlier in this case. The remaining simulations would continue to use Model 1 for the aluminum plate.

5.3.4 Aluminum Plate Thickness Check

Since there was a discrepancy between the nominal plate thickness and the actual measured thickness, two simulations were performed with only the thickness of the plate changed. For these simulations the gelatin bird used a Gruneisen C and S of 1450 m/s and 2 respectively and a dynamic viscosity of 0. There was only a 3.5% difference in the deflections between the 9.525mm and 9.9mm thick plates as summarized in Table 24.

Table 24 – Results of Thickness of Plate Simulation Comparison

Plate Thickness (mm)	Deflection (mm)	% Change
9.525	34.3	N/A
9.9	33.1	- 3.5 %

5.3.5 Flexible Plate Simulation Results

Simulations were performed of the flexible plate tests for various combinations of Gruneisen parameters and dynamic viscosity. A summary of some of the key results of the simulations is shown in Table 25. None of the results closely matched the experimental data target deflection of 45.29mm, with the lowest error being 23.8%. This lowest error occurred for the case in which the pressure profile matched all target values within 4% and over-predicted the steady-state pressure by 17%. It was expected that this simulation should have over-predicted the deflection. The result of the simulation at the moment of peak deflection is shown in Figure 77.

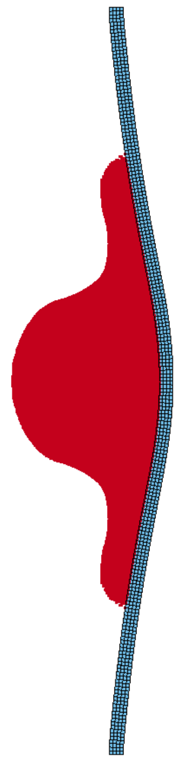

*Figure 77 – Flexible plate simulation result at time of peak deflection for Gruneisen C = 500, S = 1, and dynamic viscosity of 1000 Pa*s.*

The most likely explanation of why the simulations under-predicted the peak deflections is due to the boundary conditions. The simulation assumed a perfectly fixed boundary at the edges where the aluminum plate touches the radius of the cut-out in the Sabot Stopper plate. Investigation of the plates used in the experiments showed clear evidence that gelatin squeezed between the front side of the aluminum plate and the clamping plate. This would indicate that the boundary conditions were not truly fixed as planned. It is likely there was some separation of the clamping surface to allow the gelatin to squeeze into this area. The experimental clamping method should be improved in future work.

To confirm the suspicion that the boundary condition was a probable source of the discrepancy, two simulations were performed: one with a fixed boundary and one with a pinned connection on the rear outer edge to allow rotations about that edge. The peak deflection for the fixed boundary condition was 34.5mm, while the pinned boundary condition peak deflection was 52.2mm (51% higher). The actual average deflection from the experiments was 45.3mm, which is mid-way between the fixed and pinned results. It can therefore be concluded that the discrepancy between the simulations and the experiments for the peak deflection could likely be due to the clamping conditions during the experiments. Budgetary constraints prevented the repetition of tests with an improved clamping condition for this work.

Although this error in experimental set up may have made it impossible to confidently match the exact magnitude of the peak deflections between the simulations and the experiments, there was still value in studying the trends of which parameters affected the peak deflections from a relative standpoint.

Table 25 – Initial Deflection Simulation Results

Gruneisen C (m/s)	Dynamic Viscosity (Pa*s)	Gruneisen S	Peak Pressure Error	Steady-State Error	Peak Impulse Error	Steady-State Impulse Error	Total Impulse Error	Deflection (mm)	% Error from Experimental
500	600	1	-40.8%	-3.1%	-7.5%	-5.3%	-6.0%	34.2	-24.5%
500	1000	1	-1.6%	17.0%	0.6%	4.0%	2.8%	34.5	-23.8%
1000	500	7.3	0.0%	-0.5%	-34.0%	4.7%	-8.4%	34.1	-24.7%
1450	0	2	5.7%	-14.1%	-33.7%	-13.2%	-20.2%	33.1	-26.9%
1450	560	4.95	0.1%	-0.8%	-26.1%	2.1%	-7.5%	34.1	-24.7%
1450	580	5.02	0.0%	3.0%	-27.2%	2.6%	-7.5%	34.2	-24.5%

5.3.6 Flexible Plate Parameter Sensitivity

This section investigates the sensitivity of the peak deflection to the various gelatin bird parameters.

5.3.6.1 Gruneisen C Deflection Sensitivity

The sensitivity of the peak deflection to Gruneisen C was investigated by holding the dynamic viscosity constant at 580 Pa*s and Gruneisen S at 5.02, while varying Gruneisen C only. As summarized in Table 26, the Gruneisen C parameter had negligible effects on the peak deflection.

Table 26 – Gruneisen C Deflection Sensitivity

Gruneisen C (m/s)	**Peak Deflection (mm)**	**% Change**
1000	34.173	N/A
1450	34.168	-0.01%
2000	34.183	0.03%

5.3.6.2 Gruneisen S Deflection Sensitivity

The sensitivity of the peak deflection to Gruneisen S was investigated by holding the dynamic viscosity constant at 580 Pa*s and Gruneisen C at 1450 m/s, while varying Gruneisen S only. As summarized in Table 27, the Gruneisen S parameter has negligible effects on the peak deflection.

Table 27 – Gruneisen S Deflection Sensitivity

Gruneisen S	Peak Deflection (mm)	% Change
2	34.164	N/A
5.02	34.168	0.01%

5.3.6.3 Dynamic Viscosity Deflection Sensitivity

The sensitivity of the peak deflection to dynamic viscosity was investigated by holding the Gruneisen C at 1450 m/s and Gruneisen S at 2, while varying dynamic viscosity only. As summarized in Table 28 and Figure 78, the dynamic viscosity has a significant linear correlation with the peak deflection.

Table 28 – Dynamic Viscosity Deflection Sensitivity

Dynamic Viscosity	Peak Deflection (mm)
0	33.1
580	34.2
1000	34.5
1500	35.1
2000	35.8
5000	40.8
10000	46.4

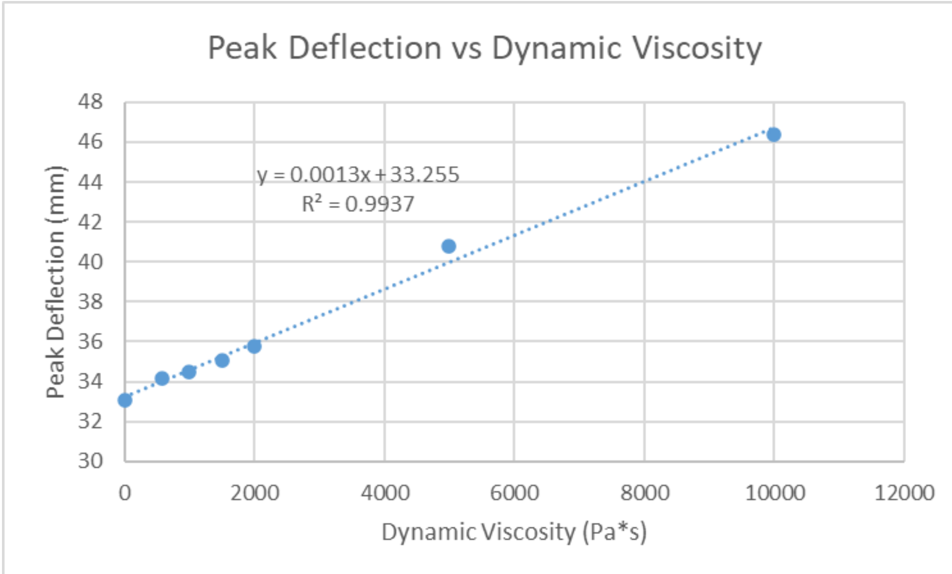

Figure 78 – Peak Deflection vs Dynamic Viscosity

5.3.6.4 Diameter Deflection Sensitivity

The sensitivity of the peak deflection to diameter was investigated using the same models used in section 4.5.4. The Gruneisen C and S were 1450 m/s and 2 respectively with a dynamic viscosity of zero. The length of the gelatin bird was adjusted with the diameter to ensure the mass was not changed. As summarized in Table 29, Figure 79, and Figure 80, the diameter and/or length have a significant linear correlation with the peak deflection. A larger diameter and a shorter length increase the peak deflection. It is important to notice that the peak pressure and steady-state pressures were nearly unchanged, yet the peak deflection changed significantly. Another critical observation is that even though the steady-state and total impulses dropped significantly, the peak defection increased. These results would suggest that the peak impulse is the driving factor for the peak deflection in these simulations. The longer the higher pressures that occur during the peak portion of the pressure profile can be maintained the further the plate will deflect. The steady-state pressure must not be high enough to dictate the peak deflection when compared to those occurring during the peak impulse.

Table 29 – Pressure Profile and Deflection Data for Diameter Sensitivity Studies

Diameter (mm)	Length (mm)	Peak Pressure (MPa)	Steady-State Pressure (MPa)	Peak Impulse (Pa*s)	Steady-State Impulse (Pa*s)	Total Impulse (Pa*s)	Flex Plate Deflection
95	295.46	394.5	14.22	6400	20750	27150	30.3
102.3	258	398	14.67	7051	17968	25019	33.1
110	226.98	395.2	14.77	7409	14688	22098	35.8

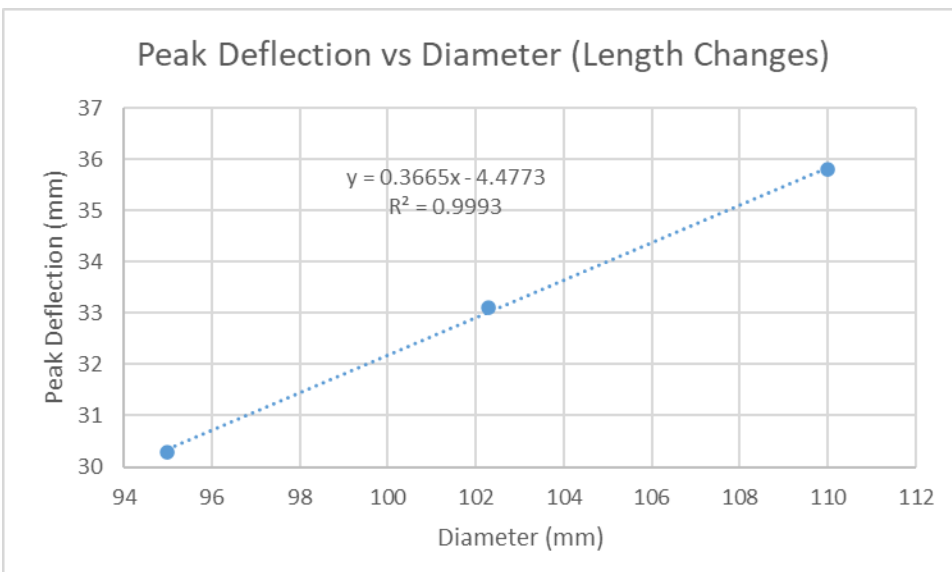

Figure 79 – Peak Deflection vs Diameter (length changed to maintain constant mass)

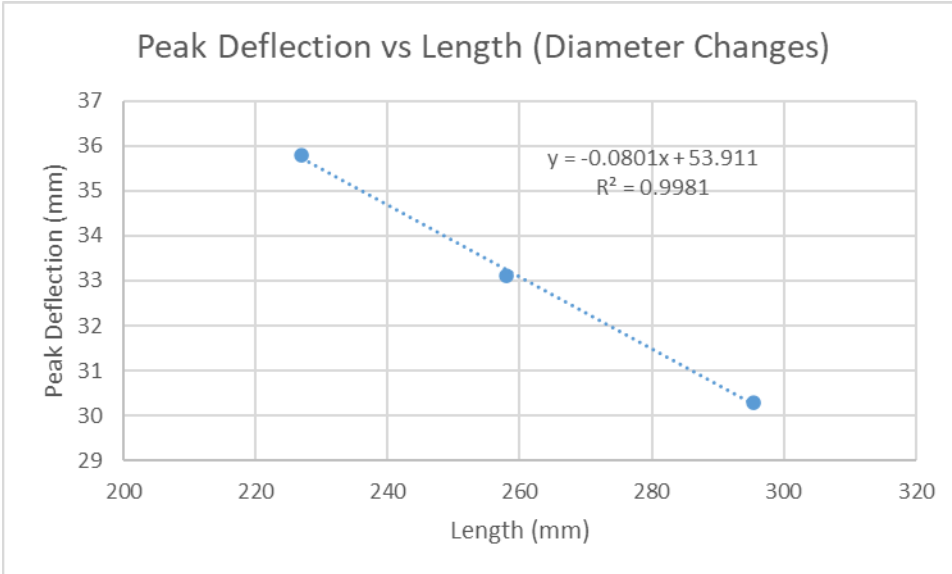

Figure 80 – Peak Deflection vs Length (diameter changed to maintain constant mass)

5.3.6.5 Radius Deflection Sensitivity

The sensitivity of the peak deflection to radius was investigated using the same models that were used in section 4.5.5. The Gruneisen C and S were 1450 m/s and 2 respectively with a dynamic viscosity of zero. The length of the gelatin bird was adjusted with the radius to ensure the mass was not changed. As summarized in Table 30 and Figure 81, the radius/length has a linear correlation with the peak deflection. A shorter radius and length results in an increase in the peak deflection; peak pressure is roughly the same for all three cases. As per the case for the diameter studies, the deflections once again increased despite the steady-state pressure, steady-state impulse, and total impulse all decreasing. This once again points to the importance of the peak impulse in driving the peak deflections. These peak impulse results are not as conclusive as in the diameter studies as the peak impulses for the 39mm and 60mm radii were roughly the same.

Table 30 – Pressure Profile and Deflection Data for Radius Sensitivity Studies

Radius (mm)	Length (mm)	Peak Pressure (MPa)	Steady-State Pressure (MPa)	Peak Impulse (Pa*s)	Steady-State Impulse (Pa*s)	Total Impulse (Pa*s)	Flex Plate Deflection
20	245.71	391.9	13.19	6857	15246	22103	33.7
39	258	391.1	13.84	6710	17143	23853	33.1
60	272.38	395.6	14.75	6730	18382	25112	32.5

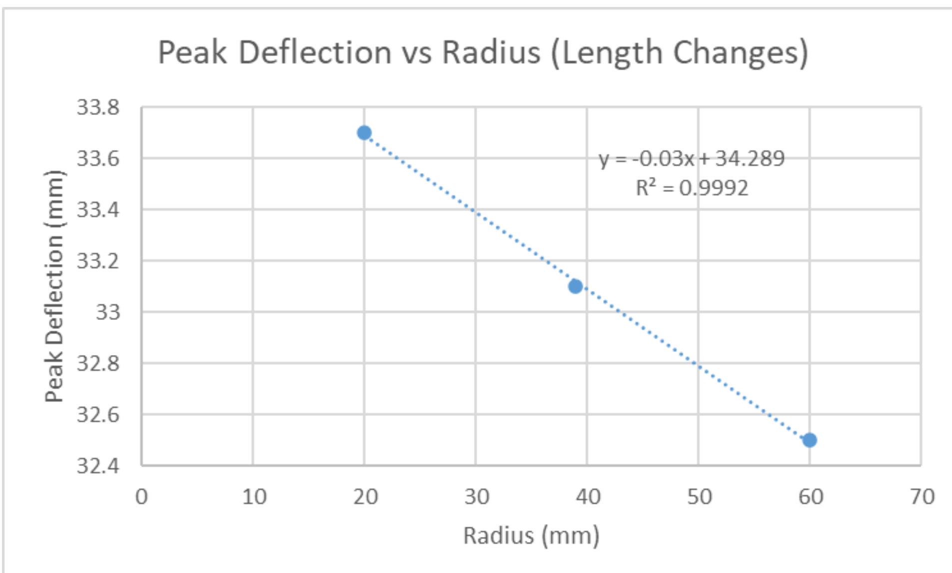

Figure 81 – Peak Deflection vs Radius (length changed to maintain constant mass)

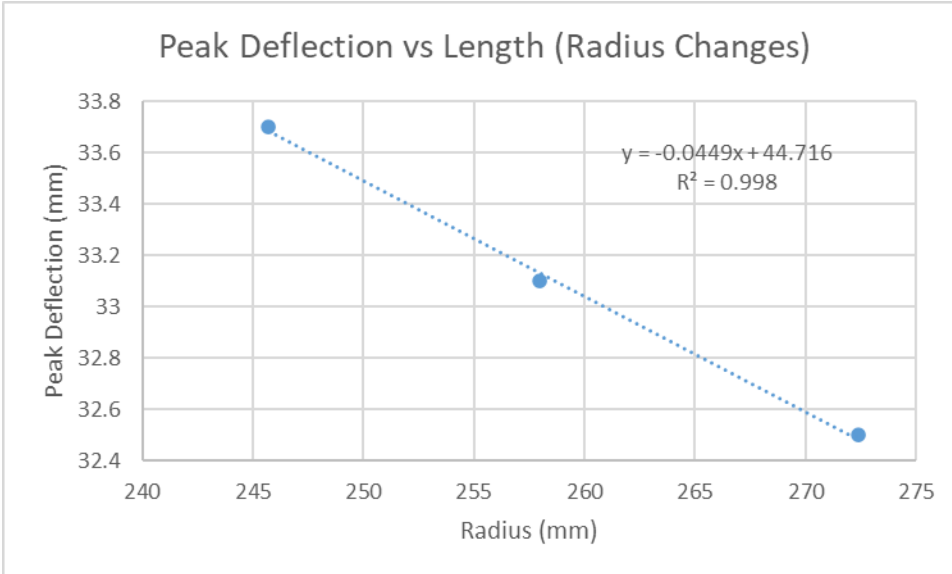

Figure 82 – Peak Deflection vs Length (radius changed to maintain constant mass)

5.3.6.6 Density Deflection Sensitivity

The sensitivity of the peak deflection to density was investigated by holding the Gruneisen C at 1450 m/s and Gruneisen S at 2, with a dynamic viscosity of zero. The length of the gelatin bird was adjusted with the density to ensure the mass was not changed. As summarized in Table 31 and Figure 83, the density has a significant linear correlation with the peak deflection.

Table 31 – Density Deflection Sensitivity

Density (kg/m^3)	Length (mm)	Peak Deflection (mm)
800	301.9	29.3
950	258	33.1
1150	218	37.6

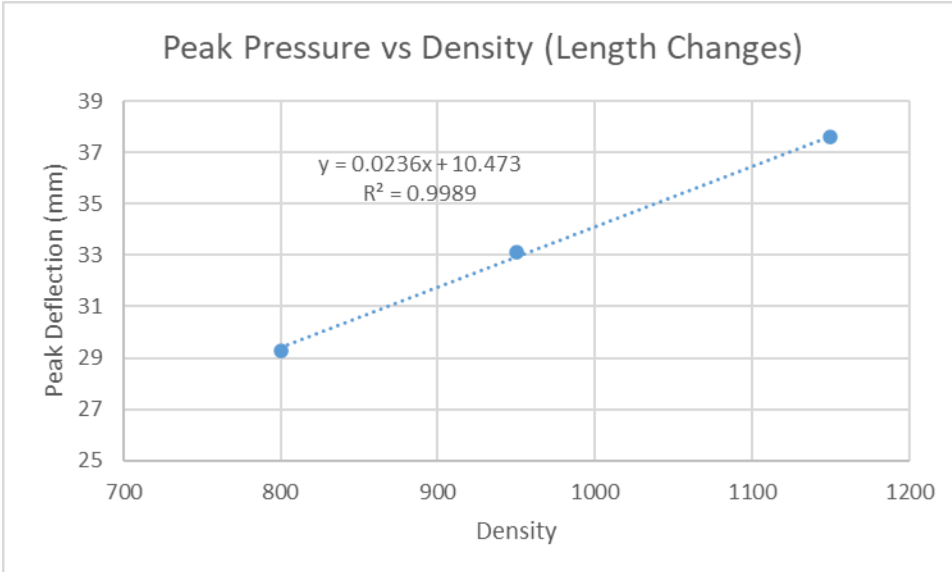

Figure 83 – Peak Deflection vs Density (length changed to maintain constant mass)

Next, instead of adjusting the length to maintain the mass of the gelatin bird, the custom created C++ program was used to generate a bird model with a density gradient from front to back. The results are summarized in Table 32 and Figure 84, which show that the peak deflections increased with increasing front density. These results once again confirmed that the steady-state pressure and steady-state impulse were not driving the peak deflections. The peak deflections once again correlate well with the peak impulse as per Figure 85.

Table 32– Variable Density Deflection Sensitivity Results

Front Density (kg/m^3)	Rear Density (kg/m^3)	Peak Pressure (MPa)	Steady-State Pressure (MPa)	Peak Impulse (Pa*s)	Steady-State Impulse (Pa*s)	Total Impulse (Pa*s)	Peak Deflection (mm)
1300	600	565.9	13.93	9013	16284	25297	35.3
950	950	397.9	14.67	7051	17980	25031	33.1
600	1300	136.4	14.76	4559	18772	23331	31.7

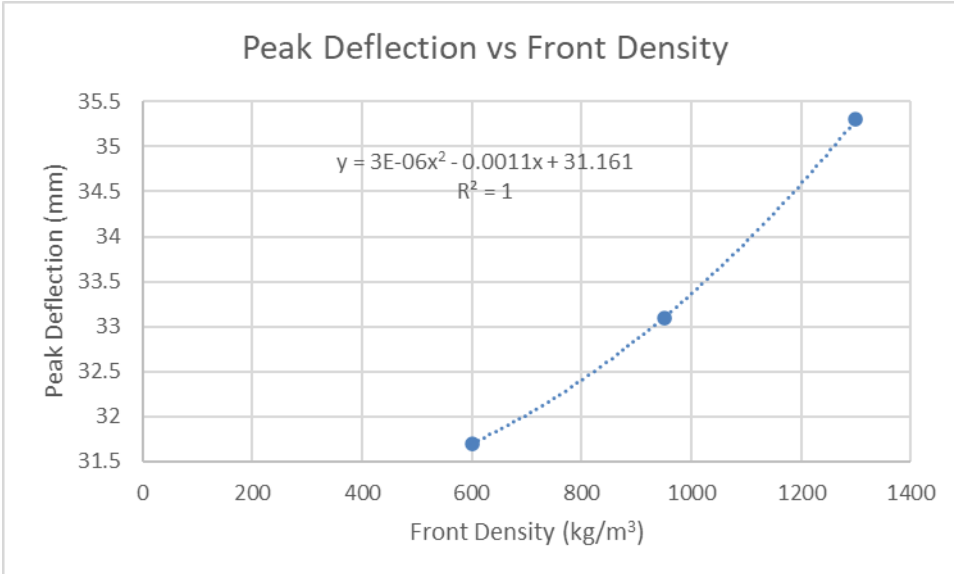

Figure 84 – Peak Deflection vs Front Density

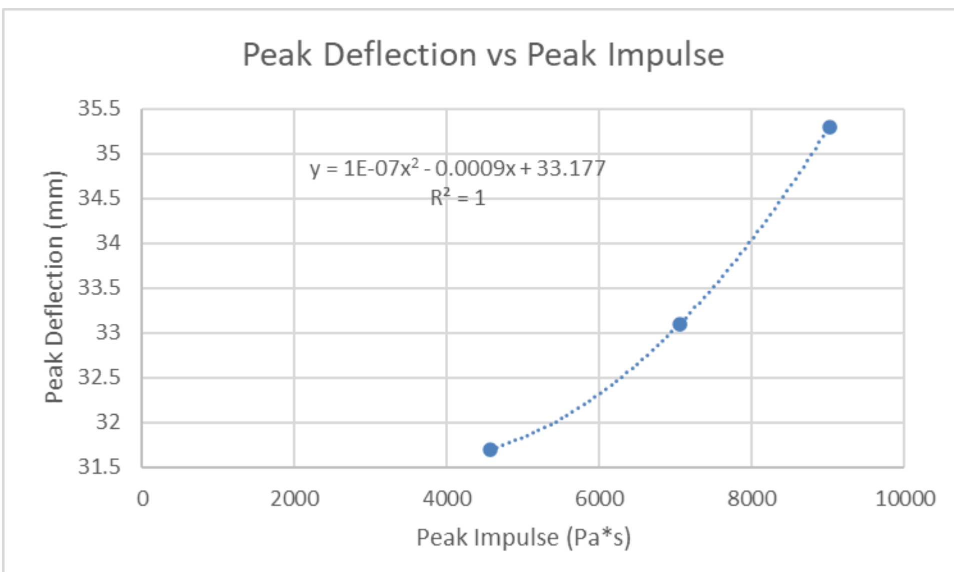

Figure 85 – Peak Deflection vs Peak Impulse for Variable Density

5.4 Shear Thickening Gelatin Bird Model

5.4.1 Significance of a Shear Thickening Gelatin Bird Model

The deviatoric stresses are often ignored in a bird model as it is assumed that the hydrostatic stresses dominate and the deviatoric stresses are negligible. As discussed in section 4.7, the strength of the gelatin bird could increase by three to four orders of magnitude as viscosities on the order of 10^4 Pa*s are plausible at these impact speeds due to the shear thickening behavior of the bird. Therefore, it is very likely that the deviatoric stresses are significant and should be considered.

5.4.2 Development of a Shear Thickening Gelatin Bird Model

It was attempted to write a user defined material model in LS-Dyna that could capture this shear thickening behavior. The work by Subhash et al [54] was the basis for the shear thickening material model. They used a power law model for the dynamic viscosity:

$$\mu = \alpha\dot{\gamma}^{n-1} \qquad \text{Equation 52}$$

Where μ is dynamic viscosity, α is a constant (set to 0.00453 for ballistic gelatin), $\dot{\gamma}$ is the shear strain rate, and n is the exponential term (set to 2.22 for the shear thickening ballistic gelatin) [54].

The deviatoric stress term would then be defined in the same manner as for the LS-Dyna Null material model:

$$\sigma'_{ij} = 2\mu\dot{\varepsilon}'_{ij} \qquad \text{Equation 53}$$

where μ is the dynamic viscosity and $\dot{\varepsilon}'_{ij}$ is the deviatoric strain rate [53]. The dynamic viscosity term would be as calculated using the power law model above.

The LS-Dyna user-defined material model was not able to work as there were issues with the LS-Dyna code using this model with SPH. However, LS-Dyna recently released a new material model called MAT_SPH_VISCOUS which does exactly what the user-defined material model above attempted to do [66]. Unfortunately, attempts to use this new material model once again resulted in some issues from LS-Dyna that made it not possible to use at this time.

5.4.3 Future Recommendations for Shear Thickening Gelatin Bird Model

Although attempts at creating a shear thickening gelatin bird model in LS-Dyna was not achieved during this work, it should be studied for use in bird modeling in future work. Combining this type of shear thickening model with the knowledge of the parametric studies from this thesis could result in creating a model that can be tuned to match a pressure profile and peak deflections from experimental data.

The LS-Dyna models attempted during this work resulted in issues incorporating the strain rate effects properly. The MAT_SPH_VISCOUS model would always result in the same pressure profile even if the parameters were changed by several orders of magnitude. The only variable that would affect the results was the minimum viscosity parameter. It appears it is acting as if the strain rate is always zero and therefore only the minimum viscosity has an effect. The tabulated version was also attempted, and it also just used whatever value was corresponded to zero strain. Further investigation of this, perhaps with the help of ANSYS customer support is suggested.

6 Conclusions and Future Recommendations

6.1 Concluding Remarks

Prior to this research, attempts at developing an appropriate bird model were based on uncertain experimental pressure data. Three popular bird models from previous research were compared against the improved experimental data from this research and it was shown that the pressures could be off by over 100% and in all cases only one variable could be matched to within less than 10% error. In this research, a model was developed that over-predicted the steady-state pressure by 17%, but all other target criteria were matched within 4%. This shows a significant potential for improvement as compared to the previously published material models that were studied.

The pressures resulting from the experiments performed in this work resulted in much higher pressures than were reported in previous published research. A previous EOS predicted a peak pressure of 182 MPa for an impact speed of 170 m/s, while published experimental results for chickens had a peak pressure of much less than this. Previous experimental results for porous gelatin were much lower than the chickens with a peak pressure of 88 MPa at a speed of 171 m/s. The peak pressures achieved in this thesis work were as high as 360 MPa. This is nearly twice as high as the theoretical maximum predicted by previous work and over four times higher than previously reported porous gelatin results.

The previous experimental work resulted in a steady-state pressure of approximately 18.5 MPa for a speed of 155 m/s for a 2kg chicken. Previous experimental steady-state pressure for the porous gelatin was 11.2 MPa at 171 m/s. The maximum recorded steady-state pressure during this thesis work was 16.39 MPa. This is 11% less than that recorded for the chicken, but 46% higher than the pressure recorded for the porous gelatin.

A challenge to developing and validating any bird strike model is the ability to develop an appropriate testing method. It is suspected that one of the key factors in the increase in measured pressures is due to an improvement in sensor quality and data acquisition speeds as the previous experiments were performed nearly 40 years earlier. The other key factor that may have influenced the ability to capture higher pressures was the amount of repetition of tests for a given size and speed of gelatin bird. The 17 tests performed in this thesis work showed the difficulty in capturing the true maximum pressures and the importance of using a statistical approach was demonstrated. The addition of multiple sensors also helped to mitigate the risk of missing the true peak loading conditions.

One of the significant improvements in the approach taken was the consideration of the shape change of the projectile (gelatin bird) prior to impact. Due to the large acceleration forces during launch, the gelatin bird is deforming prior to impact. For this reason, diameter, radius, and density sensitivity studies were performed and showed the importance of peak impulse on deflections as compared to steady-state impulse or even total impulse. Even when the steady-state pressure, steady-state impulse, and total impulse increased significantly, the peak deflection decreased with the peak impulse. Validation testing on flexible plates showed that the longer the higher pressures that occur during the peak portion of the pressure profile can be maintained the more the plate will deflect. The steady-state pressure may not be high enough to dictate the peak deflection when compared to those pressures occurring during the peak impulse. This is an important discovery as there exists previous work that states that the shock regime for a bird with hemispherical ends is relatively negligible. Based on the results of this thesis work, the word negligible should not be used to describe the shock regime in the case of a bird with hemispherical ends.

In section 4.7, it was shown that contrary to popular assumptions, the strength portion of the material model is likely very important at these high strain rates due to the dramatic increase in dynamic viscosity due to the shear thickening behavior of the gelatin bird. This can increase the strength of the bird by 3 to 4 orders of magnitude and should be considered in future gelatin bird models. This result makes sense when considering that as the speed of impact increases shear thickening effects will increase simultaneously. Shear thickening will lead to an increase in strength because it leads to an increase in flow resistance of the striking projectile. It should be noted that an actual bird may not experience these significant shear thickening effects; however, the importance of the deviatoric stresses should remain applicable.

6.2 Reviewing the Research Objectives

There were four primary objectives for this work. The first objective was to develop an experimental method for the generation of statistically significant data that can be used to help characterize a gelatin bird material model that can be used in simulations of specific FAA certification tests. This objective was completed, however, in future experiments a larger surface area for the pressure sensor would be recommended as this would allow for more consistent readings by averaging the pressures over a larger area and would also potentially allow for larger SPH sizes and larger time steps to be used, thus decreasing the computation time of the simulations. Further research is required to determine the root cause of the offset errors that were seen in the pressure profile experimental data.

The second objective was to improve the understanding of how various parameters affect the pressure profile resulting from a gelatin bird strike. Detailed parametric studies that were performed to quantify the effects that each variable has on the pressure profile and peak deflections should enable researchers to more efficiently adjust their models to match experimental bird calibration data in the future. The results from the parametric studies were used to develop a material model for the gelatin bird. A material model was created; however, it did not match all of the desired pressure profile characteristics. The best model over-predicted the steady-state pressure by 17%, but matched all other target characteristics within 4%. This is still a very good fit to the data as compared to bird models that were used in previous works. The best of the three bird models that had claimed to successfully match the bird pressure profiles from rigid plate experiments only had one pressure profile characteristic that was less than 10% error.

The third objective was to determine the importance of the peak pressures and whether they can be ignored as is often done in industry. The peak pressure, and specifically the peak impulse was shown to be very important. The peak impulse was the driving factor for the peak deflection during the validation experiments. The peak pressure regime should not be ignored in future bird models.

The fourth objective was to investigate the importance of the deviatoric stresses as most bird models in the literature ignore the deviatoric stresses. It was shown that due to shear-thickening behavior, the strength of the gelatin bird can increase by three to four orders of magnitude and therefore the deviatoric stresses should not be ignored.

There were several key contributions to the scientific community as the result of this thesis work as summarized below:

- The generation of high-quality bird strike data. Acquiring data at faster acquisition rates than other previous published work improved the odds of capturing peak pressures. Even more important was the demonstration of the need to repeat tests adequately such that a statistical approach can be used to quantify the pressure profiles adequately. This led to the conclusion that the peak pressures are actually much higher than suggested by previous researchers.
- An experimental method was developed for calibrating a bird model for specific conditions. The basis of the experimental method was validated and suggestions

for improving the method for future researchers was determined. This method may be used as the basis for a more robust bird model by repeating the method for various speeds, bird sizes, impact angles, etc.

- The results of the detailed parametric studies in this work will make it possible to quickly adjust material parameters to match experimental data for future researchers. A better understanding of the trends of how each variable affects the pressure profile components was achieved
- It had been typically assumed that the peak pressures have no effect on the resulting damage and that only the steady-state pressure was of importance. The results of this work have shown that the peak impulse is approximately 50% of the steady-state impulse and therefore should be considered significant (especially in materials such as composites which fail at low strains). A study of the flexible plate simulations confirmed the importance of the peak impulse as it was shown consistently that the peak deflections would increase with peak impulse even if the steady-state and total impulses were decreased.
- The importance of shear strength was discovered and demonstrated. It was normally assumed that the bird has no shear strength upon impact and only the hydrodynamic stresses are important. However, this work has shown that shear thickening in gelatin birds may cause these deviatoric stresses to become very important in accurately modeling bird strike behavior. The development of a shear thickening bird model was proposed for future researchers. While the mechanism for shear strength in an actual bird may be different than those for a gelatin bird,

the results show that it is still important to consider these deviatoric terms even for actual birds in the future.

6.3 Assumptions and Limitations

It should be noted that this work was focused on a specific test case that was aimed at generating a simulation that can match those of a certification test. There is an assumption that a gelatin bird is representative of an actual bird used for these certification tests. It is not known whether this is true or not and this should be considered when using these results. An emphasis should also be placed on the amount of potential experimental error due to geometry changes, impact offset from the center of the sensors, non-rigid boundary conditions, etc. The use of a statistical approach for a worst-case scenario was suggested, but it is not known which approach would be adequate. This work should be viewed as a baseline for further research work, which could expand upon this work with the goal of creating a conservative yet accurate approach for performing simulations of bird strikes to improve safety and the likelihood of passing certification tests.

6.4 Future Recommendations

The following are recommendations for future work that could be considered to build upon the approach and results completed in this research:

- In future rigid plate experiments, a larger surface area for the pressure sensor would be recommended as this would allow for more consistent readings by averaging the pressures over a larger area and would also potentially allow for larger SPH sizes and larger time steps to be used, thus decreasing the computation time of the simulations.

- As per the pressure sensor manufacturer's suggestion, kapton foil should be placed over the pressure sensor face during the rigid plate experiments in an attempt to reduce the offset error that can occur potentially due to thermal effects on the sensor. If this does not mitigate the issue enough, then an in depth investigation into the root cause of the offsets should be conducted.
- Other statistical analysis for bird model (e.g., 95^{th} confidence interval) could be used on the rigid plate experiment results.
- Shear thickening material model based on power law of [54] using MAT_SPH_VISCOUS in LS-Dyna.
- Real birds could be used instead of gelatin birds. An investigation could be performed as to whether shear thickening effects occur with real birds or whether other mechanisms lead to the importance of the consideration of the deviatoric terms of the material model for a real bird.
- The tests could be performed using different size birds and for different impact speeds. Various angles of impact could also be studied.
- An investigation into how to correct numerical error for small radii as per section 4.5.5.
- More complex geometries such as larger front diameter with smaller rear diameter to increase the peak impulse while maintaining the density.
- Improve the clamping method for the flexible plate experiments.
- 3D quarter model of flexible plate experiment with bolted connections.

- For the flexible plate experiments, it would be recommended to take DIC measurements on the front side as well (if costs allows) to check if there is separation of the clamping plate

Bibliography

[1] V. Walvekar, "Birdstrike Analysis on Leading Edge of an Aircraft Wing Using a Smooth Particle Hydrodynamics Bird Model," May 2010. [Online]. Available: http://openpdf.info/viewer?url=http://soar.wichita.edu/dspace/bitstream/handle/10057/3339/t10048_Walvekar.pdf%3Fsequence%3D3. [Accessed 25 June 2012].

[2] Transport Canada, "Appendix 5.1 - FAA Airworthiness Requirements for Airframes," Transport Canada, 20 May 2010. [Online]. Available: http://www.tc.gc.ca/eng/civilaviation/publications/tp13549-appendices-appendix5-1-2168.htm. [Accessed 25 February 2012].

[3] K. C. Chuan, "Finite Element Analysis of Bird Strikes on Composite and Glass Panels," 2006. [Online]. Available: http://dynamicslab.mpe.nus.edu.sg/dynamics/Project0506/thesis0506/Finite%20element%20analysis%20of%20bird%20strikes.pdf. [Accessed 26 June 2012].

[4] V. D. Perdikoulis, E. E. Theotokoglou and I. K. Giannopoulos, "Bird Strike Virtual Testing Simulations and Results, For Preliminary Airframe Design Structural Optimization," in *14th World Congress in Computational Mechanics (WCCM)*, 2021.

[5] J. S. Wilbeck, "Impact Behavior of Low Strength Projectiles," July 1978. [Online]. Available: http://www.dtic.mil/cgi-bin/GetTRDoc?AD=ADA060423. [Accessed 22 June 2012].

[6] G. S. Collins, "An Introduction to Hydrocode Modeling," 2 August 2002. [Online]. Available: http://amcg.ese.ic.ac.uk/~gsc/publications/sales_2/download/intro.pdf. [Accessed 15 June 2011].

[7] Y. Chang, "Hydrocode Analysis at APL," *John Hopkins APL Technical Digest, Volume 19, Number 1,* p. 72, 1998.

[8] Century Dynamics Inc. (ANSYS Inc.), "AUTODYN - Explicit Software for Nonlinear Dynamics - Theory Manual, Revision 4.3," Concord, 2005.

[9] J. a. W. R. D. Bonet, Nonlinear Continuum Mechanics for Finite Element Analysis, Cambridge: Cambridge University Press, 1997.

[10] B. Adams, "Simulation of Ballistic Impacts on Armored Civil Vehicles," Eindhoven, 2003.

[11] ANSYS Inc., "ANSYS 13.0 Help: Appendix F. Explicit Dynamics Thoery Guide," SAS IP, Inc., 2010.

[12] G. Black, "Computer Modeling of Blast Loading Effects on Bridges," Easton, 2006.

[13] J. Zuo, "University of South Carolina," 21 August 2006. [Online]. Available: http://www.me.sc.edu/research/jzuo/Contents/ALE/ALE_1.htm. [Accessed 19 October 2011].

[14] X. Quan, N. K. Birnbaum, M. S. Cowler and B. I. Gerber, "Numerical Simulation of Structural Deformation Under Shock and Impact Loads Using a Coupled Multi-Solver Approach," Concord, 2003.

[15] M. Souli, A. Ouahsine and L. Lewin, "ALE formulation for fluid-structure interaction problems," Livermore, 1999.

[16] Creative Commons, "File:Stress tensor.png," 11 October 2009. [Online]. Available: http://commons.wikimedia.org/wiki/File:Stress_tensor.png. [Accessed 18 April 2013].

[17] A. F. Bower, "Applied Mechanics of Solids," 2008. [Online]. Available: http://solidmechanics.org/text/Chapter2_2/Chapter2_2.htm. [Accessed 2 September 2011].

[18] E. Pierazzo and G. Collins, "A Brief Introduction to Hydrocode Modeling of Impact Cratering," Tucson.

[19] ANSYS Inc., "ANSYS LS-Dyna User's Guide," Canonsburg, 2009.

[20] G. R. Johnson, R. A. Stryk, T. J. Holmquist and S. R. Beissel, "Numerical Algorithms in a Lagrangian Hydrocode," Hopkins, 1997.

[21] J. Von Neumann and R. D. Richtmeyer, "A Method for the Numerical Calculation of Hydrodynamic Shocks," *Journal of Applied Physics,* vol. 21, pp. 232-237, 1950.

[22] J. O. Hallquist, "LS-DYNA Theory Manual," Livermore, 2006.

[23] Engineering Design Analysis, "Implicit & Explicit Finite Element Analysis," April 2011. [Online]. Available: http://engineeringdesignanalysis.blogspot.com/2011/04/implicit-explicit-finite-element.html. [Accessed 14 October 2011].

[24] K. H. a. T. E. A. Huebner, The Finite Element Method for Engineers, New York: John Wiley & Sons, 1982.

[25] S. Imaoka, "Ansys.net," 28 June 2001. [Online]. Available: http://ansys.net/?mycat=tnt_sheldon13. [Accessed 14 October 2011].

[26] K. Subbaraj and M. A. Dokainish, "A Survey of Direct Time-Integration Methods in Computational Structural Dynamics - II. Implicit Methods," *Computers & Structures Vol. 32, No. 6,* pp. 1387-1401, 1989.

[27] C. J. Hayhurst, R. A. Clegg, I. H. Livingstone and N. J. Francis, "The Application of SPH Techniques in AUTODYN-2D to Ballistic Impact Problems," Horsham, 1996.

[28] DYNAmore, "IS YOUR MESH REFINED ENOUGH? Estimating Discretization Error using GCI," 2008. [Online]. Available: http://www.dynamore.de/de/download/papers/forum08/dokumente/I-I-03.pdf. [Accessed 17 October 2013].

[29] P. J. Roache, "Quantification of Uncertainty in Computational Fluid Dynamics," *Annual Reviews Fluid Mechanics,* vol. 29, pp. 123-160, 1997.

[30] J. P. Barber, H. R. Taylor and J. S. Wilbeck, "Bird Impact Forces and Pressures on Rigid and Compliant Targets," May 1978. [Online]. Available: http://www.dtic.mil/cgi-bin/GetTRDoc?Location=U2&doc=GetTRDoc.pdf&AD=ADA061313. [Accessed 25 June 2012].

[31] M. A. McCarthy, J. R. Xiao, C. T. McCarthy, A. Kamoulakos, J. Ramos, J. P. Gallard and V. Melito, "Modelling of Bird Strike on an Aircraft Wing Leading Edge Made from Fibre Metal Laminates - Part 2: Modelling of Impact with SPH Bird Model," *Applied Composite Materials,* vol. 11, pp. 317-340, 2004.

[32] L. S. Nizampatnam, "Models and Methods for Bird Strike Load Predictions," December 2007. [Online]. Available: http://soar.wichita.edu/dspace/bitstream/handle/10057/1494/d07030.pdf?sequence=1. [Accessed 28 June 2012].

[33] J. S. Wilbeck and J. L. Rand, "The Development of a Substitute Bird Model," *Journal of Engineering for Power,* vol. 103, no. 4, pp. 725-730, 1981.

[34] A. J. Tudor, "Bird Injestion Research at Rolls-Royce," in *Symposium on the Mechanical Reliability of Turbo-Machinery Blading*, Derby and District College of Technology, 1968.

[35] R. Doubrava, J. Vlach, M. Oberthor, O. Vich and P. Belsky, "Bird strike tests, analyses, and design optimisation of a tilt-rotor aircraft composite inlet," *Engineering Failure Analysis,* vol. 161, 2024.

[36] L. Davison, Fundamentals of Shock Wave Propagation in Solids, Tijeras, New Mexico: Springer-Verlag Berlin Heidelberg, 2008.

[37] M. Arienti, E. Morano and E. Shepherd, "Shock and detonation modeling with the Mie-Gruneisen equation of state," 22 April 2004. [Online]. Available: http://www2.galcit.caltech.edu/EDL/publications/reprints/galcit_fm99-8.pdf. [Accessed 26 June 2012].

[38] ANSYS Inc., "ANSYS 11.0 Help: Material Models," 2007. [Online]. Available: http://www.kxcad.net/ansys/ANSYS/AUTODYN/AUTODYN_Help.htm#Material_Models/. [Accessed 7 September 2011].

[39] P. Boogard, H. J. Verbeek, M. Stuivinga and A. C. Van der Steen, "General Shock Wave Equation of State for Solids," *American Institute of Physics - Journal of Applied Physics,* vol. 78, no. 9, pp. 5335-5344, 1 November 1995.

[40] W. M. Isbell, F. H. Shipman and A. H. Jones, "Hugoniot Equation of State Measurements for Eleven Materials to Five Megabars," December 1968. [Online]. Available: http://www.dtic.mil/cgi-bin/GetTRDoc?AD=AD0721920. [Accessed 26 June 2012].

[41] Livermore Software Technology Corporation, "LS-DYNA Theory Manual," Livermore, 2006.

[42] Livermore Software Technology Corporation, "LS-DYNA Keyword User's Manual," May 2007. [Online]. Available: http://lstc.com/pdf/ls-dyna_971_manual_k.pdf. [Accessed 25 February 2012].

[43] R. Hedayati and M. Sadighi, Bird Strike : An Experimental, Theoretical and Numerical Investigation, Elsevier Science & Technology, 2015.

[44] R. Hedayati, M. Sadighi and M. Mohammadi-Aghdam, "On the difference of pressure readings from the numerical, experimental and theoretical results in different bird strike studies," *Aerospace Science and Technology,* vol. 32, no. 1, pp. 260-266, 2014.

[45] J. Liu, Y. Li and X. Gao, "Bird strike on a flat plate: Experiments and numerical simulations," *Internatiional Jounral of Impact Engineering,* vol. 70, pp. 21-37, 2014.

[46] Y. Zhang and Y. Zhou, "Evaluating constitutive models of smoothed particle hydrodynamics for bird-strike simulation," *International Journal of Crashworthiness,* vol. 29, no. 3, pp. 547-556, 2024.

[47] J. Cwiklak, E. Kobialka and A. Gos, "Experimental and Numerical Investigations of Bird Models for Bird Strike Analysis," *Energies,* vol. 15, no. 10, 2022.

[48] Z. Song, Q. Wang, C. Yu, R. Chen, D. Guo and L. Hou, "A Novel FEM-DEM Adaptive Transfer Method for Bird-Strike Simulation," *Journal of Aerospace Engineering,* vol. 36, no. 1, 2022.

[49] M. A. Lavoie, A. Gakwaya, M. Nejad Ensan, D. G. Zimcik and D. Nandlall, "Bird's substitute tests results and evaluation of available numerical methods," *International Journal of Impact Engineering,* vol. 36, no. 10-11, pp. 1276-1287, 2009.

[50] M. Anghileri, L. M. L. Castelletti and V. Mazza, "Birdstrike: approaches to the analysis of impacts with penetration," *WIT Transactions on Engineering Sciences,* vol. 49, pp. 63-74, 2005.

[51] J. Frischbier and A. Kraus, "Multiple Stage Turbofan Bird Ingestion Analysis with ALE and SPH Methods," 2005. [Online]. Available: http://www.mtu.de/en/technologies/engineering_news/development/Frischbier_Multiple_stage_turbofan_en.pdf. [Accessed 29 June 2012].

[52] Livermore Software Technology (LST), and ANSYS Company, "LS-DYNA Keyword User's Manual Volume I," Livermore, California, 2021.

[53] Livermore Software Technology (LST), and ANSYS Company, "LS-DYNA Keyword User's Manual Volume II - Material Models," Livermore, California, 2021.

[54] G. Subhash, J. Kwon, R. Mei and D. F. Moore, "Non-Newtonian Behavior of Ballistic Gelatin at High Shear Rates," *Experimental Mechanics,* vol. 52, pp. 551-560, 2012.

[55] J. Kwon and G. Subhash, "Compressivestrainratesensitivityofballisticgelatin," *JournalofBiomechanics,* vol. 43, pp. 420-425, 2010.

[56] F. E. Trinklein, Modern Physics, New York: Austin : Holt, Rinehart and Winston : Harcourt Brace Jovanovich, 1990.

[57] J. Cook, R. Bouchard and S. Emelianov, "Tissue-mimicking phantoms for photoacoustic and ultrasonic imaging," *Biomedical Optics Express,* vol. 2, no. 11, 2011.

[58] V. Pickerd, "Optimisation and Validation of the ARAMIS Digital Image Correlation System for use in Large-scale High Strain-rate Events," Australian Government Department of Defence, Maritime Division - Defence Science and Technology Organisation, Victoria, Australia, 2013.

[59] H. Schreier, J.-J. Orteu and M. A. Sutton, Image Correlation for Shape, Motion and Deformation Measurements, New York: Springer, 2009.

[60] J. Shang, S. Hatkevich and L. Wilkerson, "Experimental Study and Numerical Simulation of Electromagnetic Tube Expansion," in *5th International Conference on High Speed Forming*, 2012.

[61] B. Corbett, "Numerical simulations of target hole diameters for hypervelocity impacts," *International Journal of Impact Engineering,* vol. 33, pp. 431-440, 2006.

[62] A. Elsen, M. Ludwig, R. Schaefer and P. Groche, "Fundamentals of EMPT-Welding," in *Proceedings of 4th International Conference on High Speed Forming*, Columbus, 2010.

[63] W. Rule, "A numerical scheme for extracting strength model coefficients from Taylor test data," *International Journal of Impact Engineering,* vol. 19, pp. 797-810, 1997.

[64] J. Fish, "Al 6061-T6 - elastomer impact simulations. Technical Report," 2005.

[65] J. &. Cook, "LA-4167-MS Selected Hugoniots EOS," in *7th Int. Symp. Ballistics*, 1969.

[66] Livermore Software Technology Corporation (LSTC), "LS-DYNA Keyword User's Manual Volume II - Material Models," Livermore, California, 2020.

[67] PCB Piezotronics, "Model 109C12 Product Specification," 2013. [Online]. Available: http://www.pcb.com/Products.aspx?m=109C12#.UeRJuczNiM8. [Accessed 15 July 2013].

[68] Bird Strike Committee USA, "Bird Strike Committee USA," 29 August 2012. [Online]. Available: http://www.birdstrike.org/. [Accessed 10 September 2012].

[69] C. Beam, "It's a Bird, It's a Plane...," The Slate Group, 15 January 2009. [Online]. Available: http://www.slate.com/articles/news_and_politics/explainer/2009/01/its_a_bird_its_a_plane_.html. [Accessed 24 February 2012].

[70] Continuum Mechanics, "Hydrostatic & Deviatoric Stresses," [Online]. Available: http://www.continuummechanics.org/cm/hydrodeviatoricstress.html. [Accessed 4 April 2013].

[71] Livermore Software Technology Corporation (LSTC Inc) and DYNAmore GmbH, "LS-DYNA Support - Equation of State," 2012. [Online]. Available: http://www.dynasupport.com/howtos/general/equation-of-state. [Accessed 20 August 2012].

[72] Merriam-Webster Inc., "Merriam Webster," 2013. [Online]. Available: http://www.merriam-webster.com/dictionary/empennage. [Accessed 9 September 2013].

[73] L. Kwasniewski, "Application of grid convergence index in FE computation," *Bulletin of the Polish Academy of Sciences: Technical Sciences,* vol. 61, no. 1, pp. 123-128, 2013.

[74] F. Allaeys, G. Luyckx, W. Van Paepegem and J. Degrieck, "Numerical and experimental investigation of the shock and steady state pressures in the bird material during bird strike," *International Journal of Impact Engineering,* vol. 107, pp. 12-22, 2017.

Appendix A – Gelatin Bird Mold Drawings

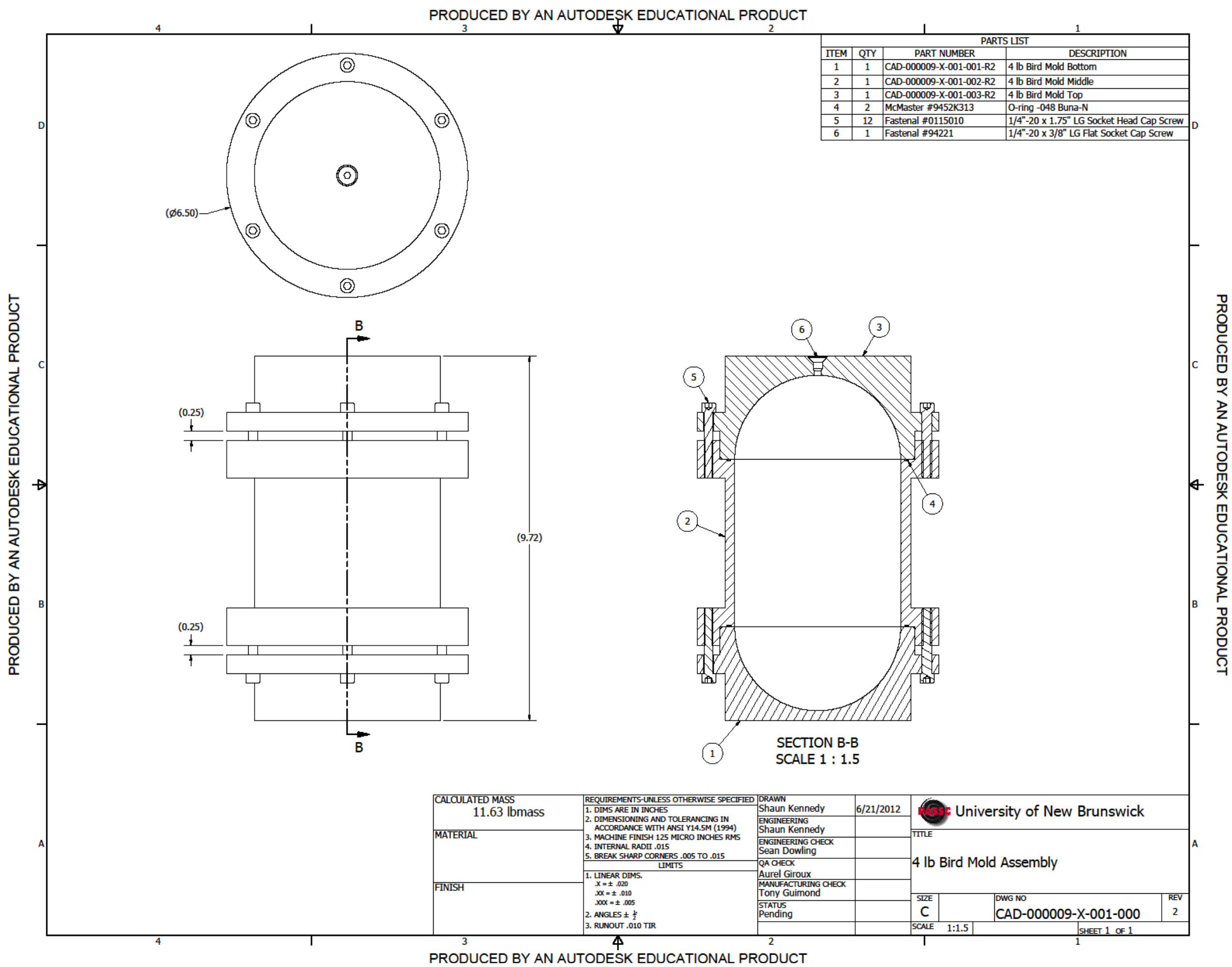

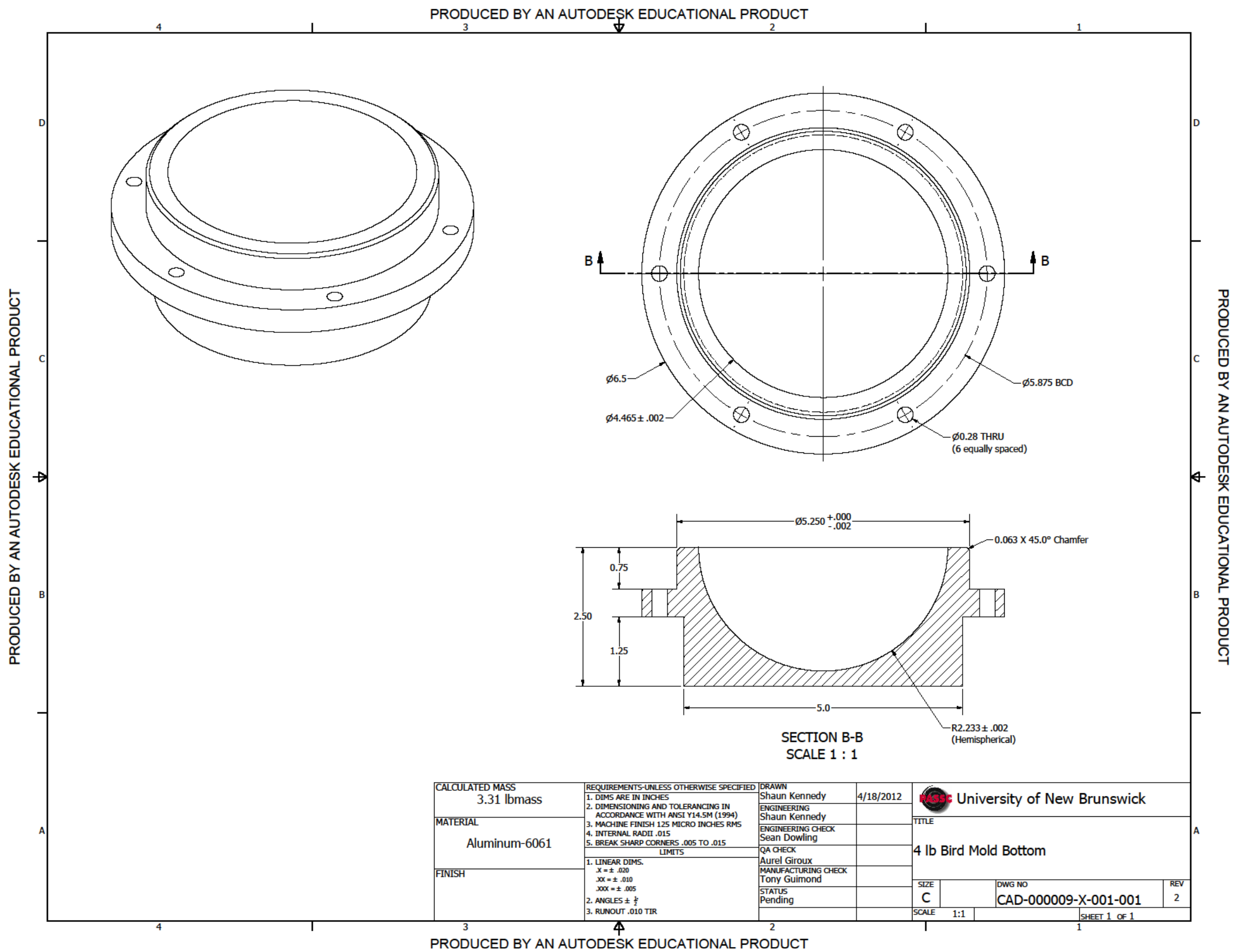
PRODUCED BY AN AUTODESK EDUCATIONAL PRODUCT
B
B
Ø6.5
Ø4.465 ± .002
Ø5.875 BCD
Ø0.28 THRU
(6 equally spaced)
Ø5.250 +.000 -.002
0.063 X 45.0° Chamfer
0.75
2.50
1.25
5.0
R2.233 ± .002
(Hemispherical)
SECTION B-B
SCALE 1 : 1
CALCULATED MASS
3.31 lbmass
MATERIAL
Aluminum-6061
FINISH
REQUIREMENTS-UNLESS OTHERWISE SPECIFIED
1. DIMS ARE IN INCHES
2. DIMENSIONING AND TOLERANCING IN ACCORDANCE WITH ANSI Y14.5M (1994)
3. MACHINE FINISH 125 MICRO INCHES RMS
4. INTERNAL RADII .015
5. BREAK SHARP CORNERS .005 TO .015
LIMITS
1. LINEAR DIMS.
.X = ± .020
.XX = ± .010
.XXX = ± .005
2. ANGLES ± 1/2
3. RUNOUT .010 TIR
DRAWN
Shaun Kennedy
4/18/2012
ENGINEERING
Shaun Kennedy
ENGINEERING CHECK
Sean Dowling
QA CHECK
Aurel Giroux
MANUFACTURING CHECK
Tony Guimond
STATUS
Pending
University of New Brunswick
TITLE
4 lb Bird Mold Bottom
SIZE
C
DWG NO
CAD-000009-X-001-001
REV
2
SCALE
1:1
SHEET 1 OF 1
PRODUCED BY AN AUTODESK EDUCATIONAL PRODUCT

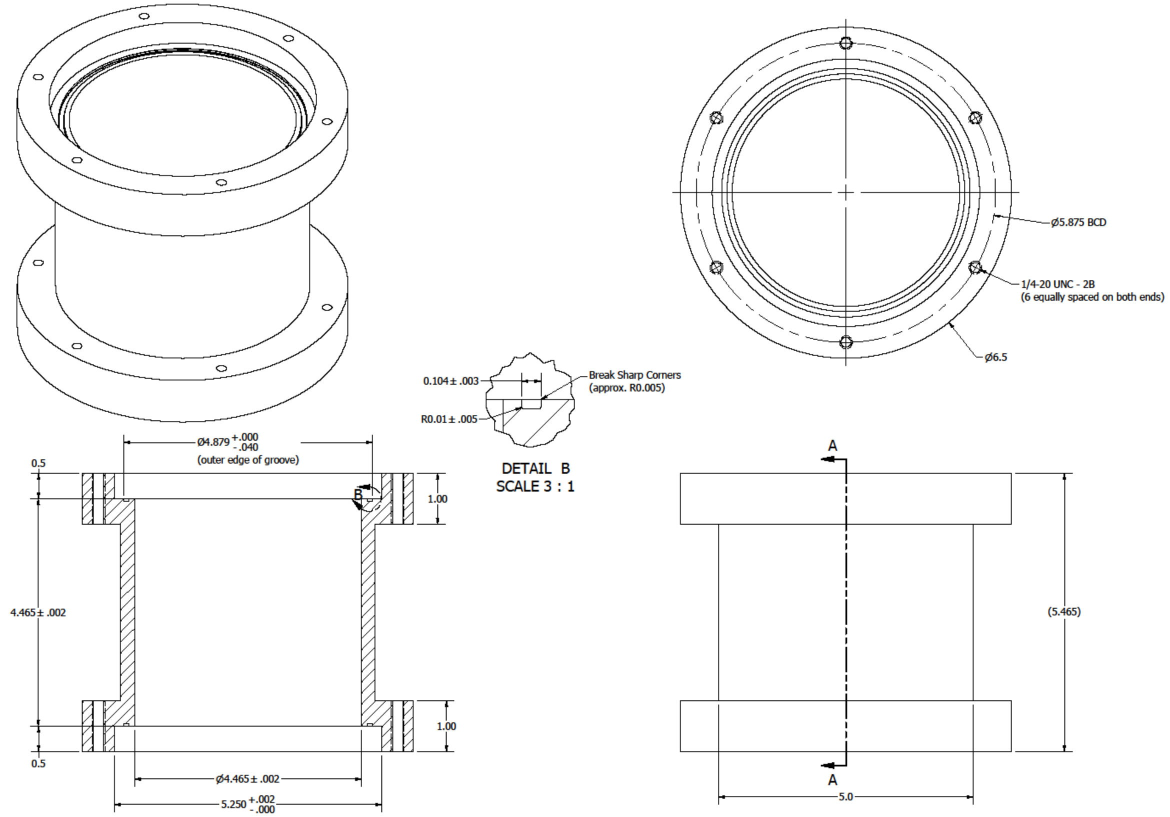

SECTION A-A
SCALE 1 : 1.2

CALCULATED MASS 4.142 lbmass	REQUIREMENTS-UNLESS OTHERWISE SPECIFIED 1. DIMS ARE IN INCHES 2. DIMENSIONING AND TOLERANCING IN ACCORDANCE WITH ANSI Y14.5M (1994) 3. MACHINE FINISH 125 MICRO INCHES RMS 4. INTERNAL RADII .015 5. BREAK SHARP CORNERS .005 TO .015	DRAWN Shaun Kennedy	4/18/2012	University of New Brunswick
MATERIAL Aluminum-6061		ENGINEERING Shaun Kennedy		TITLE 4 lb Bird Mold Middle
	LIMITS 1. LINEAR DIMS. .X = ± .020 .XX = ± .010 .XXX = ± .005 2. ANGLES ± ½° 3. RUNOUT .010 TIR	ENGINEERING CHECK Sean Dowling		
FINISH		QA CHECK Aurel Giroux		SIZE C
		MANUFACTURING CHECK Tony Guimond		DWG NO CAD-000009-X-001-002
		STATUS Pending		REV 2
				SCALE 1:1.2 SHEET 1 OF 1

PRODUCED BY AN AUTODESK EDUCATIONAL PRODUCT
PRODUCED BY AN AUTODESK EDUCATIONAL PRODUCT
PRODUCED BY AN AUTODESK EDUCATIONAL PRODUCT

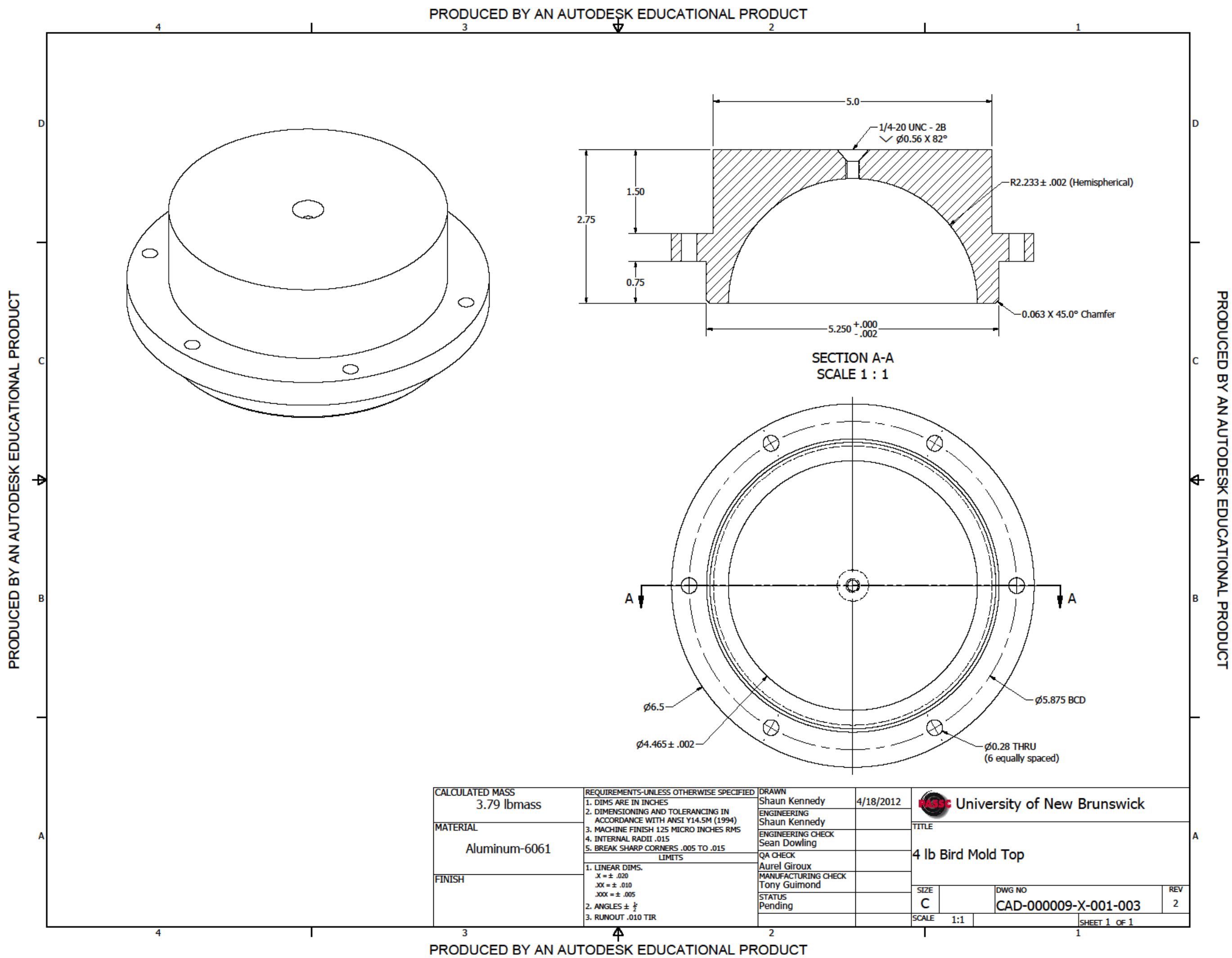
PRODUCED BY AN AUTODESK EDUCATIONAL PRODUCT
5.0
1/4-20 UNC - 2B
Ø0.56 X 82°
R2.233 ± .002 (Hemispherical)
1.50
2.75
0.75
0.063 X 45.0° Chamfer
5.250 +.000 -.002
SECTION A-A
SCALE 1 : 1
A
A
Ø6.5
Ø4.465 ± .002
Ø5.875 BCD
Ø0.28 THRU
(6 equally spaced)
CALCULATED MASS
3.79 lbmass
MATERIAL
Aluminum-6061
FINISH
REQUIREMENTS-UNLESS OTHERWISE SPECIFIED
1. DIMS ARE IN INCHES
2. DIMENSIONING AND TOLERANCING IN ACCORDANCE WITH ANSI Y14.5M (1994)
3. MACHINE FINISH 125 MICRO INCHES RMS
4. INTERNAL RADII .015
5. BREAK SHARP CORNERS .005 TO .015
LIMITS
1. LINEAR DIMS.
.X = ± .020
.XX = ± .010
.XXX = ± .005
2. ANGLES ± ½
3. RUNOUT .010 TIR
DRAWN
Shaun Kennedy
4/18/2012
ENGINEERING
Shaun Kennedy
ENGINEERING CHECK
Sean Dowling
QA CHECK
Aurel Giroux
MANUFACTURING CHECK
Tony Guimond
STATUS
Pending
University of New Brunswick
TITLE
4 lb Bird Mold Top
SIZE
C
DWG NO
CAD-000009-X-001-003
REV
2
SCALE
1:1
SHEET 1 OF 1
PRODUCED BY AN AUTODESK EDUCATIONAL PRODUCT
PRODUCED BY AN AUTODESK EDUCATIONAL PRODUCT
PRODUCED BY AN AUTODESK EDUCATIONAL PRODUCT

Appendix B – Rigid Plate Drawing R1

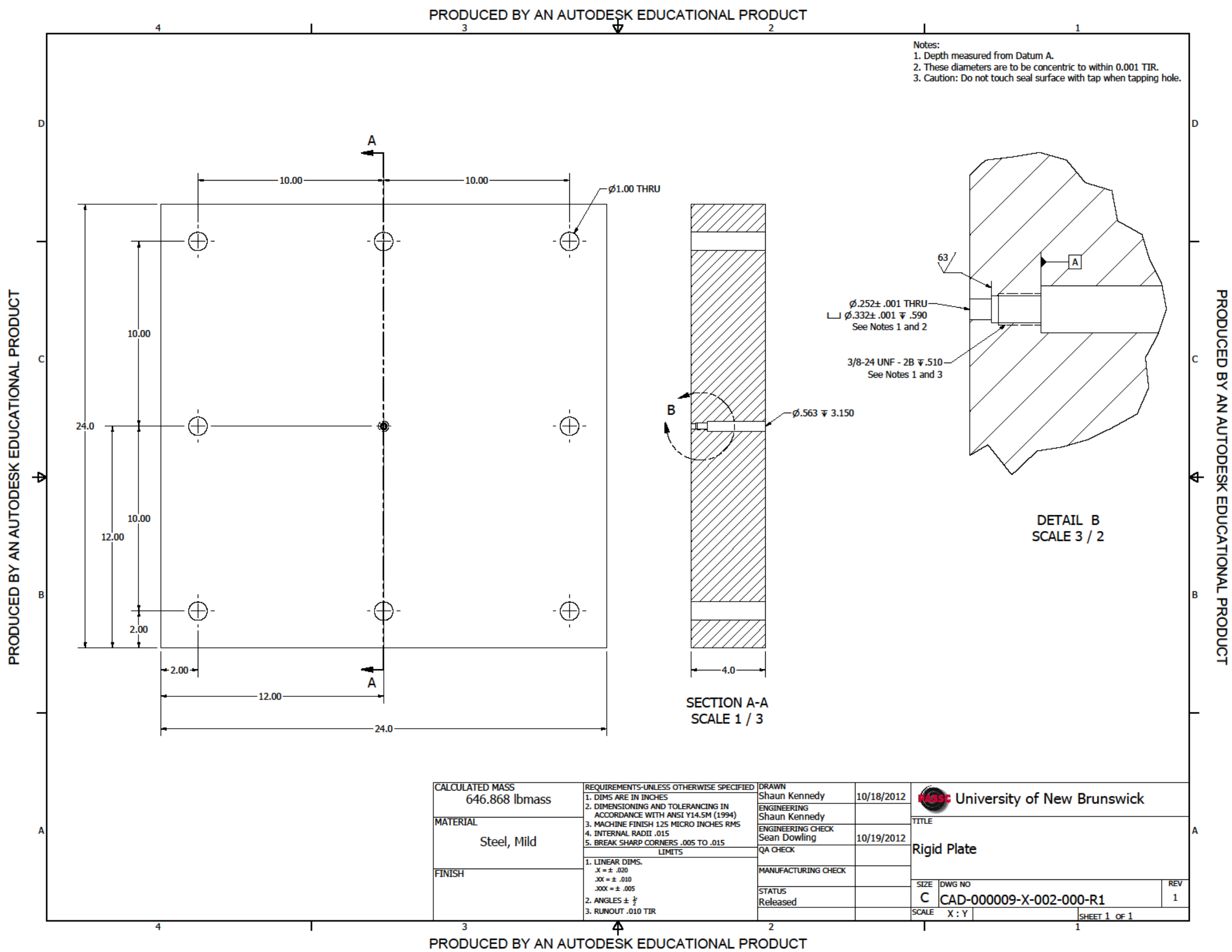

Appendix C - Rigid Plate Drawing R2

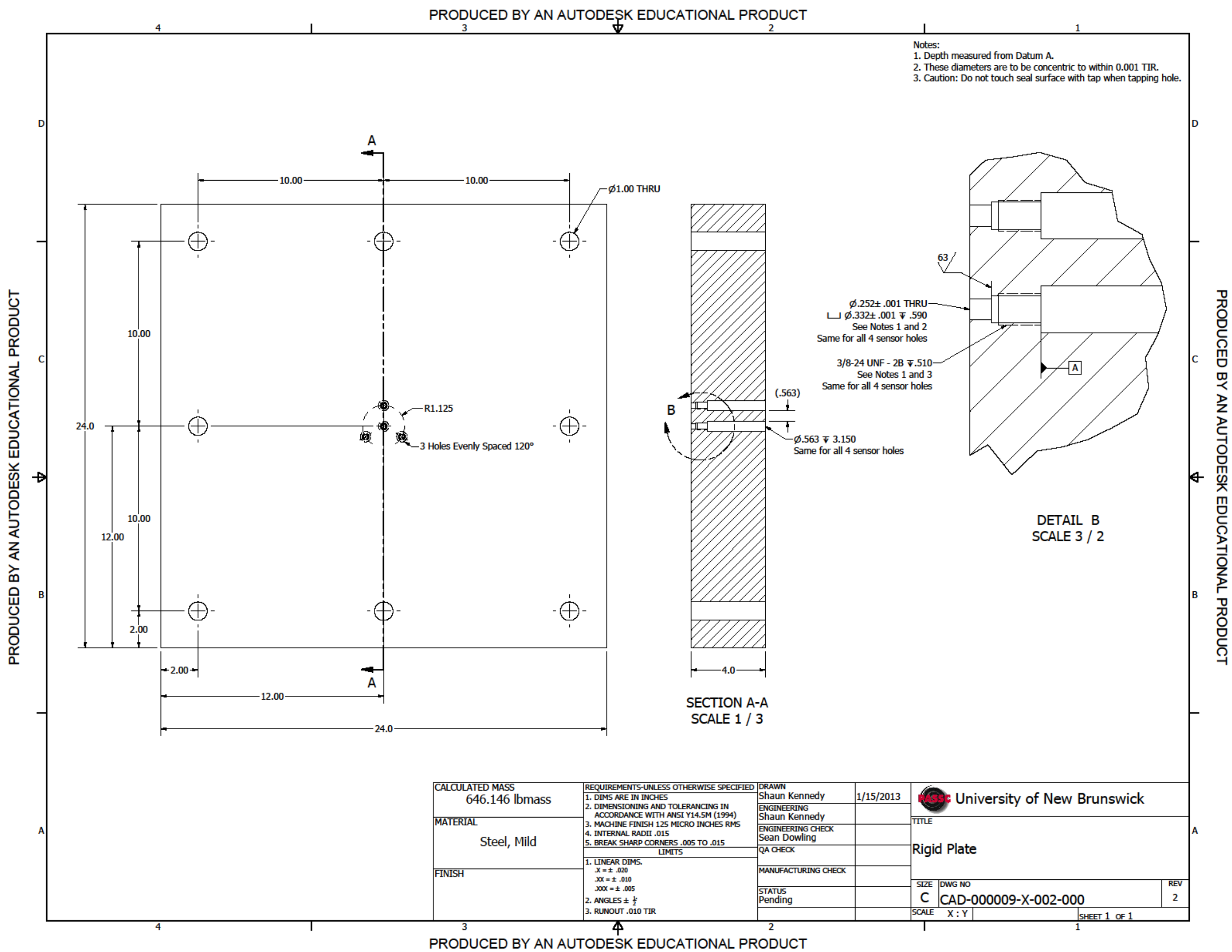

Appendix D – PCB Pressure Sensor Model 109C12 Spec. Sheet [67]

Product Specifications

	ENGLISH	SI
Performance		
Measurement Range	100000 psi	690000 kPa
Sensitivity (±15 %)	0.07 mV/psi	0.010 mV/kPa
Maximum Pressure	125000 psi	862000 kPa
Resolution	2.0 psi	13.8 kPa
Resonant Frequency	≥400 kHz	≥400 kHz
Rise Time	≤2.0 μ sec	≤2.0 μ sec
Non-Linearity	≤2.0 % FS	≤2.0 % FS
Environmental		
Acceleration Sensitivity	≤0.02 psi/g	≤0.015 kPa/(m/s²)
Temperature Range (Operating)	-100 to +275 °F	-73 to +135 °C
Temperature Coefficient of Sensitivity	≤0.07 %/°F	≤0.126 %/°C
Maximum Flash Temperature	3000 °F	1650 °C
Maximum Vibration	2000 g pk	19620 m/s² pk
Maximum Shock	50000 g pk	490330 m/s² pk
Electrical		
Output Polarity	Positive	Positive
Discharge Time Constant	≥2000 sec	≥2000 sec
Excitation Voltage	20 to 30 VDC	20 to 30 VDC
Constant Current Excitation	2 to 20 mA	2 to 20 mA
Output Impedance	≤100 Ohm	≤100 Ohm
Output Bias Voltage	8 to 14 VDC	8 to 14 VDC
Physical		
Sensing Geometry	Compression	Compression
Sensing Element	Quartz	Quartz
Housing Material	C-300	C-300
Diaphragm	C-300	C-300
Sealing	Epoxy	Epoxy
Electrical Connector	10-32 Coaxial Jack	10-32 Coaxial Jack
Weight	0.6 oz	17 gm

Appendix E – Sample Gelatin Bird Shot Pressure Profiles

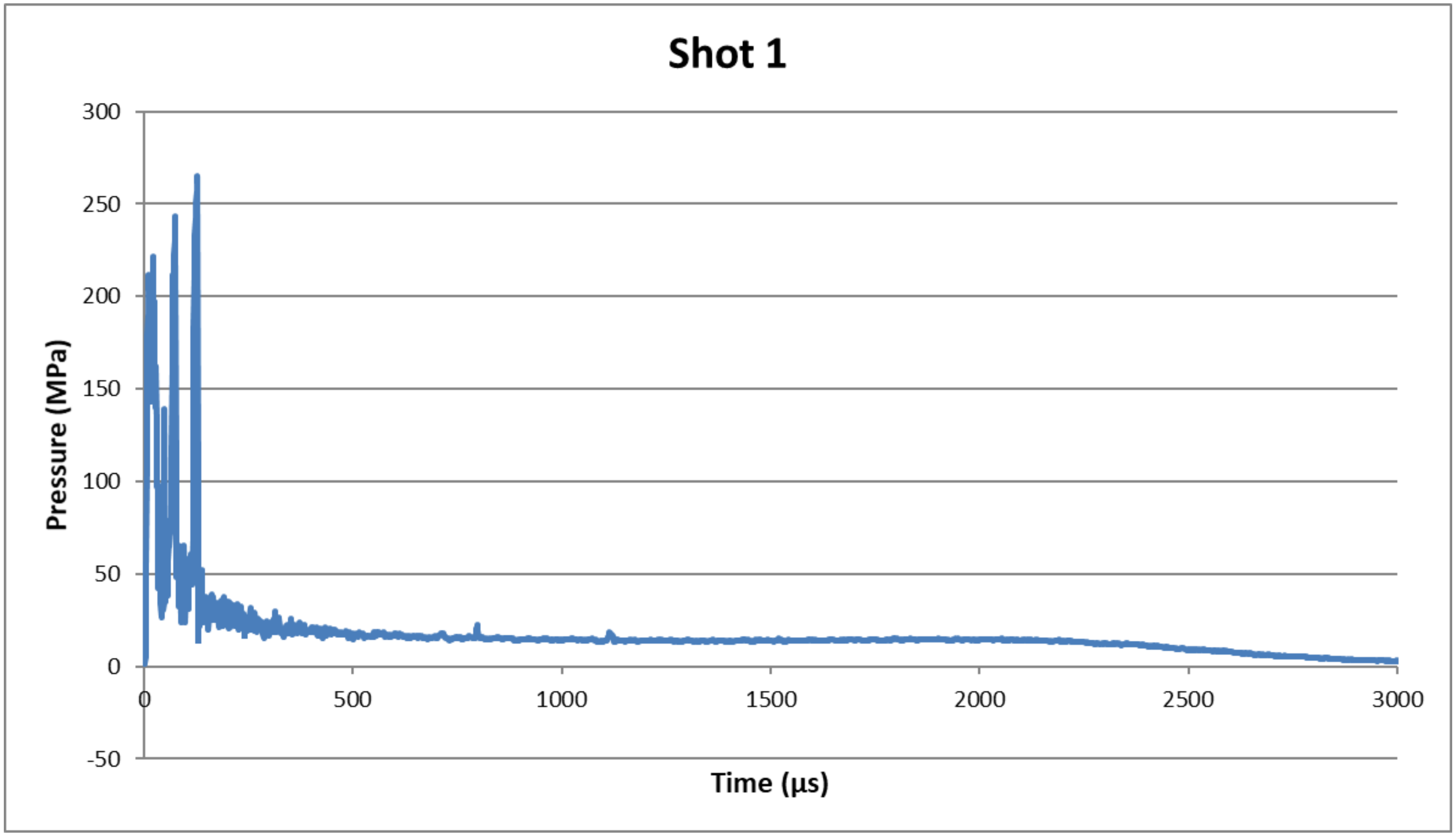

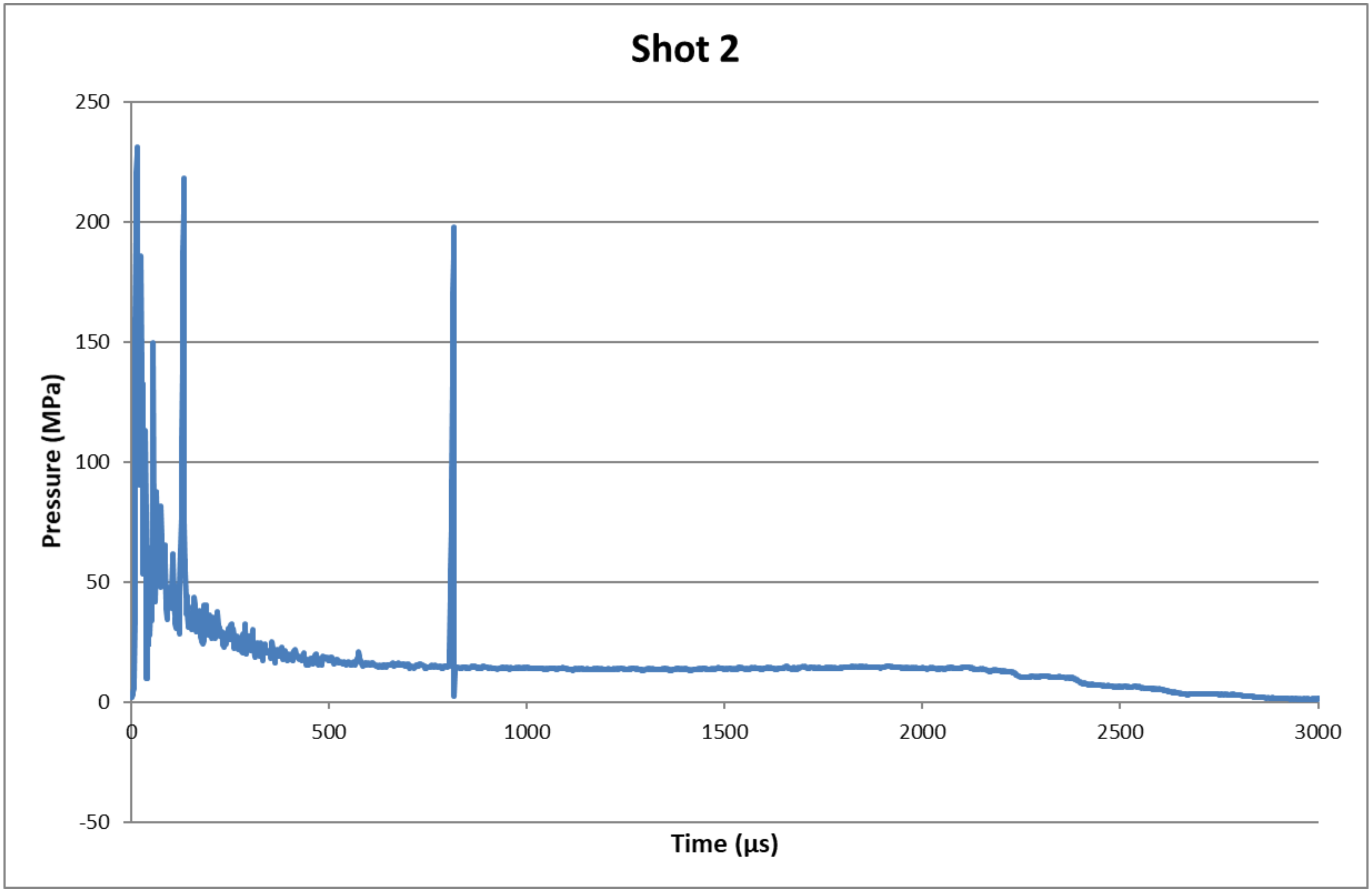
Shot 2
Pressure (MPa)
250
200
150
100
50
0
-50
0
500
1000
1500
2000
2500
3000
Time (µs)

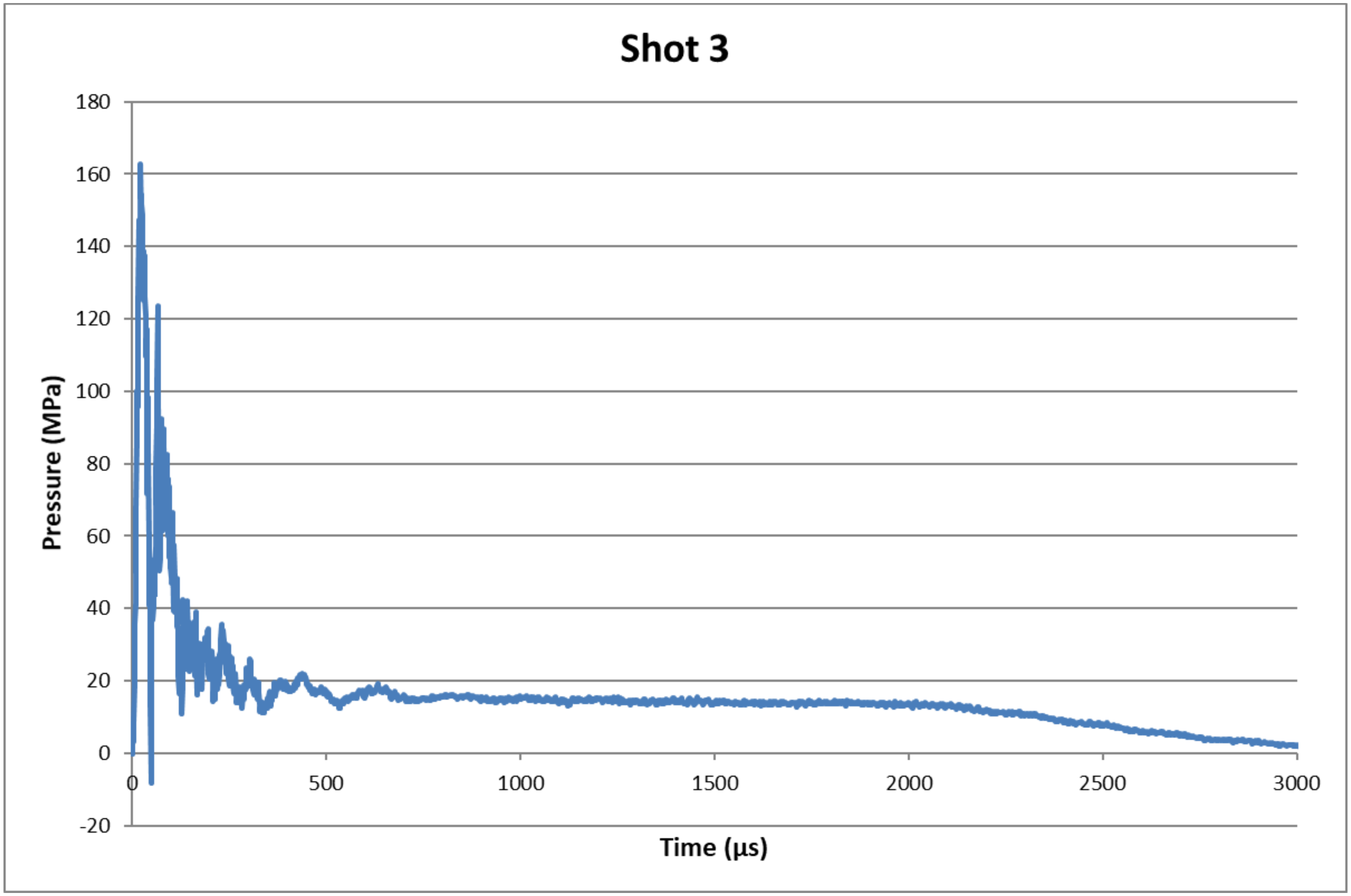
Shot 3
Pressure (MPa)
180
160
140
120
100
80
60
40
20
0
-20
0
500
1000
1500
2000
2500
3000
Time (µs)

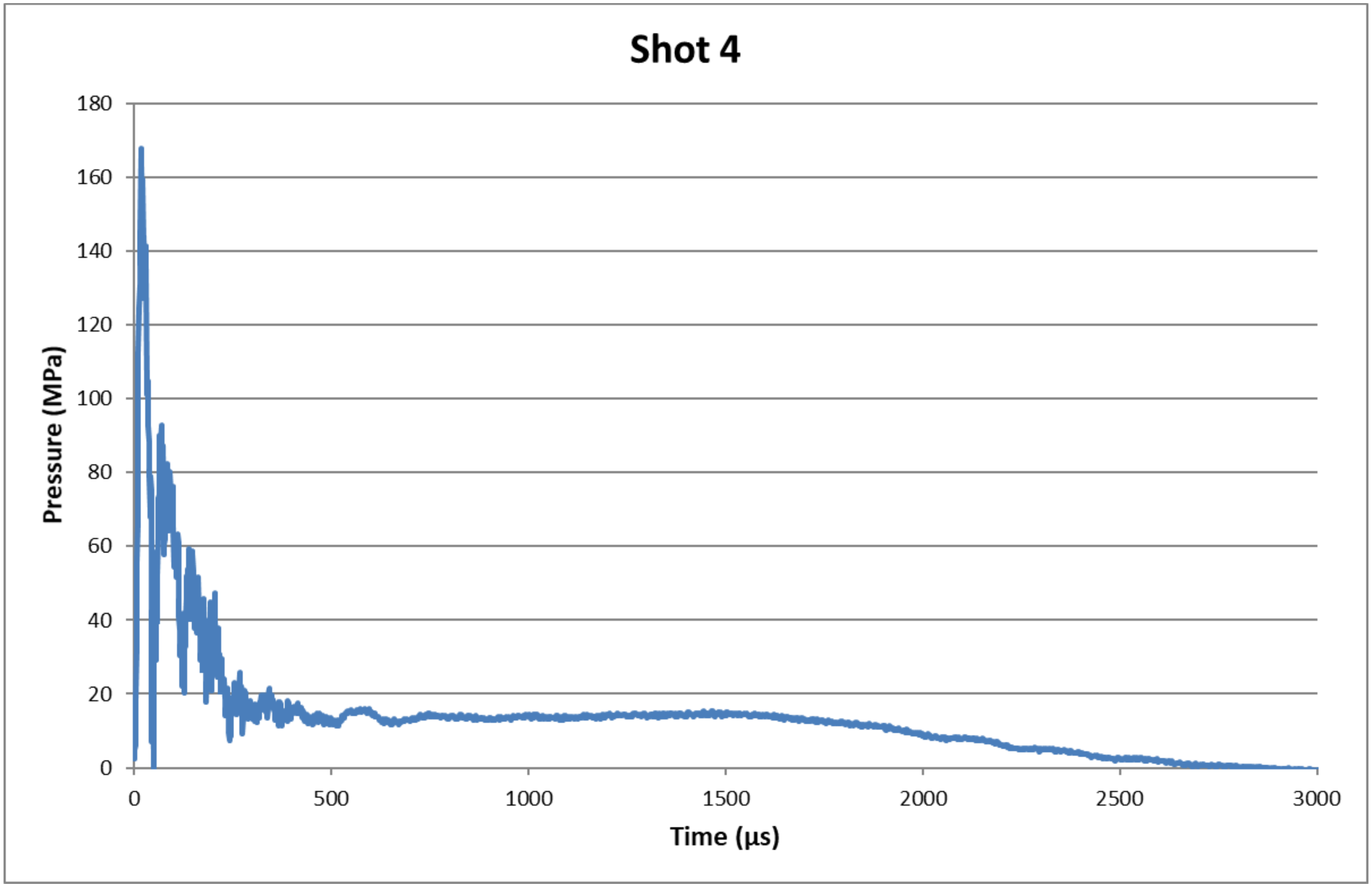
Shot 4
Pressure (MPa)
0
20
40
60
80
100
120
140
160
180
0
500
1000
1500
2000
2500
3000
Time (µs)

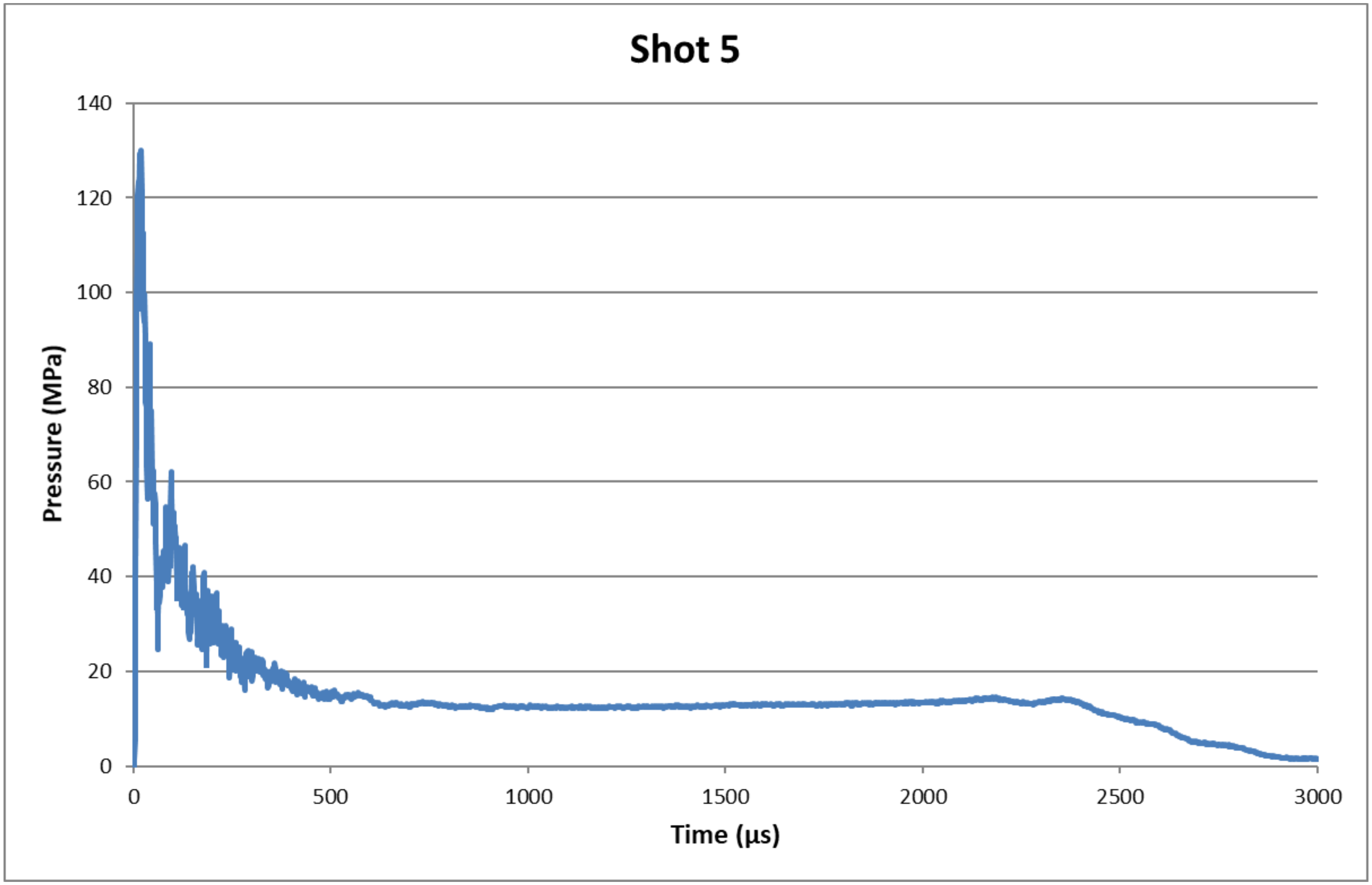
Shot 5
Pressure (MPa)
0
20
40
60
80
100
120
140
Time (µs)
0
500
1000
1500
2000
2500
3000

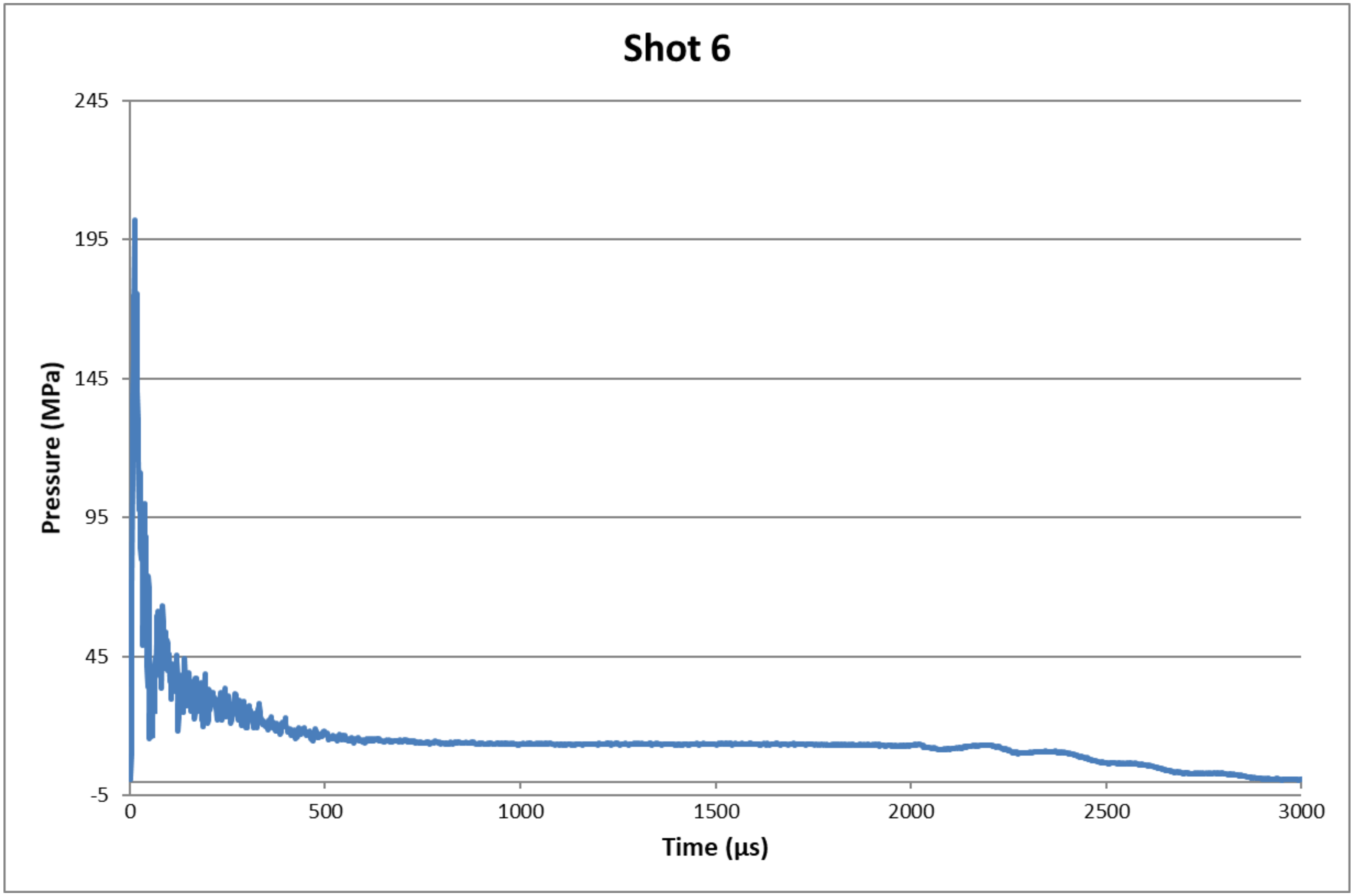
Shot 6
245
195
145
95
45
-5
Pressure (MPa)
0
500
1000
1500
2000
2500
3000
Time (µs)

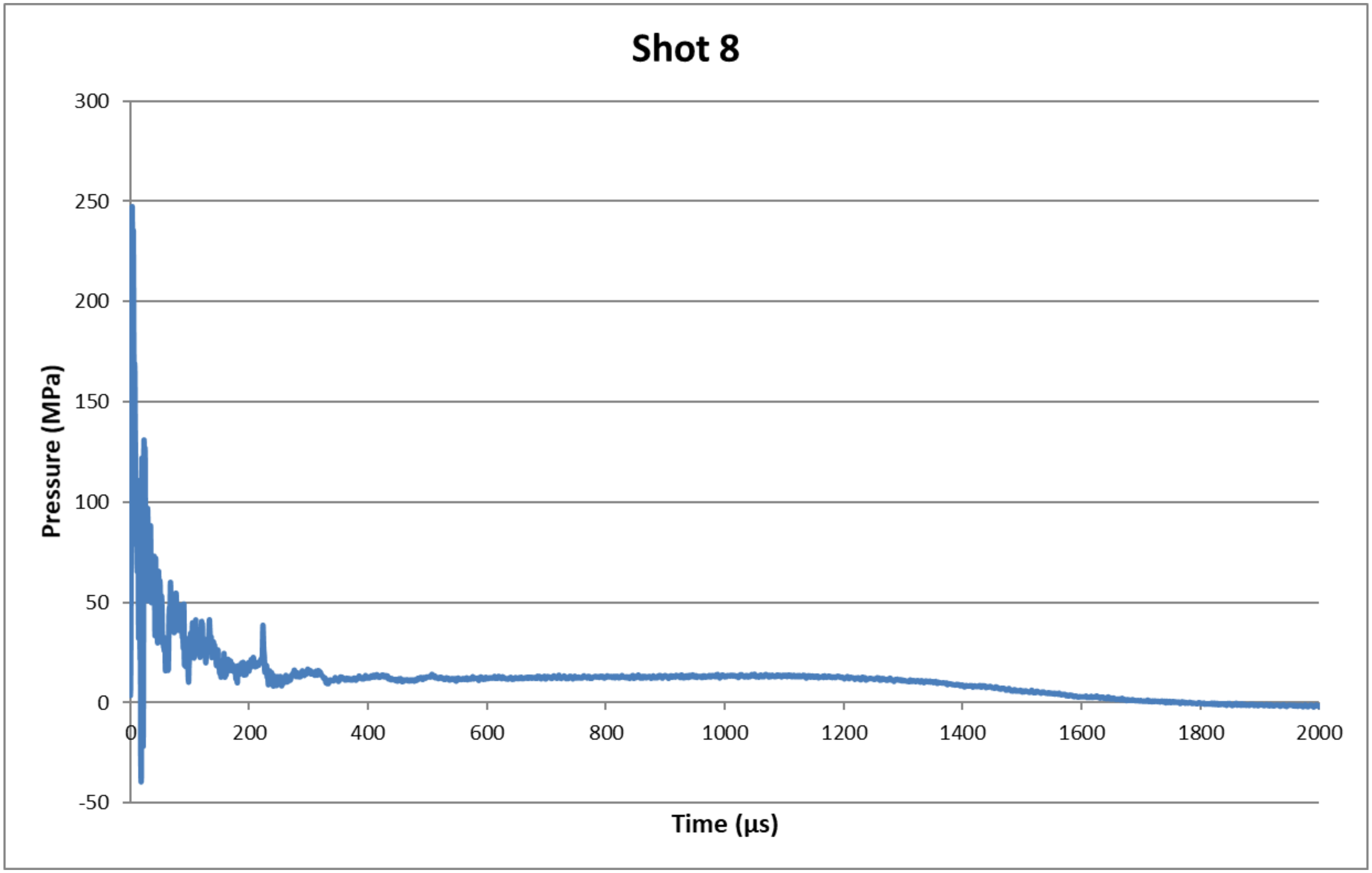
Shot 8
Pressure (MPa)
300
250
200
150
100
50
0
-50
0
200
400
600
800
1000
1200
1400
1600
1800
2000
Time (μs)

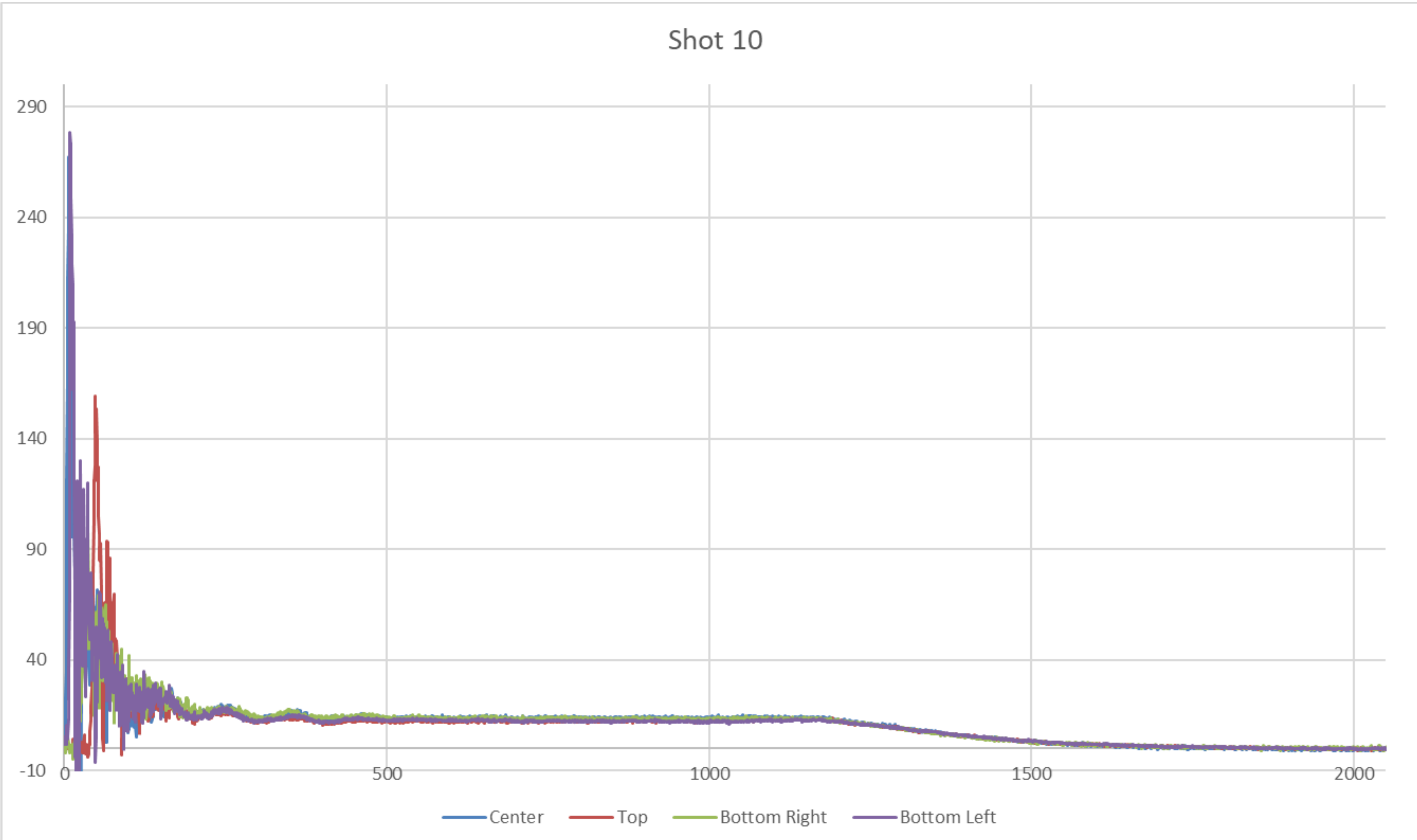
Shot 10
290
240
190
140
90
40
-10
0
500
1000
1500
2000
Center
Top
Bottom Right
Bottom Left

Appendix F – Gelatin Bird Shot Statistical Analysis

Shot #	Transducer Location	Peak Pressure (MPa)	Max Peak Pressure (MPa)	Start of Steady-State (µs)	End of Steady-State (µs)	Final Time (µs)	Median Steady-State (MPa)	Max Median Steady-State (MPa)	Peak Impulse (Pa*s)	Max Peak Impulse (Pa*s)	Steady-State Impulse (Pa*s)	Max SS Impulse (Pa*s)
1	Center	244.3	244.3	200	981	2314	14.3	14.3	8686	8686	15624	15624
2	Center	301.1	301.1	137	1060	2311	15.3	15.3	7508	7508	19331	19331
3	Center	194.4	194.4	218	916	2494	15.56	15.56	8481	8481	16620	16620
4	Center	279.8	279.8	167	1092	2384	14.35	14.35	9144	9144	14115	14115
5	Center	243.2	243.2	271	1057	2449	14.47	14.47	9837	9837	15176	15176
6	Center	181.6	181.6	167	1055	2099	14.39	14.39	6844	6844	16584	16584
7	Center	187.2	187.2	120	780	2111	15.82	15.82	6715	6715	16283	16283
8	Center	151.1	151.1	234	1182	2699	13.93	13.93	7925	7925	15798	15798
9	Center	232.9	232.9	233	1012	2414	14.72	14.72	8368	8368	15771	15771
10	Center	274	298.7	111	1177	2010	14.75	14.75	2573	6305	19866	19866
	Top	179.8		200	1171	1990	12.76		5682		15656	
	Bottom Right	117.2		205.5	1171	1990	14.02		6150		17052	
	Bottom Left	298.7		105	1167	2000	12.86		6305		17736	

Shot #	Transducer Location	Peak Pressure (MPa)	Max Peak Pressure (MPa)	Start of Steady-State (µs)	End of Steady-State (µs)	Final Time (µs)	Median Steady-State (MPa)	Max Median Steady-State (MPa)	Peak Impulse (Pa*s)	Max Peak Impulse (Pa*s)	Steady-State Impulse (Pa*s)	Max SS Impulse (Pa*s)
11	Center	266.7	266.7	254.5	1130	2150	14.48	14.48	9391	9391	18466	18466
	Top	78.5		135	1061	2130	11.17		4166		14552	
	Bottom Right	87.4		208	1157	2150	13.43		5916		17600	
	Bottom Left	138.9		233	1161	2050	13.39		7644		17384	
12	Center	195.4	197.3	183	758	2070	14.46	15.93	6686	6873	11708	13259
	Top	48.2		114	654	2031	14.01		1727		11078	
	Bottom Right	185.8		191	745	1974	15.64		6391		12789	
	Bottom Left	197.3		193	740	2046	15.93		6873		13259	
13	Center	173.5	173.5	242	786	2014	13.72	16.39	4289	7988	11172	13859
	Top	74.1		170	678	2036	14.68		4539		11691	
	Bottom Right	156.7		208	756	2034	16.39		6913		13859	
	Bottom Left	119.1		254	787	1587	14.05		7988		11275	

Shot #	Transducer Location	Peak Pressure (MPa)	Max Peak Pressure (MPa)	Start of Steady-State (µs)	End of Steady-State (µs)	Final Time (µs)	Median Steady-State (MPa)	Max Median Steady-State (MPa)	Peak Impulse (Pa*s)	Max Peak Impulse (Pa*s)	Steady-State Impulse (Pa*s)	Max SS Impulse (Pa*s)
14	Center	195.4	222.2	227	853	2151	13.97	15.37	7860	7860	12435	14763
	Top	92.7		183	792	2179	15.37		4503		13126	
	Bottom Right	222.2		145	857	2111	14.57		6046		14763	
	Bottom Left	185.6		156	867	2199	14.65		6838		14510	
15	Center	360	360	270	905	2154	12.35	15.19	9011	9011	10668	14059
	Top	49.5		261	863	2083	12.36		5789		10530	
	Bottom Right	114.9		197	877	2058	15.19		6405		14059	
	Bottom Left	195.3		244	913	2159	13.36		7937		12216	
16	Center	260.2	260.2	186	830	2262	13.08	16.37	7635	7635	12346	15431
	Top	66.4		188	765	2098	15.15		5327		13226	
	Bottom Right	172.2		211	806	2148	16.37		7203		15431	
	Bottom Left	124		176	819	2137	10.47		5747		10081	

Shot #	Transducer Location	Peak Pressure (MPa)	Max Peak Pressure (MPa)	Start of Steady-State (µs)	End of Steady-State (µs)	Final Time (µs)	Median Steady-State (MPa)	Max Median Steady-State (MPa)	Peak Impulse (Pa*s)	Max Peak Impulse (Pa*s)	Steady-State Impulse (Pa*s)	Max SS Impulse (Pa*s)
17	Center	221.1	221.1	190	1028	2265	11.81	13.98	7062	7062	13063	15277
	Top	76.1		226	1022	2154	10.9		5121		11034	
	Bottom Right	106.9		175	1024	2224	12.83		5799		14569	
	Bottom Left	165.7		182	1006	2154	13.98		6132		15277	
	Mean =		236.2	194	938	2148		15.02		7978		15899
	Median =		232.9	193	913	2137		14.75		7925		15624
	Minimum =		151.1	105	654	1587		13.93		6305		13259
	Maximum =		360.0	271	1182	2699		16.39		9837		19866
	Standard Deviation =		54.3	44	159	178		0.79		1027		1862
	99% Population Max =		376.5					17.07		10632		20709

Appendix G – Discretization Convergence

SPH Size (mm)	TSSFAC	Peak Pressure (MPa)	% Change	Asymptotic Check	Grid Convergence Index
2	0.5	468.4	NA	NA	NA
	0.25	538.7	13.0%	NA	NA
	0.125	615.6	12.5%	1.143	181.94%
	0.063	641.1	4.0%	1.041	2.47%
	0.031	650.8	1.5%	1.015	1.14%
	0.016	655.9	0.8%	1.008	1.08%
	0.008	657.7	0.3%	1.003	0.19%
1	0.25	353.3	NA	NA	NA
	0.125	357.4	1.1%	NA	NA
	0.063	372.5	4.1%	1.042	6.96%
	0.031	382	2.5%	1.026	5.27%
	0.016	382	0.0%	1	0.00%
0.5	0.25	371	NA	NA	NA
	0.125	372.6	0.4%	NA	NA
	0.063	390.1	4.5%	1.047	6.17%
	0.031	398	2.0%	1.02	2.04%
	0.016	401	0.7%	1.008	0.57%
0.25	0.5	344	NA	NA	NA
	0.25	363.7	5.4%	NA	NA
	0.125	403.7	9.9%	1.11	24.41%
	0.063	405.9	0.5%	1.005	0.04%

Appendix H – Gelatin Bird Model Creation Results Based on Gruneisen Parameters and Dynamic Viscosity

This appendix shows the results from simulations that attempted to fit the pressure profile to the target parameters by adjusting only Gruneisen C, Gruneisen S, and the dynamic viscosity. Results that matched the target values within 10% are highlighted green, those with errors within 20% are highlighted yellow, and those with errors greater than 20% are highlighted red.

Gruneisen C (m/s)	Dynamic Viscosity (Pa*s)	Gruneisen S	Peak Pressure (MPa)	% Error	Start of Steady-State (µs)	End of Steady-State (µs)	Final Time (µs)	Steady-State Pressure (MPa)	% Error	Peak Impulse (Pa*s)	% Error	Steady-State Impulse (Pa*s)	% Error	Total Impulse (Pa*s)	% Error
500	600	0	233	-38.1%	223	1150	2180	16.43	-3.7%	10541	-0.9%	18341	-11.4%	28882	-7.8%
	600	1	223	-40.8%	215	1080	2210	16.54	-3.1%	9830	-7.5%	19616	-5.3%	29446	-6.0%
	600	5	217.6	-42.2%	183	1040	2200	17.73	3.9%	8564	-19.5%	20997	1.4%	29561	-5.7%
	600	10	374.5	-0.5%	204	990	2200	18.52	8.5%	8391	-21.1%	20360	-1.7%	28751	-8.3%
	1000	1	370.4	-1.6%	226	1010	2120	19.97	17.0%	10698	0.6%	21535	4.0%	32233	2.8%
	1000	2	325.1	-13.7%											
	1000	3	319	-15.3%											
	1000	10	364.2	-3.3%											
	1500	2	372.4	-1.1%	182	1020	2210	19.92	16.7%	10722	0.8%	23497	13.5%	34219	9.2%
	2000	1	675.6	79.4%	250	842	2500	22.69	32.9%	13330	25.4%	22541	8.8%	35871	14.5%
	2000	2	677	79.8%	193					11833	11.3%				
	2000	6	530.9	41.0%											
	2000	10	438.3	16.4%											
	2000	11	423.9	12.6%											
	2000	12	590.6	56.9%											
700	400	8	392.5	4.2%	131	1012	2210	16.22	-5.0%	7075	-33.5%	20688	-0.1%	27763	-11.4%
	1000	1	351	-6.8%	162	964	2150	20.48	20.0%	9120	-14.2%	22715	9.7%	31835	1.6%
1000	0	3.07	376.6	0.0%	118	1007	2500	14.47	-15.2%	6108	-42.6%	18087	-12.7%	24195	-22.8%
	200	4.92	376.6	0.0%	127	1000	2300	14.83	-13.1%	6687	-37.1%	18973	-8.4%	25660	-18.1%
	400	6.55	376.3	-0.1%	123	1010	2250	16.52	-3.2%	6842	-35.6%	20778	0.3%	27620	-11.9%
	500	7.3	376.5	0.0%	124	1050	2250	16.98	-0.5%	7019	-34.0%	21676	4.7%	28695	-8.4%
	800	0	312.8	-16.9%											
	925	0	364.2	-3.3%											
	930	0	366.4	-2.7%	145	839	2150	20.26	18.7%	8162	-23.2%	23315	12.6%	31477	0.4%
	950	0	399.2	6.0%											
	1000	0	415.7	10.4%											
	1000	1	417.8	11.0%	146	823	2160	21.12	23.7%	8329	-21.7%	23678	14.3%	32007	2.1%
	1000	3	393.1	4.4%	144					8334	-21.6%				
	1000	7.3	378.6	0.6%	136	790	2220	21.81	27.8%	8146	-23.4%	23434	13.2%	31580	0.8%
	1500	0	522.7	38.8%											
1200	0	2	351.5	-6.6%	114	1100	2300	14.77	-13.5%	6072	-42.9%	18704	-9.7%	24776	-20.9%
	0	2.47	376.8	0.1%	202	1010	2500	14.26	-16.5%	7669	-27.9%	16610	-19.8%	24279	-22.5%
	1000	1	431.3	14.6%	145	1000	2160	19.98	17.0%	8469	-20.3%	23797	14.9%	32266	3.0%
1400	0	1.75	377	0.1%	172	1050	2350	14.73	-13.7%	7475	-29.7%	17329	-16.3%	24804	-20.9%

Gruneisen C (m/s)	Dynamic Viscosity (Pa*s)	Gruneisen S	Peak Pressure (MPa)	% Error	Start of Steady-State (µs)	End of Steady-State (µs)	Final Time (µs)	Steady-State Pressure (MPa)	% Error	Peak Impulse (Pa*s)	% Error	Steady-State Impulse (Pa*s)	% Error	Total Impulse (Pa*s)	% Error
1450	0	1	350.1	-7.0%	178	1080	2450	14.03	-17.8%	7358	-30.8%	17110	-17.4%	24468	-21.9%
	0	1.56	376.7	0.1%	171	1108	2500	14.06	-17.6%	7459	-29.8%	17277	-16.6%	24736	-21.1%
	0	2	398	5.7%	164	1032	2250	14.67	-14.1%	7051	-33.7%	17968	-13.2%	25019	-20.2%
	0	2.5	423.2	12.4%	163	1020	2450	15.04	-11.9%	6837	-35.7%	17789	-14.1%	24626	-21.4%
	0	4	504	33.9%	169	1020	2300	14.39	-15.7%	7081	-33.4%	17112	-17.4%	24193	-22.8%
	0	10	934.3	148.2%	163					6976	-34.4%				
	50	2	379.5	0.8%	192	1070	2350	14.04	-17.8%	7716	-27.4%	17016	-17.8%	24732	-21.1%
	100	2	363.8	-3.4%	147	1040	2300	14.43	-15.5%	6809	-36.0%	18132	-12.4%	24941	-20.4%
	200	2	339.1	-9.9%	155	998	2250	15.09	-11.6%	7295	-31.4%	18488	-10.7%	25783	-17.7%
	200	2.96	376.4	0.0%	149	1050	2250	15.02	-12.0%	7177	-32.5%	18573	-10.3%	25750	-17.8%
	400	4.13	376.3	-0.1%	140	1045	2500	16.46	-3.6%	7250	-31.8%	20438	-1.3%	27688	-11.7%
	540	4.85	376.9	0.1%	150	975	2500	17.8	4.3%	7663	-27.9%	21170	2.2%	28832	-8.0%
	560	4.95	377	0.1%	159	1065	2500	16.93	-0.8%	7860	-26.1%	21135	2.1%	28995	-7.5%
	580	5.02	376.5	0.0%	150	972	2500	17.59	3.0%	7736	-27.2%	21255	2.6%	28991	-7.5%
	700	5.5	376.4	0.0%	152	989	2200	18.45	8.1%	8011	-24.7%	22062	6.5%	30073	-4.0%
	810	0	362.2	-3.8%											
	850	0	378	0.4%	166	1050	2130	19.15	12.2%	8642	-18.7%	22371	8.0%	31013	-1.0%
	900	0	393.1	4.4%											
	1000	0	411.6	9.3%	165					8952	-15.8%				
	1000	1	401.1	6.5%	165	820	2170	21.16	24.0%	8925	-16.1%	22900	10.6%	31825	1.5%
	1000	3	430.1	14.2%	155					8725	-17.9%				
	1000	7	428	13.7%	150					8602	-19.1%				
	1500	1	506.2	34.4%											
	1500	3	586.5	55.8%											
	1500	7	574.1	52.5%											
	1500	12	555.6	47.6%											
1482.9	0	2	406.6	8.0%	153	1090	2300	14.21	-16.8%	6828	-35.8%	17293	-16.5%	24121	-23.0%
1500	0	1.31	376.7	0.1%	163	1030	2250	14.75	-13.6%	7079	-33.4%	17550	-15.3%	24629	-21.4%
1600	0	2	430.2	14.3%	148	1110	2250	14.28	-16.3%	6639	-37.6%	17808	-14.0%	24447	-22.0%
1791	0	0.00001	376.4	0.0%	147	1025	2500	15.19	-11.0%	6840	-35.7%	18651	-9.9%	25491	-18.7%
2000	700	0	379.7	0.8%	126	1080	2150	18.27	7.0%	7437	-30.1%	22567	9.0%	30004	-4.3%
	700	1	391	3.9%											
	1000	1	495.9	31.7%											

Curriculum Vitae

Candidate's full name: Shaun Patrick Kennedy

University degrees:

2003 - Bachelor of Computer Science, Acadia University

2007 - Bachelor of Science in Engineering (Mechanical), University of New Brunswick

Academic Awards/Scholarships:

2005-2006 – Anne Murray Alumni Scholarship

2005-2006 - Edwin Jacob Special University Scholarship

2006-2007 - Sodexho Scholarship

2016-2017 - Part-Time Graduate Student Merit Awards

Work Experience:

2007 – 2009, Atomic Energy of Canada Ltd., Mississauga, ON

Mechanical Designer

2009 – 2017, University of New Brunswick, Fredericton, NB

Engineering Lead and Operations Manager at UNB Impact Research and Technology Facility

2016 – Present, Mach85 Inc., Fredericton, NB

President and CEO